New approaches for using satellite observations in numerical weather prediction

Stefan Geiss

München 2021

New approaches for using satellite observations in numerical weather prediction

Stefan Geiss

Dissertation
an der Fakultät für Physik
der Ludwig–Maximilians–Universität
München

vorgelegt von
Stefan Geiß, M. Sc.
aus Zwiesel

München, 04. Oktober 2021

Erstgutachter: Prof. Dr. Martin Weissmann
Zweitgutachter: Prof. Dr. Bernhard Mayer
Datum der Abgabe: 04. Oktober 2021
Datum der mündlichen Prüfung: 13. Dezember 2021

Parts of this thesis are included in (see Appendix A):

Geiss, S, Scheck, L., de Lozar, A., and Weissmann, M.: Understanding the model representation of clouds based on visible and infrared satellite observations, Atmos. Chem. Phys., 21, 12273–12290, https://doi.org/10.5194/acp-21-12273-2021, 2021.

Zusammenfassung

Satellitenbeobachtungen liefern hochauflösende Informationen über den Zustand der Atmosphäre. Bisher wurden hauptsächlich thermische Infrarotkanäle für die Evaluierung und Assimilation von Modellwolken verwendet. Jedoch besteht ein wachsendes Interesse an der Nutzung von Kanälen im solaren Teil des Spektrums, welche zusätzliche und ergänzende Informationen enthalten. Im Vergleich zu Infrarotkanälen können sichtbare Kanäle genauere Informationen über die Flüssig- und Eiswasserpfade der Wolken liefern und sind empfindlicher gegenüber der Wolkenmikrophysik. Des Weiteren korreliert die solare Reflektanz am oberen Rand der Atmosphäre stark mit der Globalstrahlung am Boden. Die Assimilation solarer Reflektanzen hat daher das Potenzial, wolkenbezogene Vorhersagen zu verbessern. In Anbetracht des steigenden Anteils der wetterabhängigen erneuerbaren Energieerzeugung werden genauere Solarstrom- und daher Wolkenvorhersagen immer wichtiger.

In dieser Arbeit werden zwei neue Möglichkeiten der Nutzung von Satellitenbeobachtungen erörtert. Zum einen werden zwei komplementäre Satellitenkanäle verwendet, um die Darstellung von Modellwolken besser zu verstehen. Beobachtete und synthetische sichtbare und infrarote Satellitenbilder können systematische Fehler in Modellwolken aufdecken. Um die Vorteile der Verwendung von sichtbaren und infraroten Satellitenkanälen zu demonstrieren, werden sie sowohl einzeln als auch gemeinsam evaluiert. Hier berechnen zwei Vorwärtsoperatoren die synthetischen solaren Reflektanzen (VISOP) und die Strahlungstemperatur im Infraroten (RTTOV), um die Wolkenverteilung des Modells aus der Sicht eines Satelliten zu bewerten. Die Kombination der Strahlungstemperatur und der solaren Reflektanzen erleichtert die Zuordnung einzelner Abweichungen zu spezifischen Modellmängeln. Die Ergebnisse zeigen, dass die Modellannahme von Wasserwolken, welche vom Modell nicht aufgelöst werden können, die Hauptfehlerquelle in den sichtbaren Satellitenbildern ist. Satellitenbeobachtungen sind daher gut geeignet, um die Einstellungen für Modellwolken unterhalb der Modellauflösung zu optimieren.

Des Weiteren wird in dieser Arbeit ein sichtbarer Satellitenkanal zur Berechnung der Analyse genutzt, um die Wolkenverteilung und -dicke initial zu verbessern. Die Analyse entspricht der besten Schätzung des atmosphärischen Zustands und dient als Ausgangspunkt für die numerische Wettervorhersage. Das Potenzial wird für eine mehrwöchige Sommerperiode in Mitteleuropa aufgezeigt. Durch die Assimilation eines sichtbaren Satellitenkanals wird sowohl die solare Reflektanz selbst, als auch die Globalstrahlung am Boden für bis zu 24 Stunden erheblich besser vorhergesagt. Schließlich zeigt die Evaluation der Niederschlagsvorhersage, dass die Genauigkeit der räumlichen Niederschlagsverteilung über mehrere Vorhersagestunden erhöht wird. Dies deutet darauf hin, dass die Assimilation sichtbarer Satellitenbeobachtungen die Konsistenz zwischen der Analyse und der (Thermo-) Dynamik des Modells verbessert.

Abstract

Satellite observations provide high-resolution information on the state of the atmosphere. This thesis examines two novel approaches for using satellite observations in numerical weather prediction. The primary observations used are provided by the SEVIRI instrument on EUMETSAT's geostationary MSG satellite. Forward operators are applied to the model output of Deutscher Wetterdienst's regional numerical weather forecasting system to generate synthetic visible and infrared satellite images. The first approach combines two complementary satellite channels providing a wealth of information to better understand the model representation of clouds. The second approach assimilates visible satellite observations for the improvement of model initial conditions and subsequent forecasts.

So far, mainly thermal infrared channels have been utilised for model cloud evaluation and assimilation. However, visible channels can provide better information on clouds' liquid and ice water paths and are more sensitive to cloud microphysics than infrared channels. Thus, their assimilation has the potential to improve cloud-related forecasts. Moreover, solar reflectance at the top of the atmosphere (TOA) strongly correlates with solar irradiance at the surface. Given the rising share of renewable energy production, accurate solar power forecasts are increasingly important in terms of network safety and socio-economic value. However, solar power forecasts can only be as accurate as the model representation of clouds in the forecast.

Multiple parameterisations influence model clouds with many, often not well-constrained parameters. Observed and synthetic visible and infrared images can detect systematic errors in model clouds. To demonstrate the benefits of using both visible and infrared satellite channels, they are assessed individually as well as mutually. Here, two forward operators compute synthetic solar reflectance (VISOP) and infrared brightness temperature (RTTOV) to evaluate the model's cloud distribution from a satellite's point of view.

The combination of infrared brightness temperature and solar reflectance facilitates the attribution of individual deviations to specific model shortcomings. Furthermore, the sensitivity of model-derived visible and infrared observation equivalents to modified model and visible forward operator settings was investigated to identify dominant error sources. Estimates for the uncertainty of the visible forward operator turned out to be sufficiently low so that it can be used to assess the impact of model modifications. Results from various changes in the model settings reveal that model assumption on subgrid-scale water clouds is the primary error source in visible satellite images. Visible observations are, therefore, well-suited to constrain cloud settings below model resolution. In contrast, infrared channels are much less sensitive to subgrid clouds. However, they can provide crucial information on errors in the cloud top height.

Moreover, this thesis demonstrates for the first time the potential of assimilating vis-

ible satellite observations based on assimilation experiments for a summer period of four weeks in Central Europe. In this approach, two simulations are compared: a) Quasi-operational simulation with a data assimilation setup utilising conventional observations only and b) a setup including visible satellite observations. The comparison of 24-h forecasts demonstrates a substantial improvement in the spatio-temporal distribution of the solar reflectance at the top of the atmosphere and the global horizontal irradiance at the surface. A sizeable positive impact was found mainly during the first few hours of model integration, but both day-ahead and intra-day forecasts of solar power generation could benefit. Moreover, each forecast update can reduce solar power forecast errors substantially, different to the operational setup as errors in both quantities highly correlate and the analysis's horizontal cloud distribution and cloud thickness are considerably improved through the assimilation of visible satellite images. Evaluating the analyses and the short-term forecasts (+1 h) using conventional observations reveals a quasi-neutral impact. Finally, evaluating 24-h precipitation forecast demonstrates that the spatio-temporal accuracy is enhanced for several hours of model integration. This implies that assimilating visible satellite observation improves consistency between the analysis and the model (thermo-) dynamics.

Contents

Chapter 1

Introduction

An essential requirement for photovoltaic (PV) feed-in forecasts is an accurate forecast of clouds and thus radiation forecast in numerical weather prediction (NWP) models. The output power of a PV power plant is mainly determined by solar irradiance, which in turn is primarily affected by cloud cover (Zack, 2011). However, convective-scale NWP, meaning km-resolution, possess uncertainties in forecasts of clouds due to their complex nature. To reduce forecast errors and achieve the objective of better predicting solar power generation, improvements in the model representation of clouds in NWP models are essential. Including more accurate physical parameterisations, tuning existing parameterisations related to clouds, and representing (small-scale) cloud distribution in the analysis can improve cloud forecasts. The conventional observation system alone is insufficient for these applications. This thesis was carried out in the integrated project MetPVNet to develop innovative satellite-based methods for improved PV power prediction on different time scales at the distribution network level (Meilinger, 2017).

1.1 Solar power and cloud forecast using NWP models

As the share of renewable energy in the world's total electricity supply rises, there is an increased need to improve cloud and radiation forecasts using NWP models. Solar PV power production is one of the fastest-growing forms of renewable energy, with an increase of 22 % globally (IEA, 2020). In Germany, the share of solar energy in electricity generation exceeded 10 % in 2020 for the first time (Fig. 1.1). The German government plans to increase the share of renewable energies in gross electricity consumption from almost 46 % in 2020 to 65 % until 2030 (BReg, 2021, BMWi, 2021) and to at least 80 % until 2050 (Meilinger, 2017).

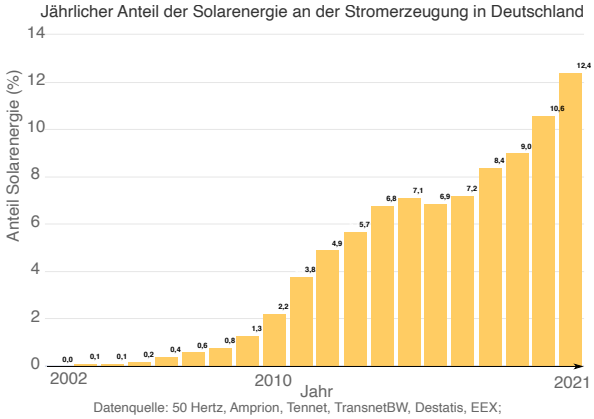

Figure 1.1: *Development in the share of photovoltaic energy generation in Germany over the last decades (Burger, 2021a).*

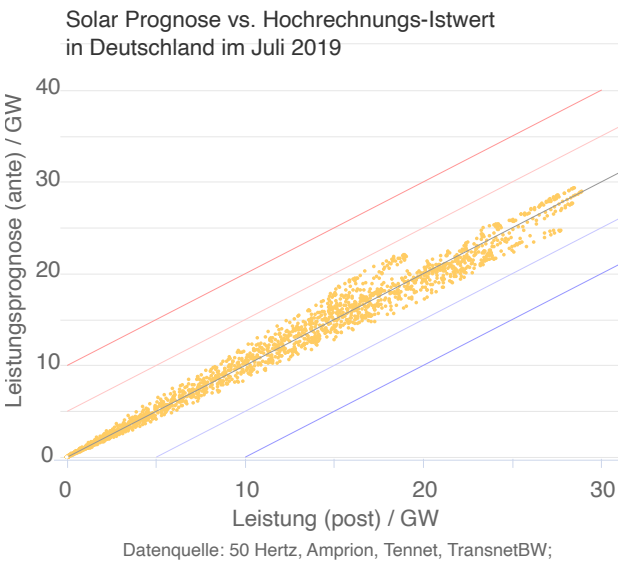

Figure 1.2: *Domain-averaged and post-processed solar power generation prediction vs observation in Germany for July 2019 (Burger, 2021b).*

The four German transmission system operators TenneT, 50Hertz, Ampirion and TransBW, only need to provide forecasts of their domain-averaged PV power generation to balance the expected power generation with consumption (Schrödter-Homscheidt et al., 2015). According to Wirth and Schneider (2015), the domain-averaged PV power generation forecasts for these four domains is relatively predictable on average, thanks to reliable weather forecasts and post-processing (Fig. 1.2). Moreover, the large-scale weather conditions are relatively predictable using NWP, and regional changes in cloud cover cannot lead to severe Germany-wide PV electricity production fluctuations. From 1 October 2021, power generation forecasts for the 874 distribution system operators (Statista, 2021) are also required to manage PV power plants with powers of 100 kW and below (e.g. Sieling and Müllers, 2021). Hence, a more accurate prediction of renewable power generation based on NWP models is crucial to efficiently using alternative power sources, maintaining network safety, reducing balancing costs, and increasing socio-economic benefits (Tuohy et al., 2015, Lenzi et al., 2013).

According to Köhler et al. (2017), the main shortcomings in solar power generation prediction using NWP are related to forecasting the dissipation of low stratus and fog, the spatial and temporal resolution of convection and shallow cumulus below model resolution and Saharan dust outbreaks. Kurzrock et al. (2018) also demonstrated that the representation of low stratus in the model dominates the uncertainty of PV power production. Radiation errors are particularly problematic if present in a day-ahead forecast and persisting after an intra-day update (Siefert et al., 2017). Lorenz et al. (2009) evaluated one year of radiation forecasts using the IFS model of ECMWF (European Centre for Medium-Range Weather Forecasts) and found a relative RMSE of nearly 40 % in Germany. More general, most NWP models overestimate radiation (e.g. ECMWF, NDFD, WRF in Remund et al. (2008)) in many regions on the globe. Such radiation biases are mainly due to biases in cloud forecasts (Lorenz et al., 2009). However, cloud formation and development often depend on small-scale atmospheric processes, which are unresolved in NWP models and need to be parameterised. Furthermore, clouds are used to tune the radiation flux at the top of the atmosphere (TOA) (e.g. Schäfer et al., 2021). Finally, most regional NWP models do not use cloud-related observations to compute the analysis because we lacked adequate observations and challenges related to data assimilation. Hence, the first three to six hours of most NWP models are not particularly useful for solar forecasting; as a result, nowcasting and sky imaging methods have been used with some success (Tuohy et al., 2015).

All in all, there are vast potentials in improving solar power forecast using NWP models

and by incorporating satellite observations: a more reliable model representation of clouds and their time variability, assimilating cloud-related satellite observations and a higher update frequency of forecast initialisation (Mathiesen et al., 2013, Tuohy et al., 2015, Meilinger, 2017, Kurzrock et al., 2018). Similar considerations apply to precipitation and weather forecast generally. Exploiting satellite observations for weather forecasts is not straightforward, and we can only assimilate what we can simulate (Weissmann et al., 2014, Gustafsson et al., 2018).

1.2 Model clouds evaluation using satellite observations

Many authors (e.g. Seifert, 2011, Illingworth et al., 2007) suggested utilising new observations for cloud evaluation to constrain uncertain model assumptions. Cloud-related observations may diagnose systematic errors in model clouds and reveal which model processes or parameterisations need improvements. Satellite images obtained by instruments on geostationary or polar-orbiting satellites are well-suited for this purpose, as they contain high-resolution information on the location and properties of clouds. These instruments' solar and thermal channels provide complementary information on clouds properties. However, this information can often be ambiguous using only a single channel for evaluation, depending on the atmosphere's thermodynamic state, aerosols, and trace gases.
Prior model evaluation studies primarily focused on retrieved quantities like derived cloud fraction, cloud optical depth, and cloud top height by using retrieval algorithms (e.g. Zhang et al., 2005, Otkin and Greenwald, 2008, Senf et al., 2020). The combination of information derived from visible and infrared satellite observations is used in the ISCCP-approach (International Satellite Cloud Climatology Project; see, e.g. Rossow and Schiffer (1991)). The ISCCP-approach constructs cloud type histograms of retrieved cloud optical thickness and cloud top pressure to detect shortcomings related to model clouds (e.g. Tselioudis and Jakob, 2002, Otkin and Greenwald, 2008, Franklin et al., 2013). These studies revealed that systematic cloud biases are present in most models and that the representation of clouds depends on almost every model parameterisation (Webb et al., 2001).

Quantities retrieved from satellite observations like cloud optical depth are relatively easy to interpret. Yet, retrievals have the drawback that (a) characterising errors is often problematic (Errico et al., 2007), and (b) retrieved quantities can be ambiguous (Fig. 1.3). A reasonable characterisation of errors is crucial not only for model evaluation but also for data assimilation. Moreover, a realistic model representation of clouds is vital to assimilate them successfully. In this thesis and generally in data assimilation, the "direct approach" employing forward operators is preferred because the data assimilation algorithm assumes uncorrelated errors. However, retrievals often incorporate model information leading to undesirable error correlations between the model and the retrieved information used for evaluation. Furthermore, only if the evaluation method's

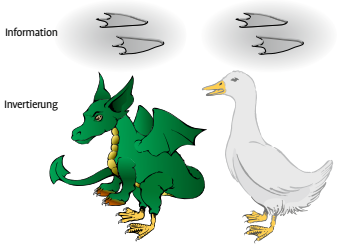

Figure 1.3: *Ambiguity in retrievals. The figure is taken from Köpke and Sachweh (2012).*

errors are sufficiently small, reliable conclusions can be drawn about model errors.
Evaluating model cloud representation using a combination of visible and infrared satellite images directly has not been demonstrated before with operationally applicable forward operators. Given the advantages of error characterisation, the forward operator approach is used in this thesis to compare observed and synthetic images. The evaluation relies on the fast methods available in the radiative transfer package RTTOV (Saunders et al., 2018) to generate synthetic infrared images. RTTOV is operationally used by many weather centres (e.g. ECMWF) and several authors have examined related uncertainties of these methods (e.g. Senf and Deneke, 2017, Saunders et al., 2017, 2018). The visible forward operator applied to the model state computes synthetic visible satellite images. VISOP has been developed, improved and the computational efficiency was greatly accelerated at LMU and DWD over the last few years (Frèrebeau, 2014, Weissmann et al., 2014, Kostka et al., 2014, Scheck et al., 2016, 2018). VISOP is based on the Method for FAst Satellite Image Simulation (MFASIS) 1D radiative transfer (RT) (Scheck et al., 2016), including an extension to account for the most critical 3D RT effects (Scheck et al., 2018). This 3D visible forward operator shows less systematic deviations than the 1D version compared to Monte Carlo calculations, particularly for large solar zenith angles.

As the direct approach of combining two satellite channels is novel, the sensitivity of solar reflectances and infrared brightness temperatures to variations in cloud-related parameterisations needs to be examined. Thus, are the forward operators accurate enough to detect model changes within their physical plausibility. For RTTOV, it is relatively clear, but as VISOP is new, its range of uncertainty must be estimated, as cloud evaluation only works if the operator is accurate enough.

1.3 Advances in assimilating all-sky satellite observations

Incorporating additional satellite observations in data assimilation to compute the analysis has improved the forecast skill in numerical weather prediction models in the past (Bauer et al., 2015). Still, there is an untapped potential in utilising cloud-affected satellite observations to date (Bauer et al., 2011a,b) that should be exploited as clouds are often associated with meteorologically sensitive areas (atmospheric instability, McNally (2002)). Only a tiny fraction of available satellite observations are assimilated in global models and mainly microwave observations.

Microwave radiance observations are observed from polar-orbiting satellites. While in global models, their assimilation led to substantial forecast improvements in cloud-related and dynamical quantities and precipitation (Bauer et al., 2010, Geer et al., 2010, 2017, 2018), polar-orbiting satellite observations are inadequate for regional NWP systems because the temporal resolution is insufficient.

Recent studies demonstrated the additional benefit of assimilating cloud-affected infrared radiances in forecasting tropical cyclones and convection (e.g. Zhang et al., 2016, 2018, 2019, Honda et al., 2018, Otkin et al., 2017). Hence, it is an active field of research towards all-sky data assimilation in the thermal spectral range. Solar channels were not used in the past because no fast and accurate visible forward operator was available for

operational purposes. Multiple scattering dominates in the solar spectral range, making radiative transfer computations with standard methods complex and slow.

No cloud-affected satellite observations are used in operational convective-scale numerical weather prediction that represents deep convection explicitly. The reasons are systematic deviations in model cloud representation and challenges related to data assimilation algorithms (Weissmann et al., 2014, Gustafsson et al., 2018). Challenges are often a non-Gaussian error distribution in the presence of clouds (Geer et al., 2010), errors in the used forward operators (Scheck et al., 2018), correlated observation errors, (Janjić et al., 2018) and the ambiguity of the measured radiances.

Nevertheless, there is a rising need and a vast potential in exploiting cloud-related satellite observations for convective-scale numerical weather prediction. On the convective scale, diabatic processes are more relevant (Pagé et al., 2007), release latent heat and interact with the large-scale flow. Furthermore, in the presence of clouds, shadows can reduce thermodynamic instability locally by cooling the earth's surface (Jakub and Mayer, 2015), influencing subsequent convection. The conventional observation system alone is insufficient for representing (small-scale) cloud distribution in the analysis. This is where satellite observations come into play because characterised by a high spatial and temporal resolution. Schröttle et al. (2020) showed an overall forecast improvement in an idealised setup by assimilating infrared and visible radiances. In a quasi-operational setup, Scheck et al. (2020) recently demonstrated in a case study a beneficial impact of solar reflectance assimilation on forecasting cloud cover and precipitation for at least up to three hours. However, we still lack sufficient statistics for a more extended period with various atmospheric conditions and longer forecast horizons to make a robust statement about the potentials for convective-scale numerical weather prediction.

1.4 Goals and outline

This dissertation consists of two parts: First, understanding the model representation of clouds. In semi-free simulations which are only driven by boundary conditions, clouds can freely develop and are evaluated using visible and infrared satellite observations. Additionally, the recently developed visible forward operator's uncertainty is estimated. The second part demonstrates the vast potential in assimilating solar reflectance for a multi-week period, focusing on cloud-related forecasts.
Following key research questions are addressed:

I Does the direct approach, using forward operators, help to understand the model representation of clouds and constrain uncertain model parameters?

II Is it possible to reveal additional shortcomings in the model representation of clouds using two complementary satellite observations?

III Does the atmospheric state in the analysis improve by assimilating visible satellite observations?

IV Overall, can we advance convective-scale weather forecasts, particularly solar power prediction?

Structure of this thesis

Chapter 2 summarises the basic principles of convective-scale data assimilation, radiative transfer, and clouds. Furthermore, the corresponding model representations in the used model setup are described. Chapter 3 provides an overview of the experimental setup, including the used data sets and the satellite observations' sensitivities in the presence of clouds. An overview of the applied metrics for the evaluation completes this chapter. Chapter 4 introduce satellite observations and their characteristics for two selected days. This is followed by a discussion of the cloud statistics for a full test period and associated systematic deviations. The sensitivity of synthetic visible and infrared satellite images to model and visible operator settings is assessed. For visible reflectances, the forward operator uncertainty and model sensitivity are estimated and compared. Chapter 5 comprises the impact of solar reflectance assimilation in the analysis, short-term and 24-h forecasts. Assessment of error dependency in solar reflectance at TOA and global horizontal irradiance at the surface is performed. The expected gain in updating solar power forecasts utilising NWP is estimated, and sensitivity experiments complete this chapter. Chapter 6 provides a summary and conclusions.

Chapter 2

Basic principles

2.1 Data assimilation and its implementation in convective-scale NWP systems

The initialisation of numerical weather prediction requires an accurate starting point (analysis). This is achieved by an optimal combination of the last available forecast and observations in the process of data assimilation. This section explains the basic principle of combining a huge data set to achieve the best estimate of the atmospheric state.

For a scalar, the analysis μ_a is computed using four parameters (Talagrand, 1997): the expected value and its standard deviation from a first guess (μ_{fg}, σ_{fg}) and from observations (μ_{obs}, σ_{obs}). The information from a first guess and an observation are uncertain within a certain probability of a range of values (Fig. 2.1). We can exploit the probability from an ensemble of short-term forecasts at a certain location and time for the first guess. For the observation, we need an estimate of the observation error.

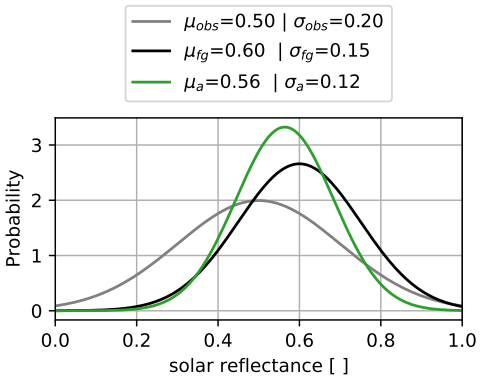

Figure 2.1: *Probability density functions of the observed and the simulated (first guess and analysis) solar reflectance.*

Cost function for a scalar

The analysis μ_a can be computed by minimising a quadratic cost function J(μ_a). For a scalar (as in Fig. 2.1), it reads:

$$J(\mu_a) = \frac{1}{2}[J_b + J_o] = \frac{1}{2}[\frac{(\mu_a - \mu_{fg})^2}{\sigma_{fg}^2} + \frac{(\mu_a - \mu_{obs})^2}{\sigma_{obs}^2}] \tag{2.1}$$

Minimizing this cost function ($J'(\mu_a)$=0; first derivative) leads to the following analysis:

$$\begin{aligned}\mu_a &= \frac{\sigma_{fg}^2}{\sigma_{obs}^2+\sigma_{fg}^2}\mu_{obs} + \frac{\sigma_{obs}^2}{\sigma_{obs}^2+\sigma_{fg}^2}\mu_{fg} = \mu_{fg} + \frac{\sigma_{fg}^2}{\sigma_{obs}^2+\sigma_{fg}^2}(\mu_{obs}-\mu_{fg}) \\ \mu_a &= \mu_{fg} + k(\mu_{obs}-\mu_{fg}).\end{aligned} \tag{2.2}$$

k is the Kalman Gain or the optimal weight. In case of an unbiased first-guess and observations, first-guess and observation errors with a Gaussian distribution and no correlation between first-guess and observations errors, this combination exhibits the smallest possible squared analysis error in a statistical sense:

$$\sigma_a^2 = (1-k)\sigma_{fg}^2 = \frac{\sigma_{fg}^2\sigma_{obs}^2}{\sigma_{obs}^2+\sigma_{fg}^2}. \tag{2.3}$$

Cost function in three dimensions

As the atmosphere is three dimensional, a 3D cost function

$$J(\mathbf{x}) = \underbrace{(\mathbf{x}-\mathbf{x^b})^T\mathbf{B}^{-1}(\mathbf{x}-\mathbf{x^b})}_{J_b} + \underbrace{(H(\mathbf{x})-\mathbf{y})^T\mathbf{R}^{-1}(H(\mathbf{x})-\mathbf{y})}_{J_o} \tag{2.4}$$

needs to be minimised. The background $\mathbf{x^b}$ contains meteorological variables (e.g. temperature or cloud water content), and $\mathbf{y}$ contains all available observations. The dimensions of $\mathbf{x^b}$ and $\mathbf{y}$ differ with $[\mathbf{x^b}]\approx 10^8$ and $[\mathbf{y}]\approx 10^5$ in the regional ICON-D2 model of Deutscher Wetterdienst. Usually, we can not directly observe the model variables we want to analyse at each model grid point. Often, observations and model grid-points differ in location. Moreover, observations can represent quantities that depend on integrals over parts of the model space containing many grid points. Here, forward operators H come into play, transforming from model to observation space. This can be a simple interpolation or a more sophisticated calculation (e.g. solving radiative transfer).

The observation error covariance matrix is defined as

$$\mathbf{R} = E(\epsilon_{obs}\epsilon_{obs}^T) = \begin{pmatrix} E(\epsilon_1^2) & E(\epsilon_1\epsilon_2) & \dots & E(\epsilon_1\epsilon_i) \\ \vdots & \ddots & & \\ E(\epsilon_i\epsilon_1) & & & E(\epsilon_i^2) \end{pmatrix}.$$

The elements on the diagonal are the observation errors (variances), and the off-diagonal (covariances) elements are usually neglected in operational data assimilation systems.

The background error covariance matrix is analogously computed

$$\mathbf{B} = E(\epsilon_b\epsilon_b^T) = \begin{pmatrix} E(\epsilon_1^2) & E(\epsilon_1\epsilon_2) & \dots & E(\epsilon_1\epsilon_i) \\ \vdots & \ddots & & \\ E(\epsilon_i\epsilon_1) & & & E(\epsilon_i^2) \end{pmatrix}$$

and should ensure a physically consistent analysis update. However, in standard methods (like 3D Var), this matrix is often static (e.g. from a climatology), which is a crude assumption because error covariances depend on the atmospheric conditions. Furthermore,

this matrix is one of the most significant challenges in data assimilation. An efficient approach for minimising the 3D cost function (Eq. 2.4) is the steepest descent method by computing the gradient $\nabla \mathrm{J}(\mathbf{x})$. The analysis is given by

$$\mathbf{x^a} = \mathbf{x^b} + \mathbf{K}(\mathbf{y} - H(\mathbf{x^b})). \tag{2.5}$$

Here, the non-linear observation operator H can be applied but in $\mathbf{K} = \mathbf{B}\mathrm{H}^T(\mathrm{H}\mathbf{B}\mathrm{H}^T + \mathbf{R})^{-1}$, we need a linearised version of the observation operator H. Usually, $\mathbf{K}$ can not numerically be computed with state of the art supercomputers because $\mathbf{B}$ is extremely large $[\mathbf{B}]=10^8\times10^8$ and the inverse of the matrix $(\mathrm{H}\mathbf{B}\mathrm{H}^T + \mathbf{R})^{-1}$ is extremely CPU-intensive.

2.1.1 LETKF

A very efficient approach to find the minimum of the cost function is the very efficient Local Ensemble Transform Kalman Filter (LETKF) after Hunt et al. (2007) and employed in this thesis. The idea of an LETKF is to estimate the analysis locally, i.e. for each model grid point independently, and "Transform" means an efficient computational calculation of the analysis in the low dimensional ensemble space. In other words, the ensemble analysis is a linear combination of the background ensemble with dimension N (ensemble size): $\overline{\mathbf{x}^a} = \overline{\mathbf{x}^b} + \mathbf{X}^b\mathbf{w}$ with the weight $\mathbf{w}$ and the background ensemble perturbations $\mathbf{X}^b = (\mathbf{x}^{b(i)} - \overline{\mathbf{x}^b})$, as will be shown next.

In an LETKF, the flow-dependent background error covariance matrix is computed for each model grid point individually:

$$\mathbf{B} \approx \mathbf{P}^b = (N-1)^{-1}\mathbf{X}^b(\mathbf{X}^b)^T \tag{2.6}$$

$\mathbf{X}^b$ represents the deviation of each ensemble member i from the ensemble mean, and N is the total number of ensemble members. Here, $\mathbf{P}^b$ is in the low dimensional ensemble space with dimension N×N.

The first guess can be transformed to observation space via H (forward operator can be linear or non-linear):

$$\mathbf{y}^{b(i)} = H(\mathbf{x}^{b(i)}), \tag{2.7}$$

and the ensemble mean in observation space

$$\overline{\mathbf{y}^b} = \overline{H(\mathbf{x}^b)} = N^{-1}\sum_i^N H(\mathbf{x}^{b(i)}). \tag{2.8}$$

The background cost junction J_b can be expressed using the weight vectors $\mathbf{w}$:

$$\begin{aligned}
J_b &= (\mathbf{x} - \overline{\mathbf{x^b}})^T(\frac{1}{N-1}\mathbf{X^b}(\mathbf{X^b})^T)^{-1}(\mathbf{x} - \overline{\mathbf{x^b}}) \\
J_b &= (\mathbf{X^b w})^T(\frac{1}{N-1}\mathbf{X^b}(\mathbf{X^b})^T)^{-1}(\mathbf{X^b w}) \\
J_b &= (N-1)\mathbf{w}^T(\mathbf{X^b})^T((\mathbf{X^b})^T)^{-1}(\mathbf{X^b})^{-1}\mathbf{X^b w} \\
J_b &= (N-1)\mathbf{w}^T\mathbf{w}
\end{aligned}$$

The 3D cost function (Eq. 2.4) can now be transformed to the low dimensional ensemble space. The LETKF cost function after Hunt et al. (2007) for a vector $\mathbf{w}$ and dimension N reads

$$J(\mathbf{w}) = \underbrace{(N-1)(\mathbf{w}^T\mathbf{w})}_{J_b} + \underbrace{(\mathbf{y}^o - \overline{\mathbf{y}^b} - \mathbf{Y}^b\mathbf{w})^T\mathbf{R}^{-1}(\mathbf{y}^o - \overline{\mathbf{y}^b} - \mathbf{Y}^b\mathbf{w})}_{J_o}. \tag{2.9}$$

In this formulation of the cost function, a linear approximation is applied:

$$H(\overline{\mathbf{x}^b} + \mathbf{X}^b\mathbf{w}) \approx \overline{\mathbf{y}^b} + \mathbf{Y}^b\mathbf{w}. \tag{2.10}$$

$\mathbf{Y}^b$ is the ensemble perturbation matrix in observation space. This cost function needs to be minimised with respect to the weight vector $\mathbf{w}$.

The minimum of the cost-function (Eq. 2.9) can be explicitly computed

$$\overline{\mathbf{w}} = \tilde{\mathbf{P}}^a(\mathbf{Y}^b)^T\mathbf{R}^{-1}(\mathbf{y}^o - \overline{H(\mathbf{x}^b)}), \tag{2.11}$$

because it is formulated in the low-dimensional ensemble space. $\overline{\mathbf{w}}$ is the analysis mean in ensemble space. From the analysis-error covariance matrix

$$\tilde{\mathbf{P}}^a = [(N-1)\mathbf{I} + (\mathbf{Y}^b)^T\mathbf{R}^{-1}\mathbf{Y}^b]^{-1}, \tag{2.12}$$

the analysis ensemble perturbation (weight matrix) is computed via

$$\mathbf{W} = [(N-1)\tilde{\mathbf{P}}^a]^{1/2}. \tag{2.13}$$

As mentioned above, the analysis of each ensemble member in physical space is a linear combination of the (weighted) background ensemble members and is computed by

$$\mathbf{x}^{a(i)} = \overline{\mathbf{x}^b} + \mathbf{X}^b(\overline{\mathbf{w}} + \mathbf{W}^{(i)}). \tag{2.14}$$

$$\overline{\mathbf{x}^a} = \overline{\mathbf{x}^b} + \mathbf{X}^b\overline{\mathbf{w}} \tag{2.15}$$

is the analysis mean in physical space. Furthermore, the Kalman gain of the ensemble mean

$$\mathbf{K} = \mathbf{X}^b\tilde{\mathbf{P}}^a(\mathbf{Y}^b)^T\mathbf{R}^{-1} \tag{2.16}$$

can be applied to the innovations $(\mathbf{y}^o - H(\mathbf{x}^b_{det}))$ to compute a 'deterministic' analysis

$$\mathbf{x}^a_{det} = \mathbf{x}^b_{det} + \mathbf{K}(\mathbf{y}^o - H(\mathbf{x}^b_{det})). \tag{2.17}$$

This deterministic analysis can be used as the initial condition for a deterministic or control forecast.

To summarise, the advantage of an LETKF is that basically every quantity that can be simulated can be assimilated (linearised and adjoint observation operators are not required), it considers a flow-dependent background error covariance matrix and is computationally very efficient (parallel computation of analysis for each model grid point).

2.1.2 Challenges in data assimilation using (new) observations

Convective-scale data assimilation poses challenges that are related to the algorithm used to compute an analysis. Some of the challenges are addressed in this thesis and briefly summarised here. Challenges, in order to exploit new observations to generate the analysis are the development of operationally applicable forward operators like the visible forward operator VISOP. Forward operators have to be both fast and accurate. In an LETKF, a linear approximation is applied in Eq. 2.10. However, radiances are linear only to a certain degree. The (non-) linearity of the measured signal is shown in Sect. 3.2.1. Furthermore, a Gaussian distribution is assumed in observation and background error. The Gaussianity assumption is related to the non-linearity of the signal and is discussed in the results section (Fig. 5.6 in Sect. 5.2.2). Furthermore, observations and model equivalents are uncertain. According to Janjić et al. (2018), observation error in the observation error covariance matrix $\mathbf{R}$ is represented by (1) measurement error, e.g. calibration or instrument noise for satellite radiances, (2) forward operator error, e.g. radiative transfer, (3) representativeness error, e.g. unresolved scales/point measurement vs model representation and (4) quality control / pre-processing error, e.g. in clear-sky radiance assimilation, pixel are contaminated with ice-covered mountains (snow/glaciers) or semi-transparent clouds. The last three errors are summarised under the term representation error (Janjić et al., 2018). We have to estimate and consider observation errors, e.g. by using Desroziers et al.'s (2005) method. For visible satellite observations, calibration is discussed in Sect. 3.2.1, and the uncertainty of the forward operator is estimated in Chap. 4.3.4. Representativeness error can be reduced by averaging satellite observation to compute a superobservation (discussion below and implementation in Sect. 3.1.1). Contaminated pixels are excluded, e.g. where the topography is greater than 1000m.

Usually, the $\mathbf{R}$-matrix is diagonal, meaning a constant error σ_o. Such an assumption is reliable for independent observations. In future, it will be likely that different channels will be assimilated simultaneously to compute the analysis. Hence, representation error is correlated between different observations, e.g. a radiative transfer error in a forward operator is probably similar for spectrally similar channels. Increasing the observation error gives the observation less weight to compute the analysis and can be used as a tuning parameter.

Finally, a possibility to reduce observation error is to thin or superob data, i.e. average of $k \times m$ satellite pixels, following Scheck et al. (2020). In the mid-latitudes and for the geostationary MSG satellite, k and m differ, as the resolution is different in zonal ($\approx 3\,\mathrm{km}$) and meridional ($\approx 6\,\mathrm{km}$) direction.

Forward operator VISOP

Forward operators (H in Eq. 2.8) are used to transform from model to observation space. It becomes relative more complex

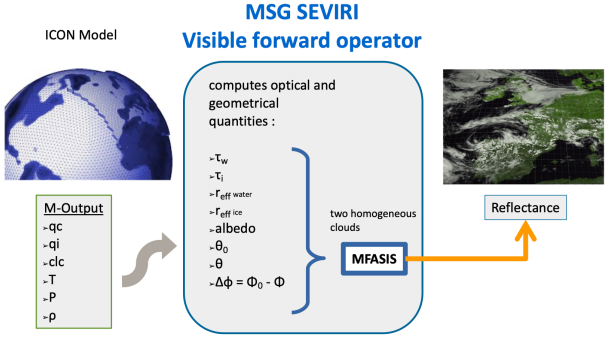

Figure 2.2: *Illustration of the visible forward operator VISOP, transforming from model to observation space.*

if we want to assimilate observations that are not prognostic, like remotely sensed radiances at satellites. To use this information, we have to apply forward operators to the model state. The visible forward operator (VISOP illustration in Fig. 2.2), used in this thesis, calculates optical (Sect. 2.3.2) and geometrical quantities (solar zenith angle Θ_0, satellite zenith angle Θ and the scattering angle α). The optical and geometrical quantities, together with the albedo, are input parameters for MFASIS. MFASIS (Sect. 2.2.1) is a fast enough and operationally applicable radiative transfer method that computes solar reflectances (Eq. 2.19). An advantage of an LETKF is that basically every quantity that can be simulated can be assimilated because the formulation explicitly uses only the non-linear operator.

2.1.3 Regional data assimilation system of Deutscher Wetterdienst

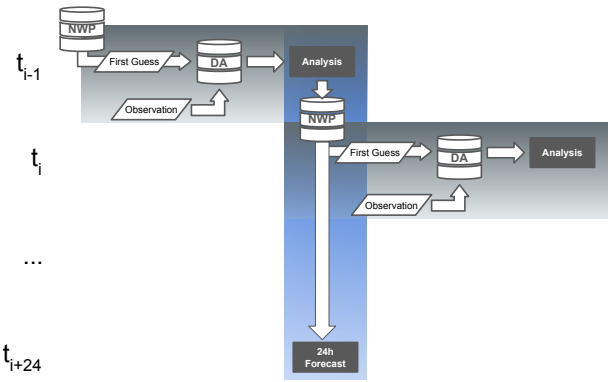

Figure 2.3: *Flow-chart of a numerical weather prediction system with $i \in$ [0,6,12,18] UTC.*

In DA, a first guess (e.g. +1 h forecast lead time) is is a short-term forecast $\mathbf{x^b} = \mathcal{M}(\mathbf{x^a})$, where the NWP model $\mathcal{M}$ is applied to a previous analysis $\mathbf{x^a}$. The model $\mathcal{M}$, solves the primitive equations that describe the atmospheric flow and predicts prognostic variables explicitly (e.g. temperature or cloud water content). The primitive equations are five non-linear partial differential equations that can be solved numerically (only) and consist of continuity, conservation of momentum (3D) and thermal energy equations.

For regional (convective-scale) data assimilation, Deutscher Wetterdienst uses the Km-scale ENsemble Data Assimilation (KENDA, described in Schraff et al. (2016)) based on an LETKF with 40 ensemble members. An hourly cycling generates analyses from where a short-term forecast is computed using the ICON-D2 model (Fig. 2.3). The domain covers entire Germany, Austria, Switzerland, the Benelux countries and partly neighbouring countries.
In a quasi-operational implementation used as a reference in this thesis, only conventional observations are assimilated. The conventional observations are direct observations of prognostic model variables that consist of four observation types:

- AIREP: aircraft observations of temperature, humidity and wind
- PILOT: profiler observations of wind
- SYNOP: surface station observations of 10-m wind and surface pressure
- TEMP: radiosonde observations of temperature, humidity and wind

Usually, conventional observations are available every hour but with a few exceptions. SYNOP wind observations are only assimilated if the topography is sufficiently low (<100 m), hence, only in Northern Germany. TEMP observations are predominantly only available at 0 and 12 UTC. Observations are assimilated up to a height of 300 hPa, meaning that only take-off and landing of aircraft observations close to an airport are considered. Due to the ban on night flights, these observations are usually unavailable from 21 to 4 UTC.

In KENDA, an adaptive localisation method is used for conventional observations to keep the number of observations per model grid point constant. The rationale is that in an LETKF, the degrees of freedom are limited by the ensemble size. Increasing the number per model grid-point would make the analysis too confident towards the observations and reduce the analysis spread. Analysis spread can be increased or controlled using additive and adaptive multiplicative inflation (Houtekamer et al., 2005) and relaxation to prior perturbations (Zhang et al., 2004). Furthermore, if the data set is sufficiently large, the potential in improving the analysis is relatively low by considering more observations. Therefore, the localisation radius is adapted and varies between 50 km and 100 km. In KENDA, the effective number of conventional observations is N=100. Following Scheck et al. (2020), the number of satellite observations per grid-point is N$= 2\pi l_h^2/l_{so^2}$, depending on the localisation scale l_h and the superobbing radius l_{so}. According to Schraff et al. (2016), the observation errors computed using Desroziers et al.'s method in June 2011 are for wind components $\sigma_{obs} \in [1.89, 2.38]$ m/s, temperature $\sigma_{obs} \in [0.55, 1.07]$ K, and relative humidity $\sigma_{obs} \in [9, 14]$ %, depending on the vertical pressure level. Using the same method, Scheck et al. (2020) found an observation error in solar reflectance of $\sigma_{obs} \in (0.1, 0.15)$.

The so-called "latent heat nudging" is applied to adjust the simulated to the radar-derived precipitation during short-term forecasts in the KENDA system. This approach assumes that latent heat release by condensation (Eq. 2.37) is proportional to the precipitation rate near the surface. If the model (under-) overestimates the precipitation rate, a (positive) negative temperature increment is applied to the model grid point. This introduces thermodynamic instability because the buoyancy increases (Eq. 2.36), leading to condensation and precipitation. Additionally, the relative humidity is kept constant by adding a specific humidity increment to avoid undersaturation after increasing the temperature. Otherwise, water droplets would evaporate after adding the temperature increment.

As the ICON-KENDA system is relatively new, there were some changes in the data assimilation system during the time this project was conducted. These changes do not apply to the version used in this thesis but are briefly summarised. Since April 14, 2021 radiosonde and aircraft observations are assimilated up to 200 hPa and 275 hPa, respectively, depending on the instrument (DWD, 2021c). Furthermore, since June 17, 2020, radar reflectivity volume data from the German weather radar network is additionally assimilated (DWD, 2020a). The assimilation of radar reflectivity volume data improved temperature and humidity in 2m height, cloudiness and global horizontal irradiance forecasts for a period from 20 May - 15 June 2020. Since June 23, 2021, the forecasts are initialised eight times a day (at 0, 03, 06, 09, 12, 15, 18, 21 UTC), and the forecast lead time was increased to 48 hours (DWD, 2021a).

2.2 Radiative transfer and its representation in NWP models

Radiation is the main driver of the atmospheric circulation. Weather satellites measure the scattered (solar) or emitted (thermal) radiances from the earth's surface and the atmosphere. This section discusses radiative transfer in the atmosphere and parameterisations in numerical weather prediction models.

Satellite observations measure radiances. The spectral radiance for a monochromatic electromagnetic wave and its radiant energy Q is defined as

$$\mathrm{I}_\lambda(\Theta,\Phi) = \frac{\mathrm{d}^4\mathrm{Q}}{\mathrm{dAdtd}\Omega\mathrm{d}\lambda}[\mathrm{Wm}^{-2}\mathrm{nm}^{-1}\mathrm{sr}^{-1}], \tag{2.18}$$

meaning the energy per unit area dA (perpendicular to the incident beam), the time interval dt, the wavelength range $\mathrm{d}\lambda$ and the radiance direction $\mathrm{d}\Omega$. In the solar spectrum it is often useful to distinguish between the direct radiance coming from the sun and the diffuse radiance related to photons that have already been scattered in the atmosphere or at the surface.

For the solar spectrum, it is helpful to define the dimensionless reflectance at TOA

$$\mathrm{R}_{TOA}(\Theta,\Phi) = \pi\frac{\mathrm{I}_\lambda(\Theta,\Phi)}{\mathrm{E}_0\cos(\Theta_0)} \tag{2.19}$$

with the extraterrestrial flux E_0. The reflectance at TOA for a certain wavelength band corresponding to a satellite channel (e.g. λ=0.6 μm) is the main quantity in this thesis used for evaluation and assimilation.

Integrating radiance over the upper or lower hemisphere results in upward and downward spectral irradiances or fluxes, defined as

$$\mathrm{E}_\lambda = \frac{\mathrm{d}^3\mathrm{Q}}{\mathrm{dtdAd}\lambda}[\mathrm{Wm}^{-2}\mathrm{nm}^{-1}]. \tag{2.20}$$

Each matter with a temperature $\mathrm{T} > 0\,\mathrm{K}$ emits radiation and hence, energy. The sun is basically a black body, meaning that emission and absorption are equal (Kirchhoff's law). This black body radiation can be described using Planck's law.

The spectral radiance of a black body with a specific temperature T and wavelength λ is

$$\mathrm{B}(\lambda,T) = \frac{2\mathrm{hc}^2}{\lambda^5}\frac{1}{exp(\frac{\mathrm{hc}}{\lambda\mathrm{k_B T}})-1}[\mathrm{W}\mu\mathrm{m}^{-1}\mathrm{m}^{-2}], \tag{2.21}$$

with the Planck constant h$\approx$6.6261x10^{-34} Js, the speed of light c$\approx$3x10^8 m/s, and the Boltzmann constant k_B=1.380649x10^{-23} J/K. The radiance measured by a satellite for a certain wavelength (e.g. λ =10.8μm) is an additional quantity in this thesis for evaluating cloud top heights.

Solving this equation for T

$$\mathrm{T} = \frac{\mathrm{hc}}{\lambda \mathrm{k_B}}[\ln(1 + \frac{2\mathrm{hc}^2}{\mathrm{B}(\lambda, T)\lambda^5})]^{-1}[\mathrm{K}] \tag{2.22}$$

gives the black body temperature. The black body temperature or brightness temperature of an atmospheric cloud top is mainly determined by its altitude.

In the atmosphere, electromagnetic waves interact with hydrometeors, aerosols and molecules through scattering and absorption. To describe the radiative transfer in the atmosphere, we need to define optical properties, describing the atmosphere.

The extinction coefficient

$$\beta_{ext} = \beta_{sca} + \beta_{abs}[\mathrm{m}^{-1}], \tag{2.23}$$

is the sum of the scattering and absorption coefficients. The dimensionless optical thickness τ is defined as

$$\tau = \int \beta_{ext}(z)\mathrm{d}z. \tag{2.24}$$

For direct radiation, the attenuation by scattering and absorption of radiation in the atmosphere can be described using Lambert-Beer's law:

$$I(\tau) = E_0 \exp(-\tau/\mu), \tag{2.25}$$

with $\mu = \cos(\theta_0)$. The fraction of scattering and extinction coefficients gives the single scattering albedo

$$\omega = \frac{\beta_{sca}}{\beta_{ext}}. \tag{2.26}$$

Scattering by spherical particles can be described using Mie-Theory. The scattering regime can be divided into Rayleigh, Mie and optical scattering in the atmosphere. The scattering regimes for a particle radius r and wavelength λ are

$$\chi = \frac{2\pi r}{\lambda} :: \begin{cases} << 1 & \text{Rayleigh,} \\ \approx 1 & \text{Mie} \\ >> 1 & \text{Optical} \end{cases} . \tag{2.27}$$

These different regimes show different characteristics in the scattering phase function $\mathrm{P}(\Omega, \Omega')$. $\mathrm{P}(\Omega, \Omega')$ describes the probability of scattering the incoming beam (Ω') to the scattered direction $\Omega = (\Theta, \Phi)$. Forward scattering dominates in the optical regime, whereas no preference is apparent in the

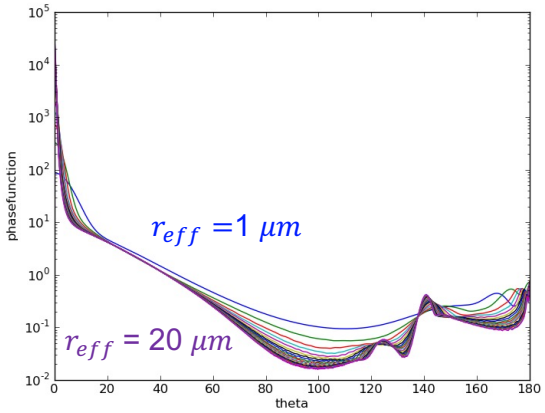

Figure 2.4: *Scattering phase functions for water droplets and different effective radii at one wavelength (550 nm) computed using Mie-theory (top). This plot is taken from the MIM-webpage under GNU Free Documentation License 1.3 (Emde, 2018).*

Rayleigh scattering regime. The phase function is usually rotationally symmetric. Forward scattering dominates in the optical regime $\chi >> 1$ (Fig. 2.4). However, the scattering phase function is relatively complex and depends on the shape of the hydrometeors, e.g. lower effective radii enhance backward scattering meaning a higher solar reflectance. It is even more complex for ice clouds as the scattering phase function also depends on the ice crystal's shape. Such non-spherical particles scatter more in sideways directions and into the backward scattering sector.

Combing Lambert-beer's law, the contribution of thermal emission and the scattering of the radiation gives the radiative transfer equation following Chandrasekhar (2013):

$$\frac{dI(\Omega)}{\beta_{ext} ds} = -I(\Omega) + \frac{\omega}{4\pi} \int P(\Omega, \Omega') I(\Omega') d\Omega' + (1 - \omega) B(T). \tag{2.28}$$

2.2.1 Approximations: MFASIS and RRTM

Eq. 2.28 can, in general, not be solved analytically. However, it is possible to solve the full 3D RT equation numerically, for example, by Monte-Carlo simulations (e.g. MYSTIC (Mayer, 2009)). For operational numerical weather prediction, Monte-Carlo simulations are too slow but would be very accurate. A balance between accuracy and computational cost is required.

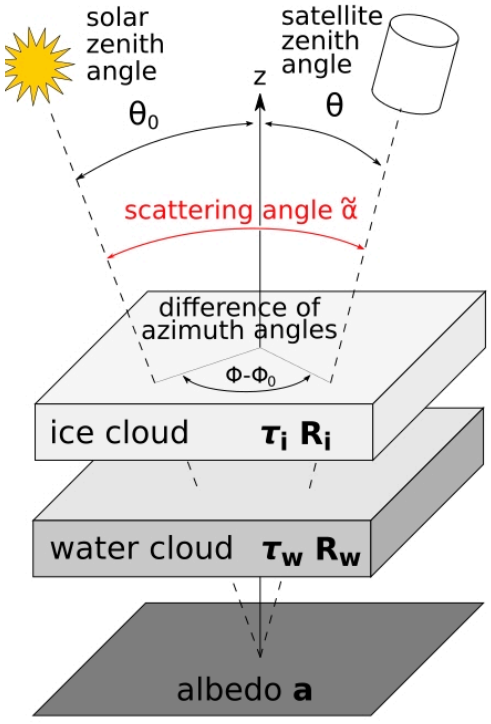

Figure 2.5: *Radiative transfer assumed in MFASIS: illustration of the scene ©Scheck.*

Due to the different nature of shortwave (solar) and longwave (thermal) radiation, the computation can be done independently. In the solar regime, scattering dominates in the atmosphere, whereas in the infrared regime, absorption and emission dominates. Next, the RT in the forward operator VISOP is described. Afterwards, the RT scheme in the used ICON version.

MFASIS

The Method for FAst Satellite Image Simulations (Scheck et al., 2016) is the RT solver used in this thesis to compute solar reflectances from model state (Eq. 2.19). The method is based on the work of Frèrebeau (2014). MFASIS determines solar reflectances at TOA by interpolating in a compressed look-up table with pre-computed values. The solar reflectances are computed using DISORT (Stamnes et al., 1988) that is implemented in libRADtran (Mayer and Kylling, 2005). MFASIS makes use of the fact that in the visible part of the spectrum, the reflectance is mainly determined by the total optical depth of the clouds. The vertical cloud structure (including variations in the effective radius of the cloud particles) has no strong influence on the reflectance. Therefore,

the cloud structure can be strongly simplified without causing large errors in the solar reflectance.

For the computation of the reflectances in the look-up table, it is assumed that two homogeneous and plane-parallel clouds are present: an ice cloud at 10 km height and below a water cloud at 4 km height. The basic strategy in MFASIS is to write the solar reflectance R as a function of the solar Θ_0 and satellite zenith angles Θ, the scattering angle α, the albedo a, and the optical properties of the water- (τ_w, r_w) and ice cloud (τ_i, r_i). The computation of the optical properties from the model state is described in Sect. 2.3.2.

RRTM

The Rapid Radiative Transfer Model (RRTM) uses a two-stream approximation and solves the radiative transfer in the used ICON-D2 model version (Zängl et al., 2015). Two-stream means only up- and downward radiative fluxes E (Eq. 2.20) are considered. In this solver, the shortwave radiation calculation is done by subdividing the electromagnetic spectrum into 14 bands (Mlawer et al., 1997) and in the longwave into 16 bands (Mlawer and Clough, 1997) to compute optical properties of clouds and aerosols. Cloud related model output is provided by the model's microphysics and for aerosols a climatological distribution is assumed (Tegen et al., 1997).

The RRTM in the ICON-D2 model assumes a plane-parallel atmosphere with 65 layers. Radiances are upward ($E^{\uparrow}$) and downward ($E^{\downarrow}$) fluxes in the shortwave (SW) and longwave (LW) parts of the spectrum. The computation of the fluxes is done for each atmospheric model layer to compute heating and cooling rates via

$$(\frac{\partial T}{\partial t}\rho c_p) = E^{\downarrow}_{SW,dir} + E^{\downarrow}_{SW,diff} - E^{\uparrow}_{SW,diff} + E^{\downarrow}_{LW} - E^{\uparrow}_{LW}. \tag{2.29}$$

The sum of $E^{\downarrow}_{SW,dir}$ and $E^{\downarrow}_{SW,diff}$ on the lowest model level gives the global horizontal irradiance [W/m^{-2}] and used fore evaluation.

2.2.2 Satellite observations

Weather satellites measure the scattered (solar) or emitted (thermal) radiances from the earth's surface or the atmosphere (e.g. hydrometeors, aerosols, water vapour). The main advantage of satellite observations is their high spatio-temporal resolution covering nearly every part of the globe. Hence, we get information about the weather situation also in remote areas like oceans. A second advantage is that we gain (complementary) information by using different sensors. For example, the SEVIRI instrument on board the Meteosat Second Generation measures radiances in specific channels. The 0.6 μm solar reflectance (VIS006) is highly sensitive to the liquid- and ice water path, whereas the 10.8 μm infrared brightness temperature (IR108) is less sensitive to the liquid- and ice water path but in addition to the cloud top height. In both VIS006 and IR108, the centered wavelength of the measured radiances lies within the atmospheric window (meaning that the clear-sky atmosphere is relatively transparent for radiation). Satellite sensors measure a combined signal (I_λ, see Eq. 2.18) of the ground ($I_{\text{clear-sky}}$) and clouds (I_{cloudy}) of a satellite pixel

$$I_\lambda = C \times I_{\text{cloudy}} + (1 - C) \times I_{\text{clear-sky}}, \tag{2.30}$$

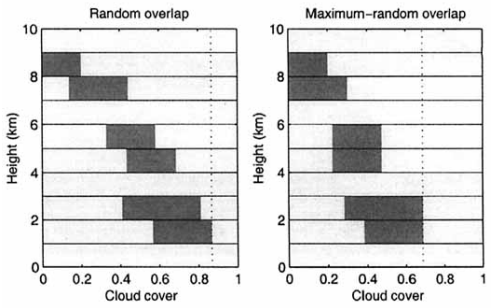

Figure 2.6: *Illustration of overlap assumptions, investigated in this thesis. This plot is taken and adapted from Hogan and Illingworth (2000).*

where C is the cloud cover of the pixel. Hence, getting the cloud-cover in weather simulation correct (with certain overlap assumptions) is essential in evaluating clouds. That is challenging since the effective model resolution is 5 - 7 Δx, which is 10-14 km for the ICON-D2 model runs considered in this work. Wood and Field (2011) showed that 85 % of global cloud cover comes from clouds larger than 10 km, based on high-resolution satellite observations. Most of the clouds should be resolved by current regional NWP models. However, a significant part of the total cloud cover is related to small clouds that affect the observed satellite radiances but are not resolved in the model. For this reason, parameterisations for unresolved clouds are crucial when comparing real and synthetic satellite observations. In this thesis, two overlap assumptions are tested to estimate uncertainty in VISOP (Fig. 2.6). The default assumption is random-maximum, where adjacent cloudy layers overlap maximally, while separated cloud layers overlap randomly. The random overlap assumes randomly overlapping clouds in the entire model column. The subgrid cloud overlap assumptions would not be a source of operator uncertainty if the assumptions in the NWP model and the operator assumptions were entirely consistent. However, RRTM in the used ICON version uses inconsistent overlap assumptions in the infrared and visible parts of the spectrum.

2.3 Clouds and their representation in NWP models

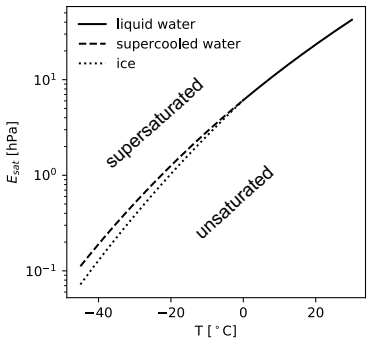

Figure 2.7: *Saturation water pressure over a plane surface of water against temperature for water and ice using Magnus formula.*

Clouds cover more than two thirds of the Earth's surface (King et al., 2013). Furthermore, clouds are one of the largest uncertainties in numerical weather prediction and climate models and strongly interact with radiation. The interaction of clouds and radiation influences the general atmospheric circulation, including the local convective-scale dynamics (e.g. Ingel, 2014). This section discusses cloud formation processes in the atmosphere and cloud-related parameterisations examined in this thesis. The description of this section follows mainly Wallace and Hobbs (2006) and Häckel (2016).

As a first approximation, an atmospheric cloud forms when the air is (super-) saturated, meaning a relative humidity RH $\geq$ 100%. The relative humidity RH = E/E_{sat} is defined as the fraction of the vapour pressure E and the saturation water pressure E_{sat}. E_{sat} over a plane water or ice surface is displayed in Fig. 2.7 and is computed using the Magnus formulas. The Magnus formulas are approximations of the Clausius-Clapeyron relation. Water vapour becomes (sub-) supersaturated through (warming) cooling by (down-) updrafts and radiative effects or adiabatic mixing of nearly saturated air parcels with different temperatures (description below).

Cloud formation processes and droplet/ice particle growth

The water phase in the atmosphere can be vapour, liquid and ice, depending on the thermodynamic equilibrium between water and the environment. A phase transition absorbs energy from or releases energy into the environment (Fig. 2.8). Latent heat release is one of the main sources of energy for global circulation, fronts and cyclones (Palmén and Newton, 1969).

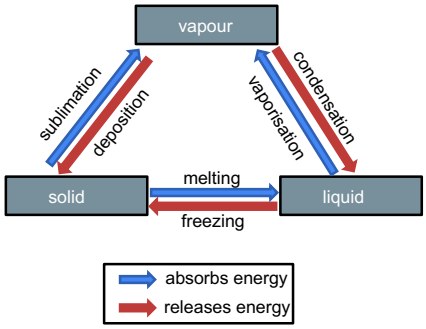

Figure 2.8: *Illustration of water phases and transitions in the Earth's atmosphere.*

Cloud water droplets form in the Earth's atmosphere if the air is (super-) saturated and in the presence of cloud condensation nuclei (CCN). This process is known as heterogeneous nucleation. In clean air, a relative humidity of several hundred per cent would be required to form clusters of H_2O molecules on the droplet's surface (homogeneous nucleation) because the saturation vapour pressure over a curved surface $E_{c,s}$ is greater than over a plane surface E_{sat}:

$$E_{c,s} = E_{sat}(T) exp(\frac{2\sigma}{nk_BTr}). \tag{2.31}$$

Hence, a droplet only forms if the air is supersaturated. The droplet radius after Kelvin's equation

$$r = \frac{2\sigma}{nk_BT\ln(\frac{E_{c,s}}{E_{sat}(T)})}, \tag{2.32}$$

depends on the surface tension σ, the temperature T and the fraction of vapour pressure E and saturation vapour pressure E_{sat} of the system. n is the number of water molecules per unit volume and k_B is the Boltzmann constant.

The Kelvin effect states that the lower the droplet radius for being in thermodynamic equilibrium, the higher the supersaturation must be. The surface tension of a liquid water droplet would force the water molecules to vaporise immediately after condensation, and only larger particles could survive in the atmosphere. That is where aerosols come into play as CCN. Aerosols can be small wettable, or water-soluble floating particles ranging from nano to some micro-meter sizes. Very effective is, for example, water-soluble sea salt (NaCl). When a water droplet contains dissolved material, the adjacent saturation vapour pressure E'_s is lower than for pure water droplets. Raoult's law describes this via

$$\frac{E'_{c,s}}{E_{c,s}} = f. \tag{2.33}$$

Here f is the mole fraction of water in the droplet f=$n_w/(n_w+n_s)$, with the number of water moles n_w and of the substance n_s. Combining the Kelvin effect (Eq. 2.32) and Raoult's law (Eq. 2.33) gives the Köhler equation:

$$\frac{E'_{c,s}(r)}{E_{sat}(T)} = \exp(\frac{2\sigma'}{n'kTr} - \frac{n_sM_w}{\frac{4}{3}\pi\rho_w r^3}). \tag{2.34}$$

For a fixed mass of dissolved material and small droplet sizes (e.g. $0.1\,\mu m$), Raoult's effect dominates, meaning that even below supersaturation, a droplet can survive. From Eq. 2.34, it becomes obvious that Raoult's effect decreases with increasing droplet radius as the solution becomes weaker ($\propto \frac{1}{r^{-3}}$) while Kelvin's effect becomes relatively more dominant ($\propto \frac{1}{r}$), leading to a peak in the Köhler curve. If the peak in the Köhler curve is below the supersaturation of the ambient air, the droplet will continue to grow (activated). The larger the particle, the lower the supersaturation can be to function as cloud condensation nuclei. That means that large aerosols are first activated. Analogously, larger droplets grow at the cost of smaller droplets. The higher the updraft velocity in a cloud, the more aerosols function as CCN (e.g. Politovich and Cooper, 1988). This indirect aerosol effect influences the optical properties of a cloud.

For raindrops, another crucial process plays an essential role. From theory, we know that taking only molecular diffusion into account, the condensation rate is too weak to form larger cloud and precipitating water droplets. The growth by collection is the dominant process that creates larger liquid droplet sizes. Larger droplets with more mass fall faster than smaller droplets as for relatively small particles in fluids, Stoke's friction plays a dominant role. Hence, larger droplets collide with smaller ones, and the collision efficiency can express the rate. The collection efficiency is the product of collision and coalescence rate because some droplets may bounce off one another.

For temperatures below 0, liquid water droplets can still exist. If such supercooled droplets and ice crystals coexist in a cloud, it is referred to as a mixed-phase cloud. Clouds that only consist of ice crystals are referred to as ice clouds. The situation for ice particle formation is analogous to water droplets, meaning to form a large enough particle to survive and grow. Here, an ice particle can grow from the water vapour (deposition, Fig. 2.8). In mixed-phase clouds, E_{sat} for ice is lower than for supercooled water droplets (Fig. 2.7). That means that the ambient air can be (super-) saturated over ice but subsaturated over water. Therefore, ice crystals grow at the cost of liquid water droplets because water droplets have to evaporate as the ambient air becomes relatively drier (Bergeron-Findeisen process). Through this process, various shapes (ice habits) can form like hexagonal or column plates.

Another process is growth by riming in mixed-phase clouds. Here, ice crystals collide with supercooled droplets that immediately freeze. So-called rimed ice crystal structures form. The last process is growth by aggregation. This process describes ice particle growth by colliding and aggregating. Similar considerations apply as discussed for the collision of water droplets. The effect of 'pure' column plates and aggregate habits on solar reflectance distribution is discussed in Sect. 4.3.2.

Adiabatic lifting processes

Air becomes saturated through adiabatic lifting, diabatic cooling or intrusion of water vapour. During mid-latitude summer, most clouds form through lifting processes if ascending air expands and thus cools adiabatically. Three types of lifting exist, leading to different cloud types:

(a) Convective clouds (e.g. Cumulus, Cumulonimbus): if the atmosphere is thermodynamically unstable, and thus an air parcel close to the earth's surface is relatively

warm. Convective clouds can be further divided into deep and shallow convective clouds (Stevens, 2005). Shallow convection means convective clouds in the atmospheric boundary layer, typically below 2 km height. These clouds are locally triggered or form along cold fronts. The vertical velocity may exceed several m/s, often causing heavy precipitation. Their spatial extension ranges from 100 m to 10 km horizontally and vertically, often up to the tropopause (in mid-latitudes approximately 10 km). The cloud water path of convective clouds is usually higher compared to stratiform clouds. The lifetime of these clouds ranges from minutes to some hours.

Local thermodynamic instability can be caused (triggered) by radiative heating of the earth's surface or damped by a cloud's shadows. Furthermore, Crook (1996) showed from numerical simulations that variations of 1 °C in temperature or 1 g/kg in boundary layer moisture were critical to whether storms formed or not. Moreover, Martin and Xue (2006) demonstrated that precipitation depends on positive ABL moisture perturbations O(1 g/kg) using an ensemble of more than 12000 meso-scale model forecasts.

The maximum intensity of convection can be expressed using the convective available potential energy

$$\mathrm{CAPE} = \int_{\mathrm{LFC}}^{\mathrm{LNB}} b dz, \tag{2.35}$$

with the level of free convection (LFC) and the level of neutral buoyancy (LNB). The buoyancy

$$b = -g\frac{T - T'}{T} \tag{2.36}$$

of an air parcel depends on the gravitational force g, its temperature T' and the environment's temperature T.

The moist static energy h of an air parcel is conserved during adiabatic ascent and descent

$$h = gz + c_p T' + Lq, \tag{2.37}$$

with the latent heat of vaporization L, the specific humidity q, the altitude above ground z and the specific heat at constant pressure c_p. Interestingly, a moisture increment of $\Delta\mathrm{q} = 1\,\mathrm{g/kg}$ has approximately the same effect as a temperature increment of $\Delta\mathrm{T} = 2\,\mathrm{K}$ (considering $L = 2000\,\mathrm{kJ/kg}$ and $c_p = 1\,\mathrm{kJ/(kg\ K)}$). This indicates that improving the temperature and humidity in the boundary layer (initially) should also enhance forecasting subsequent convective events.

(b) Stratiform clouds (e.g. Cirrostratrus, Altostratus, Nimbostratus) form when stable air ascents and often occur along warm fronts. Their spatial extent can exceed several 1000 km with low vertical velocities (some cm/s). Their lifetime is in the order of a day. The precipitation is less heavy than in convective clouds, but these clouds cause most rain amount in the mid-latitudes.

(c) Orographic clouds (e.g. Lenticularis) form when stable air masses are forced to rise. This process occurs if a horizontal flow crosses obstacles, e.g. the Alps. The cloud's lifetime is comparatively short.

Diabatic processes

Another cloud formation process in the atmosphere is through diabatic cooling. This happens when the air flows over the cold surface of the earth and fog forms (e.g. during the night in winter, the earth's surface radiates out). The intrusion of humid air can also cause cloud formation. This process often happens when relatively cold air flows over a relatively warm lake or ocean, where the air condensates directly above the water surface.

2.3.1 Cloud related parametrisations

Microphysics parametrisation is essential because it approximately describes the set of physical processes of formation, resolving, growth and fallout of hydrometeors. However, these processes are very uncertain and Seifert (2011) gives four main reasons: (1) microphysical processes occur on scales ranging from micro- (10^{-6} m) to millimetre (10^{-3} m) and hence on a wide range and not resolved by the model; (2) many processes are not well understood with gaps in the theoretical and empirical description; (3) the processes are highly non-linear and complex; (4) we lack in an adequate observation of cloud-related quantities to constrain model assumptions.

Next, a description of the microphysics and subgrid-scale clouds parametrisation in ICON-D2 is given. These parametrisations include a number of conservation equations for different hydrometeor categories. These equations are integrated by the model dynamics and include a number of source terms representing the interconversion (=mass transfer) between different hydrometeor types (e.g., riming, Bergeron-Findeisen process etc.). In addition, the conservation equation for some hydrometeors (rain, snow, hail) includes a sedimentation term to represent precipitation.

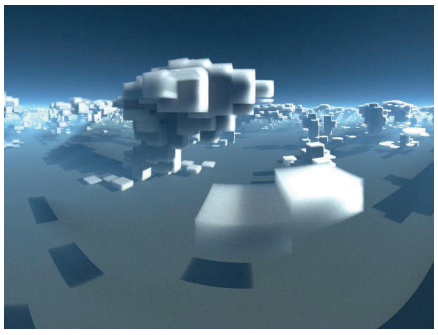

Figure 2.9: *Visualisation of a convective cloud of a EULAG simulation (2 km resolution), using MYSTIC. The plot is taken from Mayer (2018).*

The operational single-moment bulk microphysical parameterisation of the ICON-D2 model accounts for water vapour (q_v), cloud water (q_c), cloud ice (q_i), snow (q_s), rain (q_r) and graupel (q_g) (Lin et al., 1983, Reinhardt and Seifert, 2006). In the two-moment parameterisation of Seifert and Beheng (2006), the number concentrations N of different variables are also treated as prognostic variables. Hence, uncertainties related to the number concentration of clouds are reduced. An additional prognostic variable is hail (q_h). This is a more complex scheme and can potentially simulate more realistic clouds.

As described above, clouds can be divided into convective and stratiform clouds. Weisman et al. (1997) demonstrated that deep convective clouds are explicitly represented in NWP models with grid-spacing < 4 km. Therefore, deep convection is explicitly resolved in the ICON-D2 model with a horizontal grid-spacing of 2.1 km. However, this does not imply a realistic cloud representation (see Fig. 2.9) if only grid-scale clouds are considered.

Cloud parametrisation schemes are used to simulate the mean effect of processes below the model resolution. For example, from observations, we know that clouds exist, also if

the $\overline{RH}$ of a model grid box is below 100% (e.g. Wood and Field, 2011). The reasons are (moisture) fluctuations inside the grid box. Such diagnostic or subgrid-scale clouds can be represented in NWP models using PDF-based schemes (Sommeria and Deardorff, 1977). In the ICON-D2 model, the diagnostic cloud-cover scheme combines information from the turbulence (provides variability), microphysics (provides supersaturation) and shallow-convection scheme (provides cloud detrainment). This diagnosed cloud cover is input for RRTM. With grid spacing of O(100m) or below, clouds could be more realistically represented in numerical weather prediction models (e.g. Craig and Dörnbrack, 2008, Heinze et al., 2017).

Since clouds depend on nearly every parametrisation in an atmospheric model (Webb et al., 2001), some cloud-related parameterisations in ICON were modified within their physical plausibility to understand model cloud representation and to check the sensitivity of VIS and IR synthetic satellite observation to model changes. A brief introduction to the changes in the parametrisations is given next.

- The cloud-concentration number in ICON is used to calculate the cloud optical properties and influences the onset of precipitation. ICON employs the parameterisation of Segal and Khain (2006), which determines how many droplets are in a cloud depending on an aerosol number concentration derived from the climatology and on an updraft velocity at nucleation. The number of nucleated droplets increases with the updraft velocity. The determination of the updraft velocity in a 2 km resolution model is not straightforward because updrafts are underresolved. ICON assumes a constant updraft velocity, which serves as a control parameter.

- The turbulent subgrid-scale cloud parameterisation determines the cloud cover due to the unresolved variability in the model. The resulting turbulent cloud cover cc_{turb} is combined with the detrainment cloud cover, which is given by a diagnostic approximation of the equivalent term in Tiedtke (1993). We focus on the turbulent parameterisation of liquid clouds because those are the main source of subgrid-scale clouds in the summer period chosen for the experiments.

  The turbulent cloud parameterisation in ICON for liquid clouds is based on the assumption of an asymmetric probability distribution function (PDF) of total water (liquid + vapour). The used cloud-cover function starts from this assumption but has been empirically modified based on global and regional experiments (personal communication with Martin Köhler (DWD) in 2020). The final function reads

$$cc_{turb} = ((q_v + q_c + A\Delta q - q_{sat})/(B\Delta q))^2, \tag{2.38}$$

  where Δq is the variance of the total-water PDF, and it is determined by the turbulence scheme; A and B are tunable parameters that are described below; and q_{sat} is the water vapour at saturation using the mean temperature and pressure in the grid box. Some limiters and resolution-dependent corrections are applied to achieve the final cloud fraction but their description is irrelevant for this thesis.

  The parameter A determines the asymmetry of the size distribution: for larger A, clouds will be predicted at lower relative humidities, and so the cloud cover will be higher. This is a common tuning parameter when changing the model configuration.

For example, it is expected that the model requires less subgrid clouds as grid spacing is reduced and more clouds are resolved. The parameter B was introduced in this study and it scales the cloud cover for a determined PDF asymmetry. It thus allows for changing the cloud cover without modifying at which relative humidity clouds are activated. In the pre-operational ICON configuration it is set to A = 3.5 and B = 1 + A = 4.5.

- The shallow-convection parameterisation of Bechtold et al. (2014) predicts unresolved shallow convection in the model and also contributes to subgrid clouds. The model limits the parameterisation to clouds that are sufficiently thin so that thicker clouds have to be resolved by the model. The thickness of the thickest non-resolved cloud is thus an uncertain parameter that limits the strength of the parameterisation.

- The microphysical scheme describes the hydrometeors dynamics. This thesis checks the effect of using the two-moment parameterisation of Seifert and Beheng (2006), in which the number concentrations of different hydrometeors are treated as prognostic variables. This is a more complex scheme and can potentially simulate more realistic clouds. However, the two-moment scheme has never been tuned like the operational one-moment scheme.

2.3.2 Cloud-related model output and optical properties

The prognostic variables from the microphysics are grid-scale. The radiation scheme in ICON additionally uses the subgrid-scale contributions from the turbulent cloud parametrisation. This diagnosed cloud water q_c^{dia} and ice content q_i^{dia} is also a model output variable. We also need the prognostic pressure P, temperature T, density ρ to compute optical properties from the model output.

First, the liquid water content

$$\mathrm{LWC} = \frac{\mathrm{q_c^{dia}}}{\mathrm{clc}}\rho \tag{2.39}$$

and ice water content

$$\mathrm{IWC} = \frac{\mathrm{q_i^{dia}}}{\mathrm{clc}}\rho, \tag{2.40}$$

are computed, taking the pixel's cloud cover (clc) into account. LWC and IWC are used to compute the effective radii of water droplets $\mathrm{r_{w,eff}}$ after Martin et al. (1994):

$$\mathrm{r_{w,eff}} = (\frac{3}{4}\frac{\mathrm{LWC}}{\pi \mathrm{kN}\rho}). \tag{2.41}$$

Here, k=0.67 for continental clouds and N is the cloud droplet number concentration (default: N = 2x10^8 $\mathrm{m^{-3}}$) that determines reflective and cloud optical properties. However, a fixed value is unrealistic, as N depends on the number of cloud condensation nuclei. It is possible to use the two-moment scheme that explicitly computes N.

Given LWC and $\mathrm{r_{w,eff}}$, we can compute the extinction coefficient (Eq. 2.23) using a fit

function (with the determined coefficients a, b, c) after Hu and Stamnes (1993):

$$\beta_{ext}^{w} = \mathrm{LWC}(\mathrm{a}\,\mathrm{r}_{\mathrm{w,eff}}^{\mathrm{b}} + \mathrm{c}). \tag{2.42}$$

The computation of $\mathrm{r_{i,eff}}$ and its extinction coefficient is more complex because of the variety of shapes.

For ice crystals, with hexagonal columns shape the parametrization of Wyser (1998) can be used:

$$\mathrm{r_{i,eff}} = (\frac{4}{4+\sqrt{3}})(377.4 + 203.3\mathrm{B} + 37.91\mathrm{B}^2 + 2.3696\mathrm{B}^3)), \tag{2.43}$$

with $\mathrm{B} = -2{+}10^{-}3\ (273\mathrm{K}{-}\mathrm{T})^{3/2}\log(\frac{\mathrm{IWC}}{50g/m^3})$.
Here, the parametrization of Fu (1996) is used to compute the extinction coefficient

$$\beta_{ext}^{i} = \mathrm{IWC}(\frac{a_0 + a_1}{D_{ge}}), \tag{2.44}$$

where D_{ge} is the generalized effective size (see Eq. 2.3 in Fu (1996)) and a_0 and a_1 are determined using a fit function.

The computation of optical thickness as input for MFASIS (Sec. 2.2.1) of a water or ice cloud is straightforward by applying Eq. 2.24.

Chapter 3

Data and methods

This chapter describes the experimental model setup, the satellite observations, the calculation of model equivalents and the evaluation methods used in this thesis. Additionally, the sensitivity of satellite observations in the presence of clouds is discussed.

The first study (Chapter 4) uses hindcast simulations that are only driven by boundary conditions (BC) and initialized once in the beginning of the period. In this setup, clouds develop freely in the domain, but are constrained by analysis boundary conditions. This semi-free simulations are used to evaluate the model cloud climatology with satellite observations. Two forward operators compute model equivalents of VIS and IR MSG SEVIRI observations from the model output. Here, a high impact weather period with (seven) modified model settings and (five) operator settings is simulated. For the evaluation of solar reflectance assimilation, a summer period of four weeks in Central Europe with convective and stratiform clouds is simulated (results in Chapter 5). Two setups are compared, one with and one without assimilation of solar reflectances, using DWD's regional data assimilation and modeling system.

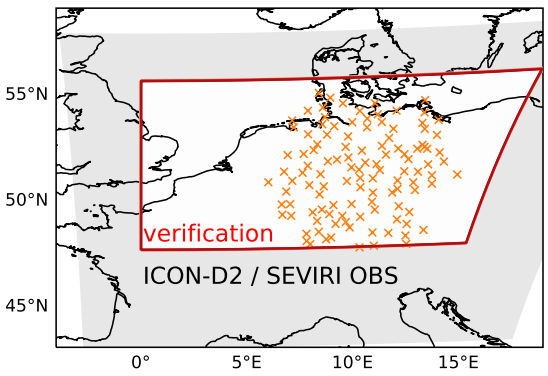

Figure 3.1: *ICON-D2 domain in observation space (gray shaded) and the reduced evaluation domain (red box). Orange x indicate DWD's pyranometer stations measuring global horizontal irradiance.*

3.1 ICON simulations

In this thesis, a pre-operational version of the ICON-D2 (ICOsahedral Non-hydrostatic, (Zängl et al., 2015)) model of Deutscher Wetterdienst was used. The ICON-D2 model is convection-permitting with prescribed lateral BCs. ICON-D2 replaced the operational COSMO-D2 model (Baldauf et al., 2018). The simulations over Germany and neighbouring countries (Fig. 3.1) have a horizontal grid spacing of 2.1 km with 65 vertical levels up to 22 km. Deep convection is explicitly simulated, whereas shallow convection is parametrized

(Bechtold et al., 2014).

3.1.1 Simulations to understand the model representation of clouds

The simulations are initialised once at 26 May 2016 00 UTC from downscaled ICON-EU analysis initial conditions. ICON-EU analysis BCs drive this semi-free simulations with an hourly update and a forecast horizon of 30 days. ICON-EU analyses are used to constrain the simulations at the boundaries. The simulation period and domain size are sufficiently large for the atmospheric model to develop its own cloud distribution without perturbations from data assimilation or nudging.

In order to investigate the sensitivity of synthetic satellite observations to these parameterisations and uncertain parameters, seven simulations are evaluated:

I Reference simulation with pre-operational model configuration.

II Increased cloud droplet number concentration by increasing the updraft velocity at activation (from 0.25 m/s to 1 m/s). This produces liquid clouds that are optically thicker as the number concentration of droplets increases roughly by a factor three.

III Modified distribution of turbulent subgrid liquid clouds. The idea is to produce less and thicker subgrid clouds in a way that the radiative balance of the model remains unchanged. This was achieved after a few trial and error experiments by using the parameters $A = 2.5$, $B = 0.21$.

IV Stronger shallow-convection parameterisation by doubling the thickness of the thickest unresolved cloud (from $2 \cdot 10^4$ to $4 \cdot 10^4$ Pa).

V Simulation with the two-moment scheme while all other parameterisations are equal to the operational configuration.

VI Two-moment scheme in which the subgrid-cloud parameterisation for ice clouds is switched off.

VII Two-moment scheme with strongly reduced asymmetry factor for subgrid-liquid clouds ($A = 1.5$, $B = 2.5$) and no subgrid ice-clouds. This simulation was motivated because the two-moment scheme reflected too much radiation, and therefore we reduced the amount of subgrid clouds.

3.1.2 Simulations for the assimilation experiment

For this study, the same model (ICON-D2) is employed, to simulate the weather in July 2019. Again, a pre-operational model version was used with the one-moment microphysics scheme. Different to the before-mentioned settings, boundary conditions from ICON-EU forecasts drive the nested domain to reflect the operational forecasting system and achieve an adequate spread in the analysis and first guess. ICON-EU forecasts have a horizontal grid-spacing of 6.5 km and deep convection is parametrized.

The two simulations VISCONV and CONV employ the KENDA system of DWD (see Sect. 2.1.3) with hourly cycling to construct the analysis (combination of observations

and first guess) and 40 ensemble members. Additionally, a deterministic analysis is computed using the Kalman gain from the ensemble mean (Eq. 2.17). In total 40+1 analyses are computed in each cycle. The analyses are computed using two sets of observations. Only conventional observations are assimilated in the quasi-operational simulation CONV, consisting of synoptic surface station, radiosonde, aircraft, and wind profiler observations (Fig. 3.2). VISCONV uses all the observations of CONV and additionally includes 0.6 μm SEVIRI solar reflectance observations from EUMETSAT's geostationary MSG satellite from 6 to 17 UTC (UTC + 2h = CEST). For the assimilation of solar reflectances, an observation error of σ_{obs} ≈0.14 is assumed with a horizontal localisation scale l_h=35 km. Additionally, superobbing is applied with a superobbing radius l_{so}=12 km. Therefore, a superobbed observation is the average of 4×2 satellite pixels (see Sect. 2.1.2). In both simulations, latent heat nudging is on.

The two deterministic VISCONV and CONV analyses are starting points for the deterministic 24-h forecasts. Forecast initialisation is every 6 hours at 0, 6, 12 and 18 UTC.

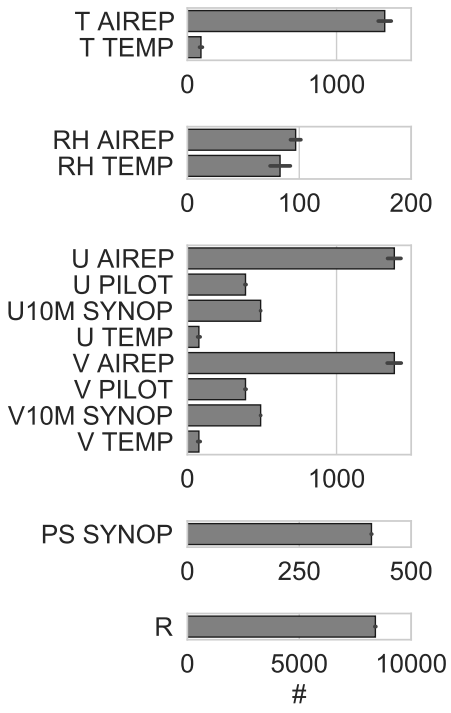

Figure 3.2: *Average number of observations at each analysis step (temperature T, relative humidity RH, zonal and meridional wind components U, V and surface pressure PS). Solar reflectance R observations are only used in VISCONV.*

3.2 Observations and model equivalents

3.2.1 Satellite observations

Observation

The SEVIRI instrument onboard METEOSAT Second Generation has eight channels in the solar and thermal part of the atmospheric window, with a spatial resolution of 3 km x 3 km at subsatellite point and about 6 km x 3 km in the ICON-D2 domain. The temporal resolution is 15 min for full disk scans (Schmetz et al., 2002). In the solar regime, radiances are dominated by scattering of photons from the sun to the satellite sensor, while emission of the earth's surface and cloud top is dominant in the thermal.

In this thesis, we use the visible 0.6 μm channel (VIS006), which has the advantage that at this wavelength the surface albedo is usually relatively low (R<0.15) and thus also errors in the albedo are smaller than for the 0.8 μm channel (VIS008) that would also be available from SEVIRI.

Additionally, we use the 10.8 μm thermal infrared window channel (IR108). At this wavelength, the signal is not strongly affected by gaseous absorption within the atmosphere and mainly determined by emission from the ground and clouds at all heights.

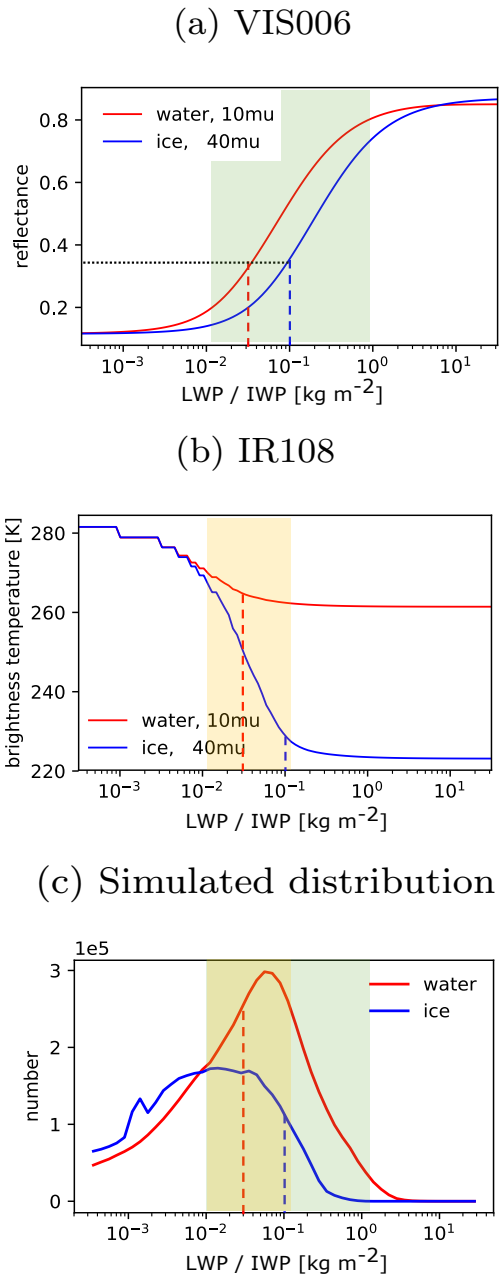

Figure 3.3: *Water and ice cloud signals with different effective particle radii from 0.6 µm SEVIRI solar reflectance (a) and 10.8 µm SEVIRI brightness temperature (b), computed using DISORT. Dashed lines indicate saturation in IR for water (red) and ice (blue) clouds. Coloured areas indicate the range of sensitivity for VIS (green) and IR (orange). The albedo is 0.1, sza is 30°, vza is 60° and α is 135°. (c) gives the simulated LWP and IWP at 12 UTC for the high-impact weather period of the reference run.*

The sensitivity of the VIS006 and IR108 signals to liquid and ice water paths (LWP, IWP) is shown in Fig. 3.3. The signals are computed using DISORT (DIScrete Ordinates Radiative Transfer; Stamnes et al. (1988)) for idealised scenes with a single-layer water cloud at the height of 4 km or a single-layer ice cloud at the height of 10 km (as assumed in MFASIS).

Both, solar reflectance and infrared brightness temperature strongly depend on LWP and IWP, but in different ranges: VIS006 is most sensitive to LWP/IWP-values in the range $[10^{-2}, 10^{0}]$ kg/m^2. In comparison, IR108's sensitivity is limited to thinner clouds with values in the range $[10^{-2}, 10^{-1}]$ kg/m^2, due to a fast saturation of the signal by the absorption of photons. Figure 3.3b implies that for a single-layer water cloud with LWP>0.03 kg/m^2 or a single-layer ice cloud with IWP >0.1 kg/m^2, only cloud top height and its corresponding temperature determines the observed BT. The IR signal can thus provide the cloud top temperature but does not allow for retrieving the LWP/IWP.

In contrast, the solar reflectance is about 0.35 at these threshold values and can still provide information on LWP/IWP values of up to 1 kg/m^2 (cumulonimbus clouds according to Kniffka et al. (2014)). These different and complementary sensitivities show that model evaluation with solar and thermal channels has the potential to provide more information on the nature of the systematic model errors and to identify specific shortcomings that would not be visible by only examining a single channel. The high sensitivity in VIS006 on a wide range is also valuable in updating cloud water paths during data assimilation, and the infrared signal could be used to adjust cloud top height.

As pointed out in Sect. 2.1.2, a linear approximation is applied to compute the analysis. From Fig. 3.3a it is clear that the measured signal is only linear in a certain range. However, the linear regime of the signal is where the largest sensitivity is (green area). Together with Fig. 3.3c it becomes evident that most of the liquid water

clouds (including the peak in the distribution) are in the linear regime. Only for very thick clouds (LWP> 1 kg/m^2) the signal is saturated and for very thin clouds the signal from the albedo dominates.

Model equivalent of solar reflectance

VISOP uses the fast 1D radiative transfer (RT) method MFASIS (Scheck et al., 2016) to compute model equivalents for visible satellite images from the ICON model state. The basic principle of MFASIS is described in Sect. 2.2.1. MFASIS is based on a compressed lookup table (LUT), computed using the DISORT solver, where the aerosol optical depth (AOD) is assumed to be zero. However, it is possible to consider aerosols or different kinds of ice habits for the computation of the MFASIS LUT (results in section 4.3.2). VISOP takes the slant satellite viewing angle into account (tilted independent column approximation of Wapler and Mayer (2008)). VISOP can account for the most important 3D RT effect by using the cloud top inclination correction (CTI) described in Scheck et al. (2018). The surface albedo values required as input for MFASIS are taken from the RTTOV-BRDF Atlas (Vidot et al., 2018).

The simulations in Chapt. 4 use r_{eff} directly as input from the model microphysics scheme to ensure consistency between RRTM, the microphysics and MFASIS. In the assimilation experiment, r_{eff} is parameterised as defined in Sect. 2.3.2.

In both experiments, ice clouds require some adjustments, as will be motivated in the following. Rain droplets, hail and graupel particles are assumed to be much larger than cloud droplets and cloud ice particles in the model. Therefore, for the same mass they are also much less effective in scattering radiation and are thus neglected in the forward operators. Model snow particles can be small enough to cause non-negligible scattering effects (see discussion in Hogan et al., 2001). The distinction

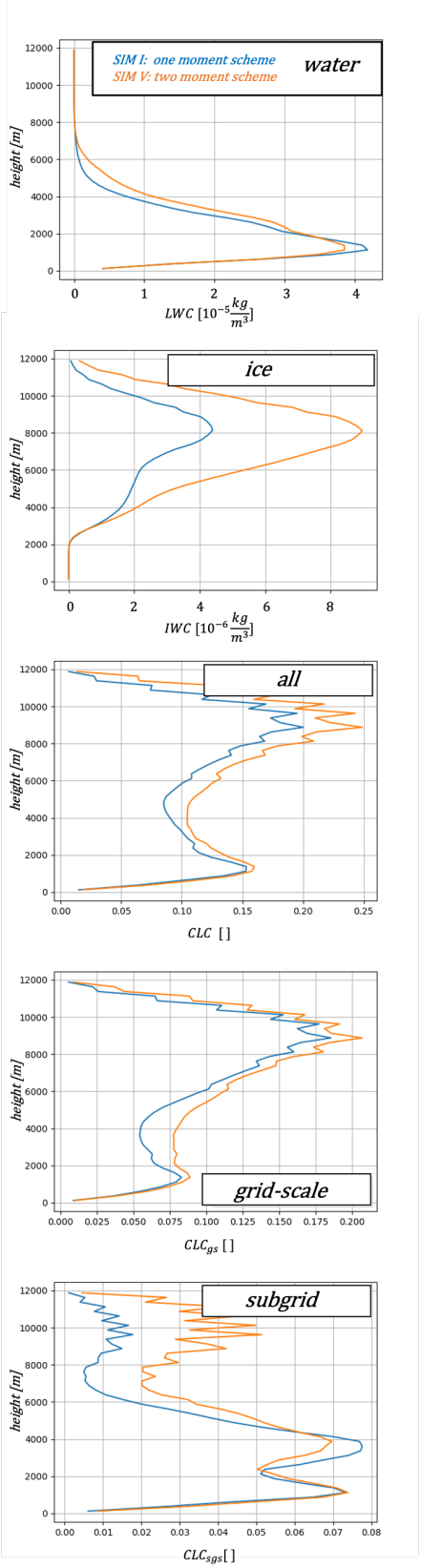

Figure 3.4: *Domain averaged model output of SIM I and IV using two microphysics schemes (Sect. 3.1.1) for binned layers (Δh=250m). From top to bottom: LWC, IWC, clc_{all}, clc_{gs}, clc_{sgs}*

between snow and cloud ice particles in the model is rather artificial. Interestingly, the two-moment scheme produces twice as much ice water content than the one-moment scheme and additionally more subgrid-scale ice clouds. (Fig. 3.4). This is to the expense of snow because the sum of ice and snow is comparable in both parametrizations. As an approximation, one can construct a frozen phase whose total mass, q_i^{tot}, is the sum of the diagnosed ice water content (grid and subgrid-scale) and snow content (only grid scale available) and whose "effective effective radius",

$$r_{i,eff}^{tot} = \frac{q_i^{tot}}{(q_i^{dia}/r_{i,eff} + q_s/r_{s,eff})}, \tag{3.1}$$

is defined using the simulated effective radii of cloud ice $r_{i,eff}$ and snow $r_{s,eff}$. The effective radii for ice and snow are calculated under the assumption that both hydrometeors behave as randomly-oriented needles, and using the mass-size relationships, size distributions and number concentrations from the microphysics (for details see Fu et al. 1997 and Muskatel et al. 2021). This approximation assumes that the optical thickness of the frozen phase is equal to the sum of the optical thicknesses of the ice and snow phases, similar as Senf and Deneke (2017). The approximation becomes exact in case of wavelengths much smaller than the hydrometeors size (optical limit), and therefore it is quite appropriate for visible channels.

In general, we use the diagnosed cloud water- and ice content including subgrid contributions as input for VISOP (see Sect. 2.3.2). If no subgrid-scale cloud is diagnosed in a particular grid box, then $q_x^{dia} = q_x$, where x could be either water or ice. We assume no differences in the microphysical and optical properties of grid and subgrid clouds, so that the effective radius calculation is the same for both cases.

Calibration of solar reflectance observation

An accurate calibration is a prerequisite for using satellite observations, but unfortunately the calibration of SEVIRI VIS006 is uncertain. Meirink et al. (2013), for example, found a bias of - 8 % for VIS006 during the years 2004 to 2008 by comparing MSG SEVIRI and MODIS (Moderate Resolution Imaging Spectroradiometer) Aqua observations. This calibration factor is also used for data assimilation experiments ($R_{obs}/ = 0.92$). In the hindcast simulations, the approach to find a suitable bias correction by minimising the average difference between probability density functions (PDF) of observed and simulated solar reflectance is used. This gives a deviation of -13 % between observations and the reference simulation, which can be partly contributed to a calibration offset (observation too dark) and a model/operator bias. Through this approach, the highest observed and simulated solar reflectances are in better accordance and the model changes can be more easily examined.

Model equivalent of infrared brightness temperature

To derive SEVIRI infrared brightness temperature from the model state, we use the efficient methods implemented in the RTTOV 12.1 package (Saunders et al., 2018) that is used by many weather services.

For the evaluation, we follow Marseille and Stoffelen (2017) and apply both operators at the full model resolution. Afterwards, these synthetic satellite images are interpolated to observation space to avoid additional representativeness errors (see Sect. 2.1.2).

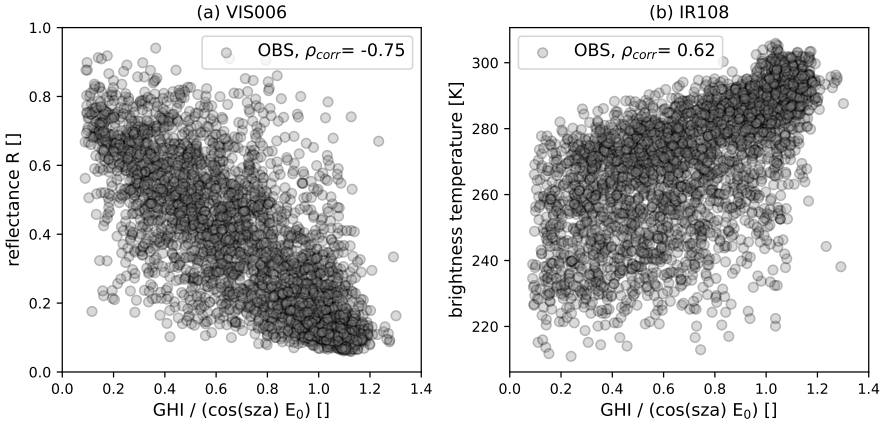

Figure 3.5: *0.6 µm SEVIRI solar reflectance (VIS006) (a) and 10.8 µm SEVIRI brightness temperature (IR108) (b) against fraction of incoming global horizontal irradiance (GHI/(cos(sza) E_0)) in May/June 2016 at 12 UTC. Here, E_0 (solar constant) is assumed to be 1367 W/m^2 and the number of collocated observations at pyranometer stations is 3365.*

3.2.2 Global horizontal irradiance

Observation

Global horizontal irradiance (GHI) at the earth's surface is the total amount of shortwave radiation and includes both direct normal irradiance (DNI) and diffuse horizontal irradiance (DHI). Deutscher Wetterdienst operates a dense network of GHI observations across Germany. GHI is an hourly average and is evaluated at 122 pyranometer surface stations (Fig. 3.1). The accuracy of the observations depends on the instruments: 26 stations are equipped with secondary standard CM-11 and CM-21 pyranometers and 96 stations utilize SCAnning Pyrheliometer/Pyranometer. For evaluation, only observed GHI-values greater than 75 W/m^{-2} are considered as suggested by Behrens et al. (2005).

One would expect visible reflectance to provide more information on the transmittance of solar radiation to the surface than infrared radiances, as attenuation and scattering properties strongly dependents on the cloud water path. Visible reflectances should therefore be more strongly correlated with the incoming radiation at the surface than infrared brightness temperatures. This is confirmed by Fig. 3.5, which displays the correlation between the observed signals of the two satellite channels and normalized hourly averages of the global horizontal irradiance GHI measured at 122 DWD pyranometer stations (Fig. 3.1). There is indeed a strong negative correlation of solar reflectance with surface radiation, with a correlation coefficient ρ_{obs} = -0.75 (Fig. 3.5a). It can be assumed that the true correlation of reflectance and GHI is even closer to -1 given that the comparison of the two quantities is also affected by the following factors: (1) the instantaneous solar reflectance is compared to the hourly-averaged quantity GHI, (2) reflectance is averaged over pixels

while GHI is a point measurement and (3) 3D radiative transfer effects affect reflectance and GHI in different ways. For constant water content, surface radiation should not be strongly correlated with the cloud top height or temperature. However, as many high clouds are caused by convection and these clouds contain large amounts of water, there is also some correlation between brightness temperature and surface radiation (Fig. 3.5b), but it is weaker ($\rho_{obs} = 0.62$) than for the visible reflectances. These results indicate that improving model forecasts of solar reflectance will also improve model forecasts of surface irradiance.

Model equivalent

The model's radiative transfer scheme RRTM (see Sect. 2.2.1) simulates DNI and DHI (Mlawer et al., 1997, Mlawer and Clough, 1997). Global horizontal irradiance is the sum of both contributions.

In Sect. 5.4.1, the error dependencies between solar reflectance and global horizontal irradiance are shown. In order to reduce sampling errors (e.g. moving clouds) a super-observation is computed for solar reflectance by averaging the nine nearest satellite pixels to a Pyranometer station.

3.2.3 Precipitation and conventional observations

This thesis uses quality controlled radar-derived hourly precipitation rates (mm/h) of DWD's so-called RY product (DWD, 2020b, 2021d). Radar reflectivity is observed at 17 operational weather radars with a spatial and temporal resolution of 1 km x 1 km and 5 min, respectively and a spatial extend of 900 km x 900 km. The hourly precipitation rate is a prognostic variable in the ICON model. Precipitation can be divided into three categories depending on the precipitation rate rr [mm/h]: light and measurable ($0.1<rr<0.5$), moderate ($0.5\leq rr< 4$) and heavy precipitation ($rr\geq 4$) (Koppe and Stozek, 1999).

Conventional observations are prognostic variables and are explicitly computed by the model. We exclude AIREP temperature observations for the evaluation because these observations exhibit systematic errors, depending on the individual aircraft (see, e.g. Necker et al. (2018)). Furthermore, AIREP relative humidity observations are excluded because the number of observations is very small (Fig. 3.2).

3.3 Evaluation method

A set of metrics is applied for the model evaluation. In both parts of this thesis, the evaluation domain (red rectangle in Fig. 3.1) is smaller than the ICON-D2 domain to exclude nesting effects at the domain boundaries and signals from snow-covered alps that exhibit reflectances similar to clouds. In the first study, probability density functions are helpful to better understand the model representation of clouds. The comparison of PDFs highlights systematic deviations and reveals shortcomings of the model. The number of bins N of the PDFs is 50, with $R\in[0,1]$ and $BT\in[200,310]$ K. From that, we define the cloudiness (C) as the fraction of pixels in which the solar reflectance is higher than a threshold value R_c of 0.2. This value is an upper limit for clear-sky reflectance in the

considered verification domain (Fig. 3.6). Violin plots are used to visualize the daily bin-by-bin deviation of the PDF (deviation computed for each day d and bin n) from the reference run and model/operator sensitivity experiments: $\epsilon^{\mathrm{PDF}}_{\mathrm{n,d}} = \mathrm{P(R)}^{\mathrm{obs}}_{\mathrm{n,d}} - \mathrm{P(R)}^{\mathrm{sim}}_{\mathrm{n,d}}$. This allows for a consistent comparison of VISOP and model uncertainty, by examining the median deviation (the mean is always zero), the interquartile range (difference between 75th and 25th percentile) as a measure for variability and the range as the extent of deviations. We further analyze clouds by constructing contoured 2D PDF plots of brightness temperature and solar reflectance, comparable to the ISCCP-approach (Rossow and Schiffer, 1991) or to contoured frequency by altitude diagrams (CFADs, Yuter and Houze Jr (1995)) of radar observations. We use the US. Standard Atmosphere 1962 (Sissenwine et al., 1962) to classify brightness temperatures into three cloud categories (low, middle and high clouds) as defined in the International Cloud Atlas (Cohn, 2017). In the US Standard Atmosphere, the surface temperature is 288 K and the (wet) temperature lapse rate is 0.65 K/100 m, leading to temperature ranges of $\mathrm{T} > 275\,\mathrm{K}$ for the surface and low clouds, $275\,\mathrm{K} \leq \mathrm{T} \leq 243\,\mathrm{K}$ for middle clouds and $\mathrm{T} < 243\,\mathrm{K}$ for high clouds.

To assess the influence of solar reflectance assimilation on analysis and forecast skill, the following commonly-used metrics are calculated: The Mean Absolute Error

$$\mathrm{MAE} = \frac{1}{N}\sum_{i=1}^{N}|m_i - o_i|, \tag{3.2}$$

where m and o represent the model and observation, respectively, the Mean Difference

$$\mathrm{MD} = \frac{1}{N}\sum_{i=1}^{N} m_i - o_i, \tag{3.3}$$

the Root Mean Squared Error

$$\mathrm{RMSE} = [\frac{1}{N}\sum_{i=1}^{N}(m_i - o_i)^2]^{1/2}, \tag{3.4}$$

and the Fractions Skill Score (Roberts and Lean, 2008)

$$\mathrm{FSS} = 1 - \frac{\frac{1}{N}\sum_W (P_m - P_o)^2}{\frac{1}{N}[\sum_W P_m^2 + \sum_W P_o^2]}, \tag{3.5}$$

where P_x is the fraction of pixels exceeding a certain threshold and W is the number of spatial windows in the domain.

The Pearson's correlation coefficient

$$\rho = \frac{cov(m,o)}{\sigma_m \sigma_o} \tag{3.6}$$

is computed from the covariance *cov* between model and observation and the correpsonding standard deviations σ_x. Surface irradiance error evolution follows the diurnal cycle. In order to give a fair comparison of predicting surface irradiance in the presence of clouds,

the normalized Mean Absolute Error is computed via

$$\mathrm{nMAE} = \frac{\mathrm{MAE}}{\sum_{i=1}^{N} o_i}. \tag{3.7}$$

Furthermore, the Percentage Improvement (PI, following Schraff et al. (2016)) is computed between our reference simulation CONV and VISCONV:

$$\mathrm{PI} = \frac{\epsilon_{\mathrm{CONV}} - \epsilon_{\mathrm{VISCONV}}}{\epsilon_{\mathrm{CONV}}}. \tag{3.8}$$

A positive value indicates an improvement in VISCONV with respect to the considered metric.

Finally, four categories should be defined using joint distribution to quantify the error reduction in the 2D cloud field. The four combinations are computed between observation and first guess and between observation and analysis at each data assimilation step:

CN correctly negative: $R_{obs} < R^{cs}$ and $R_{model} < R^{cs}$

H hit: $R_{obs} \geq R^{cs}$ and $R_{model} \geq R^{cs}$

M miss: $R_{obs} \geq R^{cs}$ and $R_{model} < R^{cs}$

FA false alarm: $R_{obs} < R^{cs}$ and $R_{model} \geq R^{cs}$

R^{cs} is the clear-sky reflectance.

One can employ a fixed reflectance threshold to distinguish cloudy from clear-sky pixels (see description above). This approximation excludes all clear-sky pixels but also some semi-transparent clouds (particularly over the ocean). Fig. 3.6 shows the clear-sky reflectance R^{cs} distribution.

Another approach that is used in Sect. 5.2.1 is to exploit the clear-sky reflectance directly to distinguish a cloudy from a clear-sky pixel i, if

$$R_i - R_i^{\mathrm{cs}} < \epsilon^{cs}. \tag{3.9}$$

Here, a certain error ϵ^{cs} must be assumed, because the used forward operator is not perfect and no aerosols are considered in the computation of the analysis and first guess solar reflectance, respectively. As estimated in Sect. 4.3.2, the clear-sky solar reflectance error introduced by neglecting aerosols is approximately 0.1. In this thesis, ϵ^{cs} is assumed to be 0.1 as retrievals from AERONET (Giles et al., 2019) measurements over Germany give a similar AOD for both investigated periods (AOD≈0.1 for each satellite pixel).

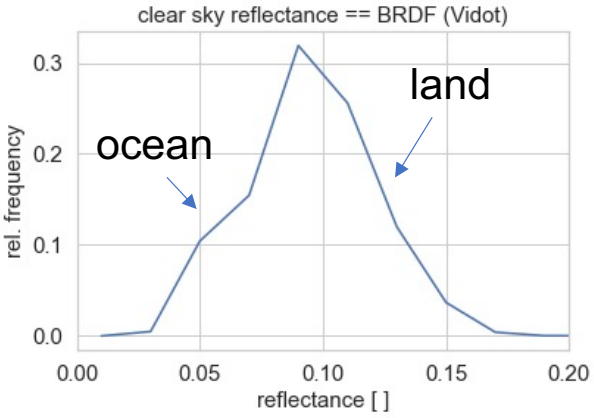

Figure 3.6: *Distribution of clear-sky reflectance, computed using VISOP and the RTTOV BRDF-Atlas of the ICON-D2 domain for July 2019 at 12 UTC.*

Chapter 4

Understanding the model representation of clouds based on visible and infrared satellite observations

This chapter demonstrates the benefits of using visible and infrared satellite channels to evaluate clouds in numerical weather prediction models. Two forward operators are applied to compute synthetic MSG SEVIRI satellite observations from the model state. First, two selected days of the period are discussed with clouds on different levels to introduce the approach. Afterwards, the full test period's statistics reveal systematic deviations between observed and synthetic satellite observations. Different hydrometeor types and subgrid-scale clouds contribute to the 1D solar reflectance PDF. Their influence is assed to understand the sensitivity of solar reflectances better. Subsequently, the sensitivity of synthetic satellite images to model and visible operator settings is estimated, and for solar reflectances, the model and operator uncertainties are compared.

4.1 Investigation period

A 30-day period from 26 May to 24 June 2016 is evaluated, which is dominated by strong summer-time convection in Germany. In the beginning, large parts of Europe were affected by high-impact weather events over almost two weeks. Atmospheric blocking and interaction of low thermal stability and weak mid-tropospheric winds were the ingredients for this exceptional sequence of thunderstorms and related flash floods (Piper et al., 2016). Many authors have discussed these two weeks (see e.g. Necker et al. (2020), Bachmann et al. (2020),

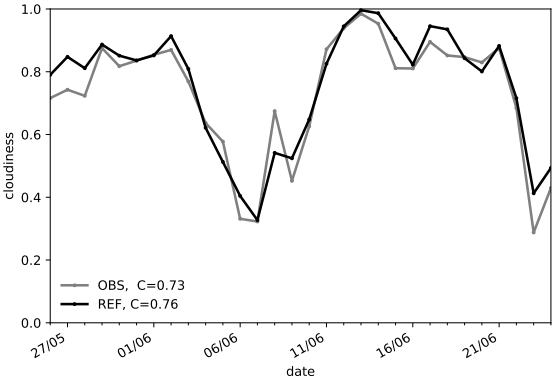

Figure 4.1: *Time series of observed and simulated cloudiness at 12 UTC during period (26 May - 24 June 2016). The cloudiness is defined as the fraction of pixels where 0.6 μm SEVIRI solar reflectance R>0.2.*

Keil et al. (2019), Necker et al. (2018), Zeng et al. (2018)). In the subsequent weeks (10. - 24. June), the wind direction changed to south-westerly flow, advecting warm and humid air masses from the Atlantic and the Mediterranean to Germany and supporting cloud formation (Fig. 4.1). In general, the simulated cloudiness (defined in section 3.3) is predominantly overestimated, leading to a period mean observed and simulated cloudiness of 0.73 and 0.76, respectively. This convective period with high cloud cover at different levels is well suited to examine the cloud climatology and its sensitivity to cloud-related parameterisations.

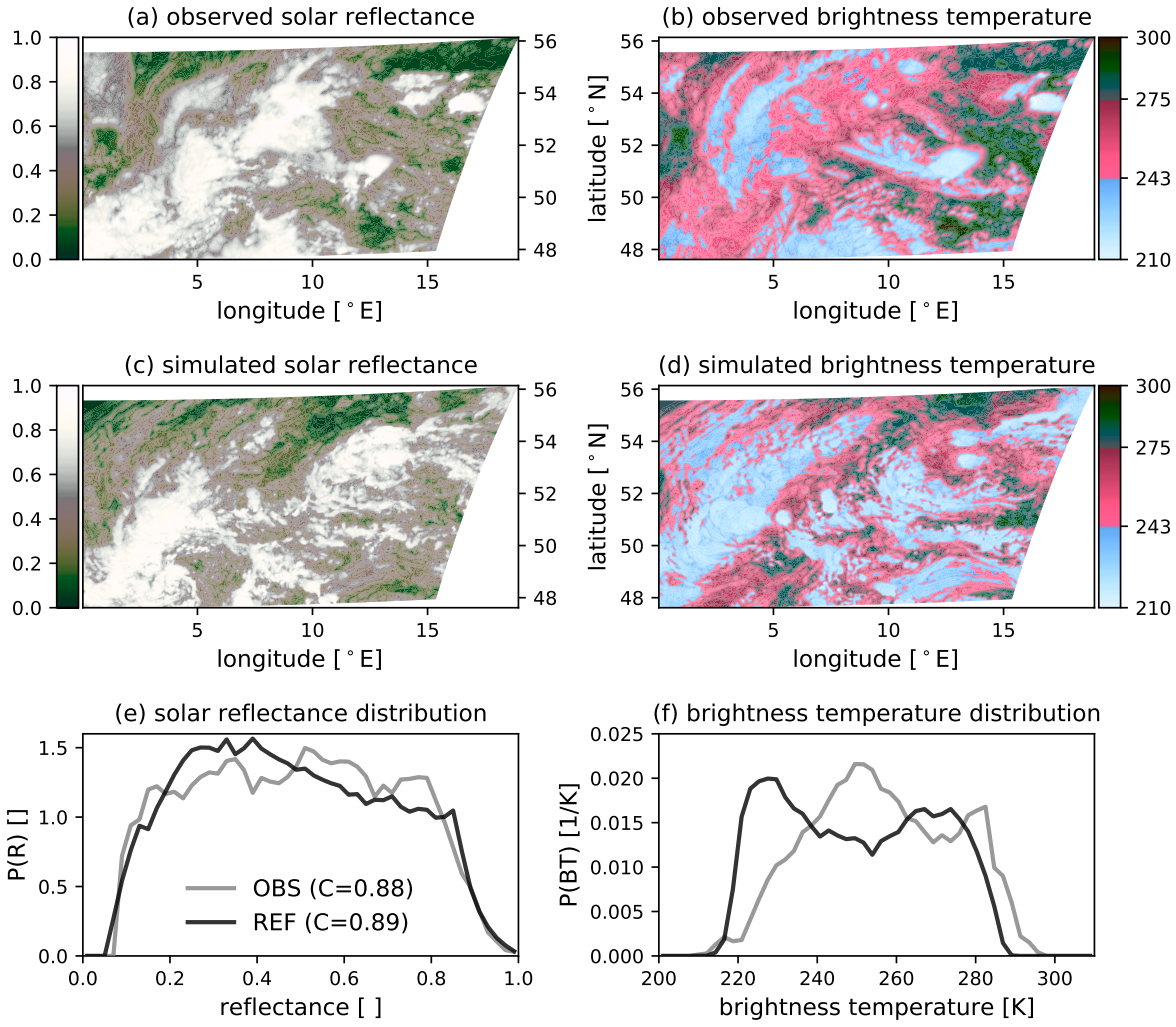

Figure 4.2: *(Regional) distribution of 0.6 µm SEVIRI solar reflectance (left) and 10.8 µm SEVIRI brightness temperature (right) and their corresponding distribution for 29 May at 12 UTC. Different colors in the colorbar indicate for solar reflectances approximately: clear-sky R∈(0.2), semi-transparent to medium thick clouds R∈[0.2,0.5) and thick clouds R∈[0.5,1] and for brightness temperature: clear-sky and low level-clouds BT∈[300,275), mid-level clouds BT∈[243,275] and high-clouds (243,210]. The numbers in the legend of (e) indicate the cloudiness, i.e. the fraction of pixels exceeding a reflectance of 0.2. (EUMETSAT)*

4.2 Visible and infrared satellite observations

4.2.1 Selected cases

In this section, two days of the period are discussed to illustrate the methodology of evaluating clouds using visible and infrared satellite channels. On the first one (29 May), deep convection and severe thunderstorms occurred leading to a flash flood that caused severe damage in Braunsbach, a small town in the south-western part of Germany. The second one (02 June) was dominated by low-level clouds. According to Piper et al. (2016), warm, moist and unstable air masses characterized both days. However, large-scale ascent dominated on 29 May and subsidence on 02 June.

Figure 4.2 shows the VIS006 and IR108 satellite images, together with the corresponding distributions of solar reflectance and brightness temperatures on 29 May 2016. The VIS006 satellite image (Fig. 4.2a & 4.2c) shows the early stage of a cyclogenesis over Germany, characterized by a prominent vortex structure, in both the observation and model simulation. However, the feature is shifted to the south-west in the simulation. The relatively high cloudiness of 88 % in the observation and 89 % in the simulation leads to a relatively uniform distribution of observed solar reflectances (Fig. 4.2e). Overall, the agreement between observed and simulated visible histograms is relatively good given that the model is forced towards the current weather only through the boundary conditions. The vortex structure of the cyclogenesis is also apparent in the IR108 observation (Fig. 4.2b), but the simulation shows clear systematic errors. In the simulation, the cloud pattern is dominated by relatively high ice clouds (Fig. 4.2d), which are less frequent in the observations. The histogram confirms this picture: The signal of high clouds is overestimated in the simulations, whereas the signal of medium clouds is underestimated by 40 %.

On 02 June 2016, boundary layer clouds dominated in both the observation and simulation (Fig. 4.3b&d). Additionally, superimposed ice clouds are observed in some regions. The simulated IR108 distribution fits the observed one relatively well on this day (Fig. 4.3f). In the visible satellite image (Fig. 4.3a&c), a high cloudiness is apparent, with 87 % in the observation and 91 % in the simulation. Different to 29 May, however, the distribution (Fig. 4.3e) reveals an overestimation of medium-thick clouds, together with an underestimation of thick clouds (R>0.6).

The examples discussed above show that the examination of a single channel (VIS or IR) can lead to opposite conclusions with respect to forecast quality. The agreement of the histograms for 29 May is good in the visible range but not in the IR. The opposite is observed for the 02 June. This shows that both channels provide complementary information. In the following, we show that further information can be obtained by using the combined information of both channels in 2D PDF plots of brightness temperature and reflectance. We have already discussed how the IR histogram shows an overestimation of high clouds on the 29 May. The combined histograms (Fig. 4.4a & 4.4c) provide the additional information that this overestimation of clouds mostly happens for thick clouds (R>0.6). This indicates that the model produced too strong deep convection.

On 02 June, where lower clouds dominated the scene, the observation and simulations agree on the vertical location of the shallow cumulus clouds (Fig. 4.4b & 4.4d). However, solar reflectances are primarily distributed around 0.7 in the observation and around 0.5 in the simulation. Compared to the 1D reflectance histogram, the 2D PDF provides the

additional information that the systematic reflectance errors are related to low clouds. These two days with predominantly deep convective clouds (29 May) and low clouds (02 June) are exemplarily for different cloud types and formation processes. Their evaluation therefore illustrates the benefit of combining a visible and an infrared channel.

4.2.2 VIS006 and IR108 statistics for the full period

The analysis of individual cases presented above illustrates certain characteristics, but longer periods are required to identify systematic model deficiencies. To address this, we now present results for the 30-day period. The observed mean VIS006 solar reflectance

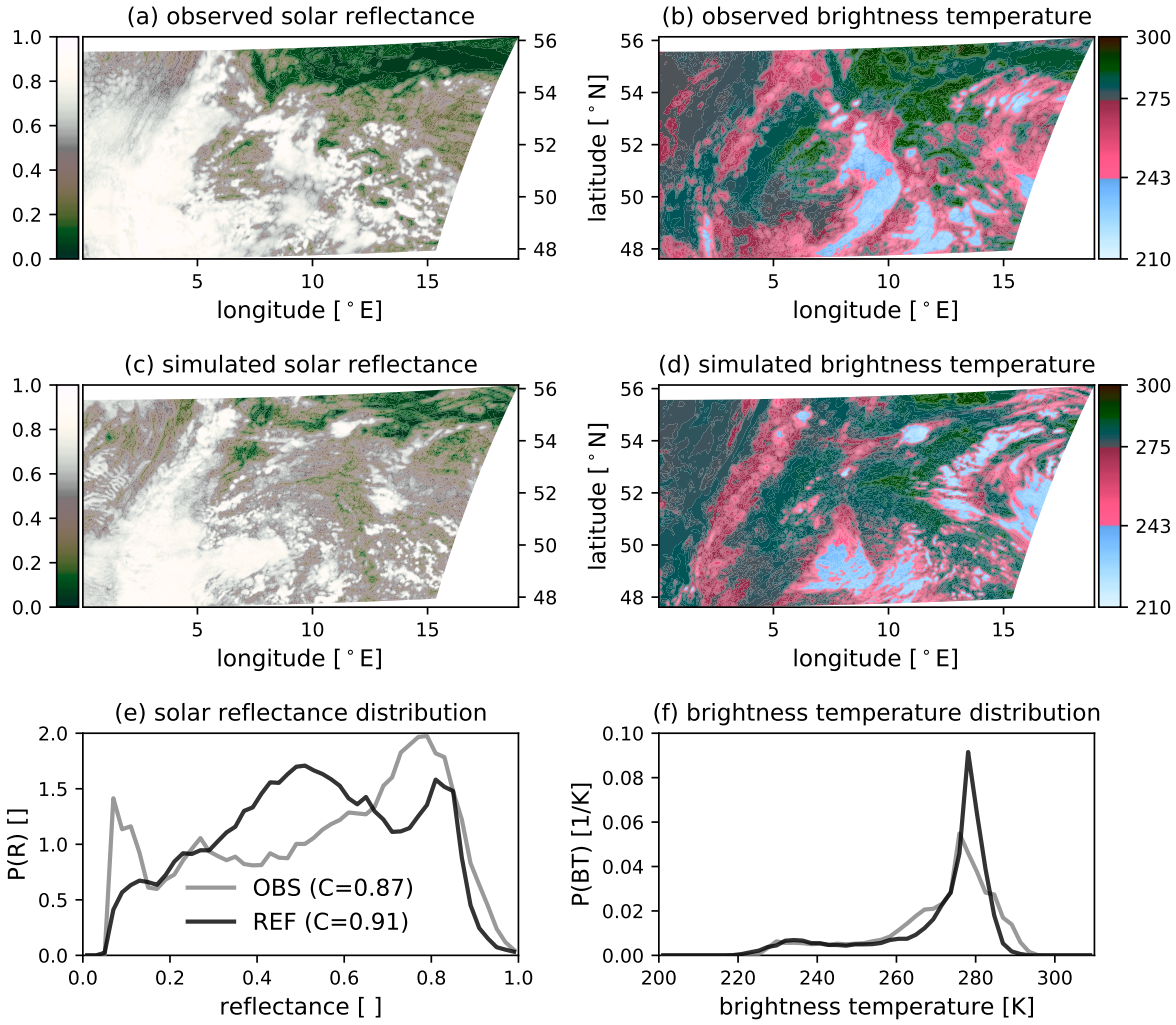

Figure 4.3: *(Regional) distribution of 0.6 µm SEVIRI solar reflectance (left) and 10.8 µm SEVIRI brightness temperature (right) and their corresponding distribution for 02 June 2016 at 12 UTC. Different colors in the colorbar indicate for solar reflectances approximately: clear-sky R∈(0.2), semi-transparent to medium thick clouds R∈[0.2,0.5) and thick clouds R∈[0.5,1] and for brightness temperature: clear-sky and low level-clouds BT∈[300,275), mid-level clouds BT∈[243,275] and high-clouds (243,210]. The numbers in the legend of (e) indicate the cloudiness, i.e. the fraction of pixels exceeding a reflectance of 0.2. (EUMETSAT)*

distribution at 12 UTC reveals a clear-sky peak at low reflectance values (R ∈ [0, 0.2]), a nearly uniform distribution for higher reflectances (R ∈ [0.2,0.8]) and a sharp decrease for reflectances higher than 0.8 (Fig. 4.5a). The distribution of the reference simulation overall looks similar, but shows some deviations from the flat plateau seen for the observations, with a surplus of clouds around a reflectance 0.5. Fig. 4.5b presents a histogram of the 30-day mean IR108-BT at 12 UTC. There are generally too many clouds with low brightness temperatures (BT<240K). This, together with an underestimation of mid-level clouds in our ICON simulations is a well known issue that has been found for many global circulation or weather prediction models using forward operators or retrievals for evaluation (e.g. Illingworth et al., 2007, Pfeifer et al., 2010, Böhme et al., 2011, Franklin et al., 2013, Keller et al., 2016) . Zhang et al. (2005) discusses possible reasons for the lack in mid-level clouds and concluded that physical deficiencies in the model might introduce these systematic deviations. The distribution further reveals a clear-sky bias, where the model underpredicts high BT values.

In general, the statistics for the full period, as shown by the 2D PDFs in Fig. 4.5c & 4.5d, indicates that the model and observation distributions have similar structures.

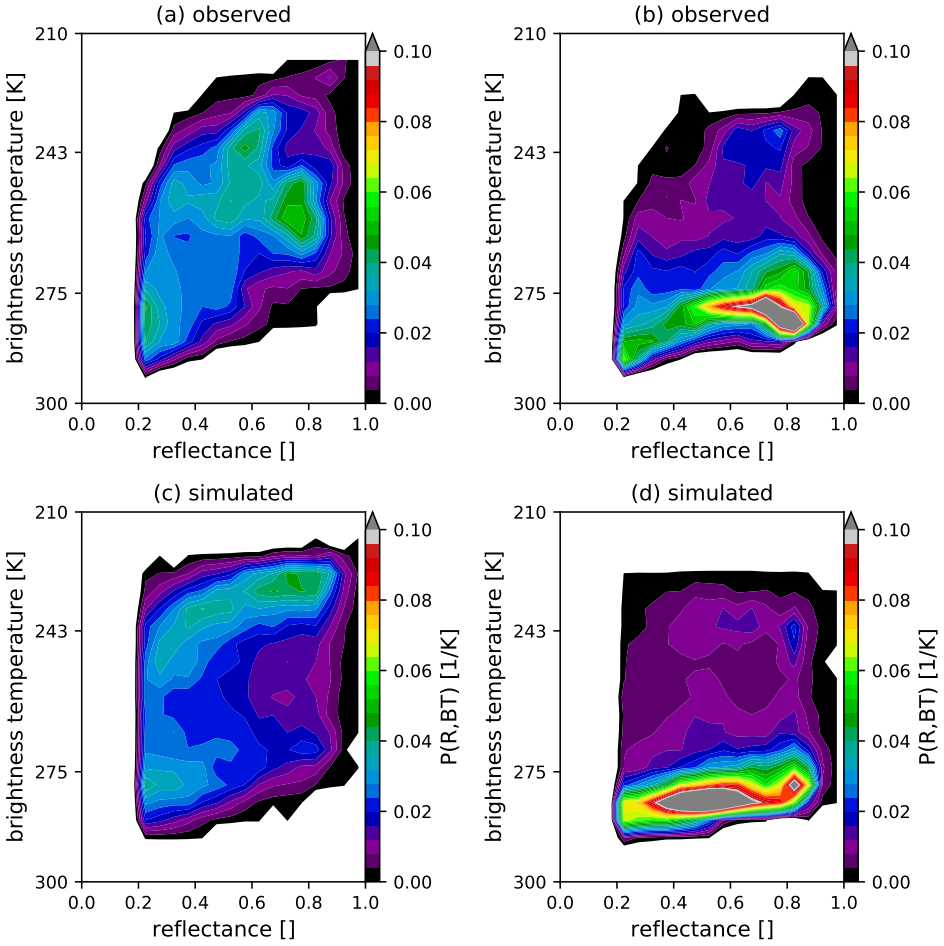

Figure 4.4: *Combined 0.6 µm SEVIRI solar reflectance (VIS006) and 10.8 µm SEVIRI brightness temperature (IR108) PDF of observations (top) and simulations (bottom) at 29 May (left) and 02 June 2016 (right) at 12 UTC.*

Noticeable differences in the distribution occur in boundary-layer clouds. The increase in solar reflectance with decreasing brightness temperature (increasing height) is noticeably steeper in the observations (indicated by dashed white lines in the plots). This means that thick boundary-layer clouds consistently reach higher levels in the observations, and suggests that shallow convection is too weak in the model. The 2D PDFs further indicate that the surplus of clouds around a reflectance of 0.5 in the model is related to boundary layer clouds, revealing a deficiency in the model representation of liquid water clouds. In addition, the simulation lacks in producing enough mid-level clouds at all solar reflectances. Finally, a secondary maximum at low BTs and high solar reflectance (R≈0.8) is apparent in the simulations but not in the observations. This maximum mainly corresponds to deep convective and precipitating clouds, which are either too active or produce too much ice, similar to 29 May. High-level clouds (cirrus as well as iced cloud tops) and low-level clouds are generally overestimated.

The combined histograms clearly show important shortcomings in shallow and deep convection. Combined histograms can thus provide additional information on the nature

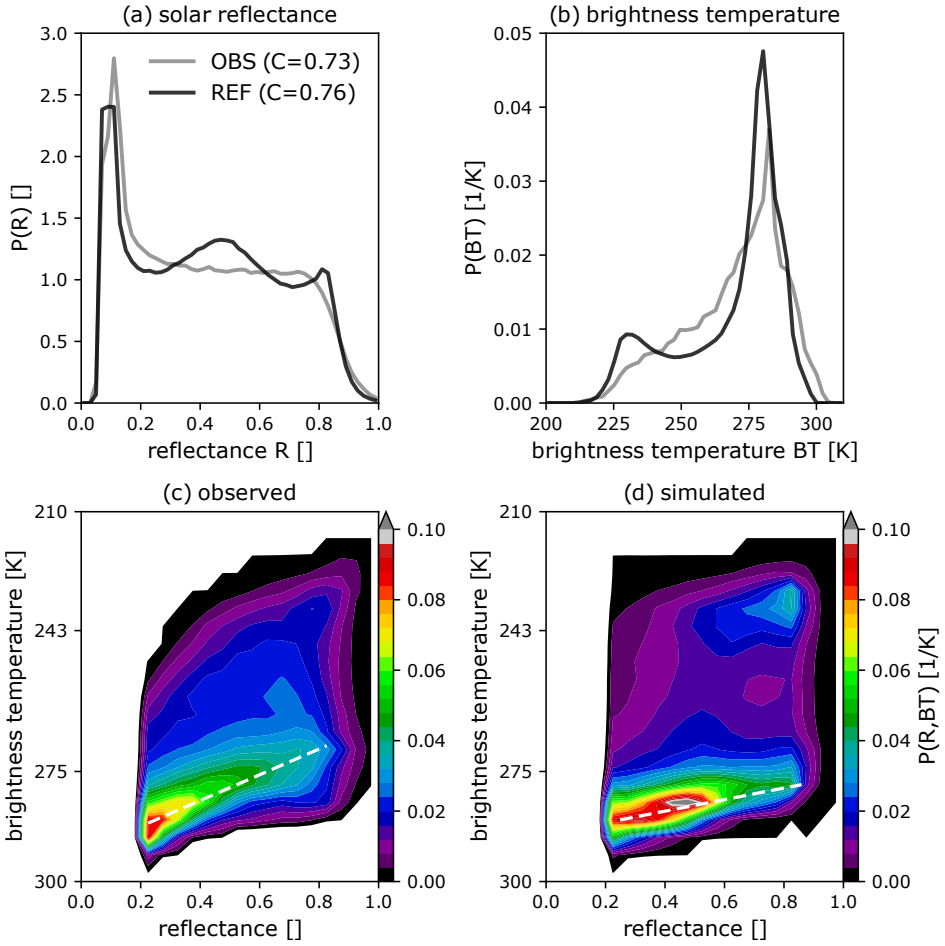

Figure 4.5: *Individual PDFs for 0.6 µm SEVIRI solar reflectance (VIS006) (a), 10.8 µm SEVIRI brightness temperature (IR108) (b) and combined VIS006-IR108 PDF (bottom) of observations (c) and simulations (d) at 12 UTC for the full test period. The numbers in the legend of (a) indicate the cloudiness, i.e. the fraction of pixels exceeding a reflectance of 0.2.*

of the systematic errors evident in the 1d histograms, and very valuable information for model development, showing which model configuration produces more realistic clouds.

4.3 Sensitivity of synthetic VIS006 and IR108 satellite observations

4.3.1 Contributions of different clouds to the reflectance distribution

For understanding the sensitivity of the synthetic visible satellite images to changes in operator settings and model modifications, it is helpful to determine the contribution of different hydrometeor types and subgrid-scale clouds to the reflectance histogram of the reference run (Fig. 4.5a). Figure 4.6 shows the observed and simulated VIS006 solar reflectance distribution (OBS and REF are the same as in Fig. 4.5a), the distribution that results from taking only grid-scale clouds into account (REF-grid) and several distributions obtained by using only certain types or combinations of hydrometeors. By comparing the contribution of a certain cloud type, e.g. REF − REF-grid for the subgrid clouds, to the deviation of REF from OBS, one can infer if tuning (i.e. slightly changing) parameters related to this cloud type in the model or the operator could be helpful to reduce REF − OBS. The shapes of the curves can provide further information on this question. Cloudiness values C are provided for each case in Fig. 4.6 to better quantify the relative importance of different cloud contributions.

Grid-scale clouds only lead to a distribution with a nearly flat plateau between reflectances 0.3 and 0.7, a feature that is also found in the distribution of the observed reflectances. However, the fraction of cloud pixels would decrease from $C = 0.76$ to 0.5 if only grid-scale clouds were present. Adding subgrid clouds results in much bet-

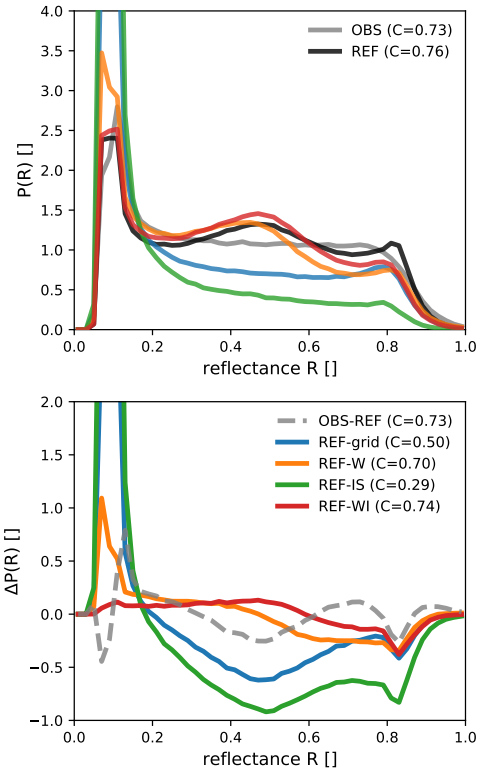

Figure 4.6: *0.6 µm SEVIRI solar reflectance PDFs (top) for the test period computed for the observations (OBS) and the reference experiment (REF). The additional distributions were computed using only the grid-scale clouds (REF-grid), only the water clouds (REF-W) and only the ice clouds (REF-IS) of the reference experiment, respectively. For the red line (REF-WI) water and ice clouds are taken into account. The numbers in the legend indicate the cloudiness. Differences between 0.6 µm SEVIRI solar reflectance PDFs (bottom) obtained for the reference run using the above mentioned model output only and standard settings.*

ter agreement with the observed value of $C = 0.73$. It is thus essential to take these additional subgrid clouds into account. However, the imperfect parameterisation of subgrid clouds also contributes to deviations in the shape of the distribution: While the distributions of the observations and the grid-scale clouds only simulation exhibit a relatively flat plateau, the addition of subgrid clouds leads to a histogram curve with a pronounced maximum at 0.5 and a minimum at 0.7.
When only water clouds are used as input to the operator (REF-W), the cloudiness falls off from $C = 0.76$ to $C = 0.70$. Primarily, reflectances larger than 0.5 become slightly less frequent. In contrast, taking only ice clouds (including snow) into account (REF-IS) has a more substantial impact on the histogram and results in much smaller cloudiness of $C = 0.29$. Water clouds thus play a much more substantial role for the reflectance distribution than ice clouds. This result is not surprising as the ice water path is much smaller than the liquid water path and additionally larger ice particles are less effective in scattering light than smaller water droplets (Fig. 3.3a).

In both the water-only and the ice-only cases, the corresponding subgrid clouds are included. The water-only curve (REF-W) shows the same deviation from the plateau-like shape of the observed distribution as the curve computed for all clouds (REF), but the ice-only curve (REF-IS) does not. Thus, it seems that the subgrid water cloud parameterisation needs to be improved to get better agreement in the histogram shapes. Finally, ignoring the simulated snow content (REF-WI) has a small, but detrimental effect. This emphasizes the need for including snow in the computation of the RT input variables as discussed in section 3.2.1.

4.3.2 Estimated uncertainty of the visible forward operator

Forward operators use fast, approximate RT methods and rely on the limited information that is available from the NWP model. Due to missing 3D RT effects and missing information (e.g. on unresolved cloud properties) their output is to some extent uncertain. While forward operators for thermal infrared channels have been available for some time and their uncertainties have been investigated in several studies (e.g. Senf and Deneke, 2017, Saunders et al., 2017, 2018), no such information is available for visible channels. In the following, the uncertainty related to what we regard as the most critical error sources will be estimated by varying the corresponding operator settings.

The potential sources of uncertainty to be investigated are related to missing 3D RT effects, unknown or inconsistent overlap statistics of subgrid-scale clouds, the spatial and temporal variation of aerosols and the shape of cloud ice particles. To estimate upper limits of the uncertainty in the reflectance distribution related to these sources, we repeated the computation of visible reflectances applying VISOP to the reference simulation with deactivated cloud top inclination (CTI) parameterisation, random instead of random-maximum subgrid cloud overlap, and aerosols or a different kind of ice habit included in the MFASIS LUT. The deviations in the reflectance distribution for the reference run caused by changing these operator settings are shown in Fig. 4.7.

The subgrid cloud overlap assumptions would not be a source of operator uncertainty if the assumptions in the NWP model and the operator were entirely consistent. However, the near-operational version of ICON employed to perform the model runs for this study uses inconsistent overlap assumptions in the infrared and visible part of the spectrum.

This inconsistency will likely be corrected in future versions, but at the moment, it means that the operator cannot be entirely consistent with the model. The deviation in the reflectance distribution caused by changing the assumption from maximum-random to random in the operator (orange line in Fig. 4.7) can be regarded as an upper limit for the impact. Changing the assumption shifts the peak around R=0.5 (which is related to subgrid clouds, as discussed in Sect. 4.3.1) to higher reflectances, but has not much influence on reflectances larger than 0.7.

Missing or imperfectly modelled 3D RT effects are likely the source of uncertainty that is most difficult to quantify. According to Scheck et al. (2018) the most important 3D effect is related to the inclination of the cloud top surface, which influences the observed reflectance. The parts of the cloud top surface tilted towards the sun appear brighter and those tilted away from the sun darker. The cloud top inclination correction (CTI, see Scheck et al., 2018) accounting for this effect has been shown to reduce the error with respect to full 3D RT calculations and is included in the reference run. The main effect of the CTI on the reflectance histogram is to reduce the slope at the high reflectance end of the distribution and to bring it in better agreement with observations. Switching off the CTI leads to a too steep decline of the distribution at high reflectances, which is visible as a double peak structure at $R > 0.8$ in Fig. 4.7. Other 3D RT effects like cloud shadows may also play a role, in particular for larger zenith angles. However, by focusing on observations near local noon, their influence should be minimized.

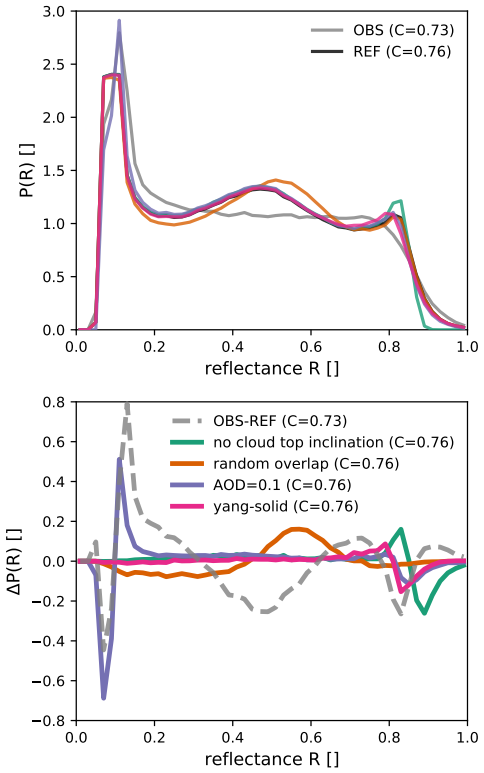

Figure 4.7: *PDFs (top) and differences (bottom) between 0.6 µm SEVIRI solar reflectance PDFs obtained for the reference run with modified operator settings and standard settings. The modified settings are switching off the cloud top inclination, using random instead of maximum-random subgrid cloud overlap, including aerosols with an optical depth of 0.1 and changing the cloud ice particle habit to solid columns. For comparison also the difference between observation and reference run histogram is shown (dashed curve).*

According to retrievals based on measurements at AERONET stations (see Giles et al., 2019) in Germany, the mean AOD in June 2016 was in the range 0.06 to 0.12 at a wavelength of 675 nm, which is similar to the wavelength of the visible channel considered here. To estimate the impact of these aerosols on the reflectance histogram, an MFASIS LUT was computed that includes aerosols (the "continental clean" aerosol mixture available in libRadtran, see Emde et al. 2016) with an optical depth of 0.1. Including aerosols in the MFASIS LUT, i.e. taking direct aerosols effect into account, influences the reflectance histogram in two ways. In clear-sky conditions, the reflectance increases

because aerosols scatter photons to the satellite, whereas in cloudy conditions, aerosols scatter photons out of their path towards the satellite. In the presence of aerosols the high reflectance end of the distribution is thus shifted towards lower reflectances and the low reflectance end towards higher reflectances. Shifting the pronounced ground peak in the distribution causes a double peak structure at low reflectances in Fig. 4.7, whereas shifting the flat high reflectance end only causes a single negative peak. In general, the error introduced by direct aerosol effects for events like (Saharan) dust outbreaks can be higher, and could potentially lead to significant errors in solar reflectances. Days affected by such events, which did not occur during our test period, should thus be excluded from model evaluation studies.

Finally, the shape of cloud ice particles is also an uncertain factor that influences the reflectances distribution. Changing the shapes quite strongly from the `baum_v36` general habit mixture (Baum et al., 2014) to solid columns (using the optical properties by Yang et al. 2005) basically only affects the highest reflectances, which are slightly reduced. The ice habit is thus not likely to cause large uncertainties in the reflectance distribution for our test period, which is characterized by a high low-level cloud cover and overlaying semi-transparent cirrus clouds. For periods with more and thicker ice clouds the uncertainties could be higher.

4.3.3 Sensitivity to model settings

Figure 4.8 shows the deviations of the reflectance and BT distributions computed for model runs using modified settings (see Sect. 3.1) with respect to the reference run. In general, these deviations are of similar magnitude as the systematic deviations between the observations and the model equivalents for the reference run discussed in section 4.2.2 (see dashed curve in Fig. 4.8). In section 4.2.2, we identified several reasons for systematic deviations between the simulations and observations: An underestimation of thick clouds (R in [0.6,0.8]), a too low boundary layer height, too many high clouds and an insufficient representation of low-level water clouds. As further analysed in Sect. 4.3.1, we found that the discrepancy in low-level clouds mainly arises from subgrid water clouds (R in [0.3,0.6]).

Figure 4.8a shows the effect of model modifications on the reflectance distribution. The first modification (experiment II), reducing the effective radii by increasing the updraft velocity and thus also the number of cloud condensation nuclei, leads to more thick clouds with $R > 0.7$ and less thin clouds with $R < 0.5$. Changing the subgrid cloud parameters (experiment III) or reinforcing shallow convection (experiment IV) has a qualitatively similar but much stronger impact on the reflectance distribution. Pixels with dense clouds become more numerous and the number of pixels with thin to medium clouds is reduced. These changes are larger than the deviations of the reference run (experiment I) from the observation (dashed line in Fig. 4.8a). In case of the modified shallow convection, the cloudiness increases from 0.76 to 0.8, which means that the deviation from the observed value of 0.73 is considerably larger.

Switching to the double-moment microphysics scheme (experiment V) mainly moves pixels with very high reflectances ($R > 0.8$) to somewhat lower reflectance values between 0.6 and 0.8 and increases the cloudiness slightly. Thin to intermediate clouds ($0.2 < R < 0.6$) are only weakly affected. Still using the two-moment scheme but turning off subgrid-scale ice clouds (experiment VI) slightly decreases the cloudiness but basically leads to the

same distribution as experiment V. Hence, ice subgrid-scale clouds cannot be responsible for the surplus of pixels with solar reflectances around $R = 0.5$ that was attributed to subgrid clouds in Sect. 4.3.1. Finally, reducing the subgrid-scale water clouds experiment VII) in addition leads to much larger changes, with negative peaks around $R = 0.5$ and $R = 0.8$ and

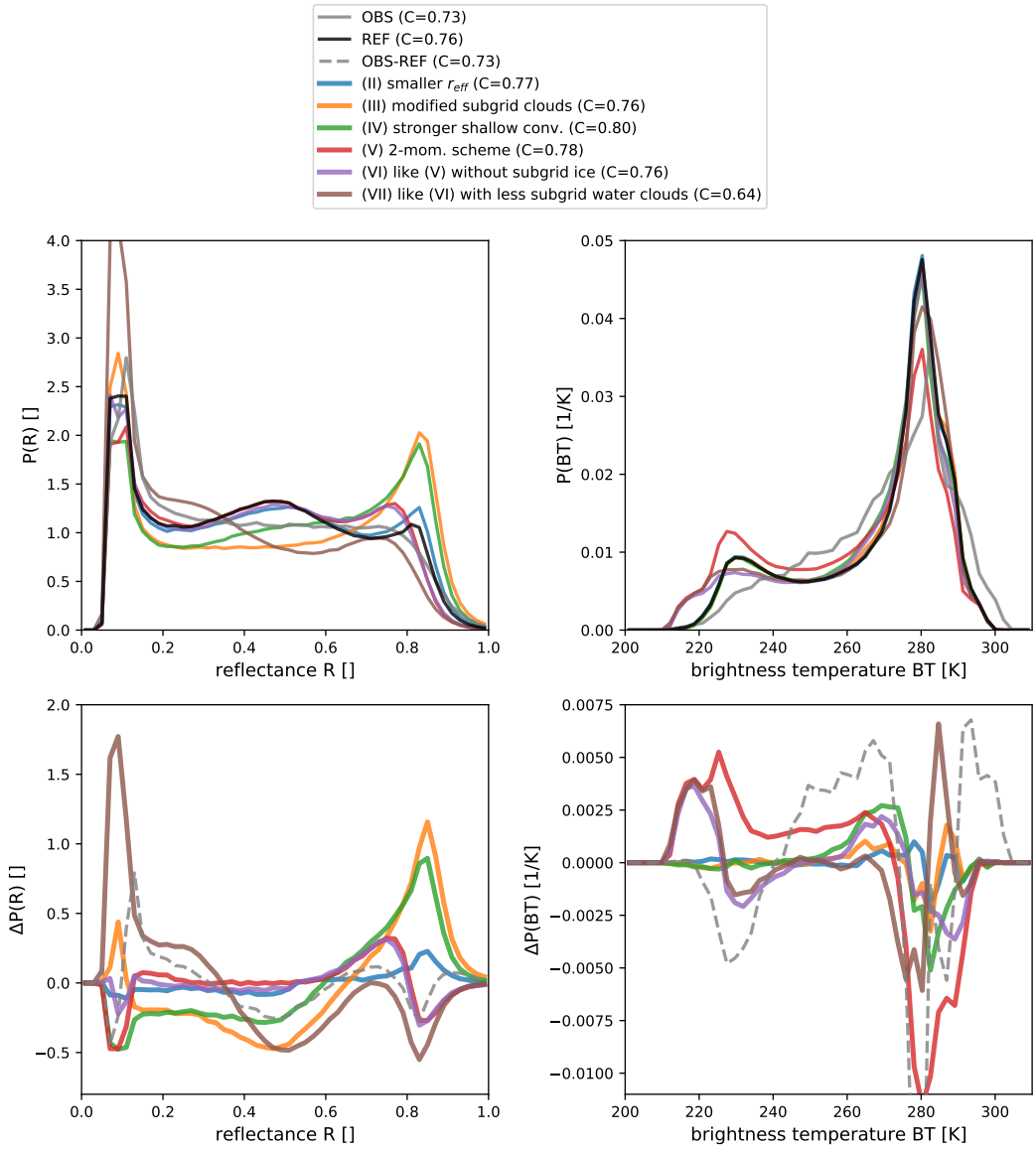

Figure 4.8: *PDFs (top) in 0.6 µm SEVIRI solar reflectance (left) and 10.8 µm SEVIRI brightness temperature (right) and differences (bottom) in solar reflectance and brightness temperature PDFs between perturbed model simulations and the reference run. The perturbed model settings are (II) increased cloud droplet number concentration (smaller effective radius) by increasing the updraft velocity at activation, (III) modified distribution of turbulent subgrid liquid clouds (less and thicker subgrid clouds), (IV) stronger shallow-convection parameterisation by doubling the thickness of the thickest unresolved cloud, (V) simulation with the two-moment scheme, (VI) like (V) without subgrid-ice clouds and (VII) like (VI) and reduced number of subgrid-scale liquid clouds. For comparison also the difference between observation and reference run histogram is shown (dashed curve).*

positive values for $R < 0.35$. These changes point into the right direction to mitigate the deviations of the reference run (dashed line in Fig. 4.8a). However, here the modification is too strong as cloudiness is dramatically underpredicted in this case ($C = 0.64$). Compared to visible reflectances, the changes in the BT distribution introduced by modified model settings are more difficult to interpret because the signal depends on cloud optical depth as well as on cloud top height. The modifications in experiments II and III only affect water clouds and thus only lead to changes at higher BTs. These changes are relatively small compared to those required to correct the deviations of the reference run (dashed line). Making shallow convection stronger (experiment IV) has a stronger impact and increases the number of pixels with BT between 250K and 275K at the expense of those with higher values. Switching to the double-moment scheme (experiment V) increases the number of middle to very high clouds for BT<270 K, and introduces a substantial reduction of the clear-sky and low-level cloud signal (BT around 280 K). These changes indicate that the two-moment scheme generates even more dense ice clouds than the one-moment scheme in the reference run, which already predicts too many of these clouds. These high clouds obscure lower clouds and the surface, which leads to less pixels with high BTs. Switching off subgrid ice clouds in the two-moment simulation (experiment VI) reveals that the peak around BT = 220 K is related to grid-scale clouds in the double-moment scheme, and the distribution of middle clouds is more like the single-moment simulation. Additionally modifying the subgrid liquid water clouds (experiment VII) again mainly affects the clear-sky and lower-level cloud signal.

Comparing the changes in the reflectance and BT distribution that were introduced by modified model settings within their estimated uncertainty leads to the following interpretation: The reflectance distribution is mainly affected by changes to water clouds and is only weakly influenced by changes to ice clouds. In contrast, the BT distribution is most strongly affected by changes in the ice clouds, but modified water clouds also have some influence on higher BTs. The distinct changes in the distributions caused by the individual model modifications allow to assess which modification could be useful to mitigate deviations from the observed distributions. The results shown in Fig. 4.8a indicate that a modified version of experiment VII with weaker modifications or a combination of II, III and IV could be able to achieve the corrections required for the reference run, i.e. to reproduce the dashed line (OBS-REF). In both cases the subgrid water clouds play an important role. To correct systematic errors in the reflectance distributions it therefore seems particularly important to tune or advance the subgrid cloud scheme. While the reflectance distribution is not sensitive to changes in subgrid ice clouds, these are clearly important for the BT distribution (compare experiments V and VI in Fig. 4.8a,b). The combined information from the two parts of the spectrum can thus provide guidance on optimizing the subgrid cloud scheme.

In contrast to visible reflectances, there is no obvious way to scale or combine the model modifications in order to eliminate the errors of the reference run in the IR108 channel, i.e. to reproduce the dashed line in Fig. 4.8b. Additional or different model modifications appear to be required for this purpose, but the results presented here already indicate that particular modifications leading to less grid-scale ice clouds are required.

The discussed changes described with 1D distribution become more vivid in 2D PDF difference plots (Fig. 4.9), combining the two complementary satellite channels. Interest-

ingly, changing the subgrid-scale water clouds (SIM III) also affects relatively high clouds (likely mixed-phase), not obvious in the 1D PDF of IR brightness temperature. Switching to the two-moment scheme much more high ice clouds are observable, because the two-moment produces twice as much ice than the one-moment scheme (Fig. 3.4). Reducing the subgrid-scale ice clouds (compare SIM V and VI) reduces the probability of high ice and

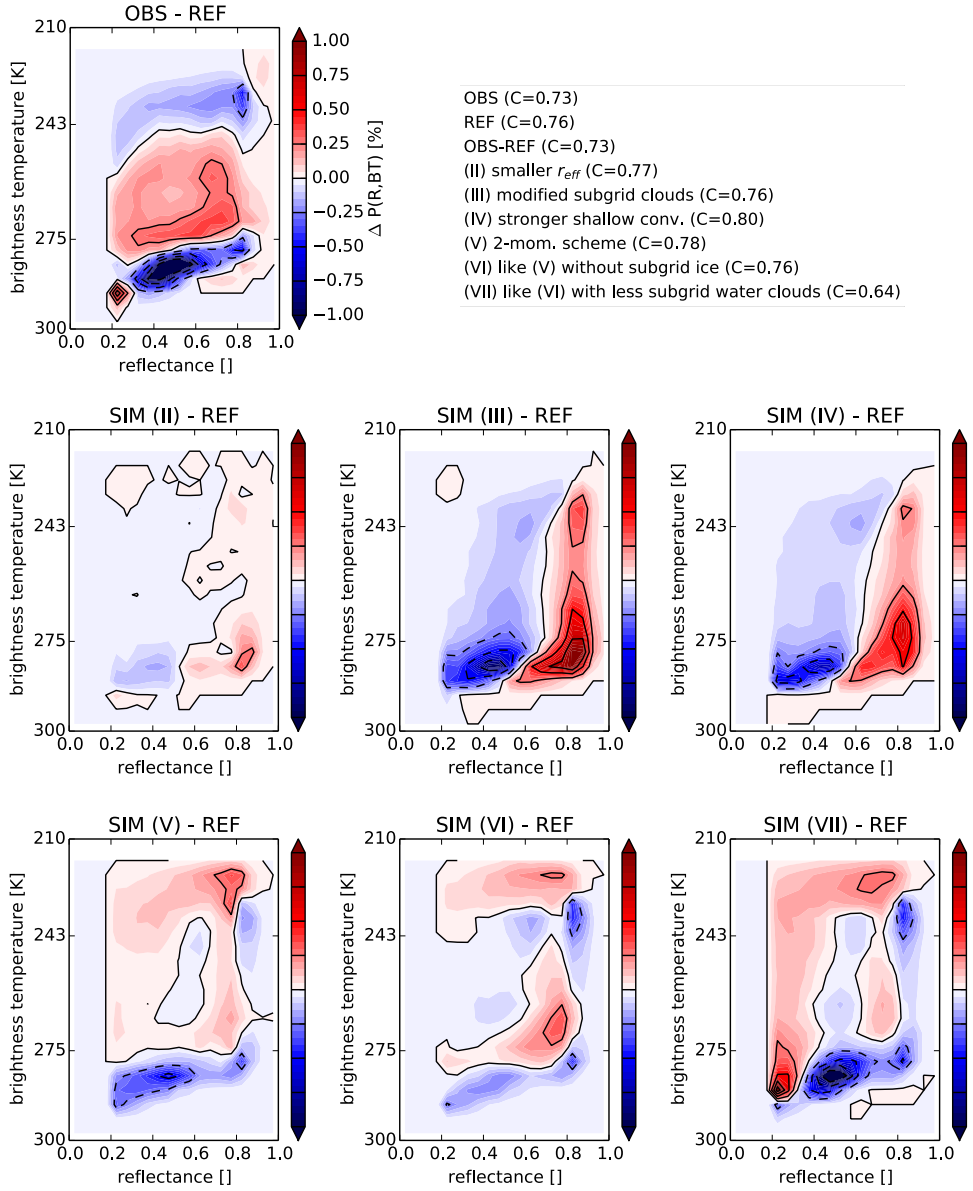

Figure 4.9: *Differences between perturbed model simulations and the reference run in 2D PDFs of 0.6 µm SEVIRI solar reflectance and 10.8 µm SEVIRI brightness temperature for model settings. The perturbed model settings are (II) increased cloud droplet number concentration (smaller effective radius) by increasing the updraft velocity at activation, (III) modified distribution of turbulent subgrid liquid clouds (less and thicker subgrid clouds), (IV) stronger shallow-convection parameterisation by doubling the thickness of the thickest unresolved cloud, (V) simulation with the two-moment scheme, (VI) like (V) without subgrid-ice clouds and (VII) like (VI) and reduced number of subgrid-scale liquid clouds. For comparison also the difference in 2D PDF between observation and is shown.*

middle clouds, while low clouds' probability is enhanced. Therefore, by reducing subgrid-scale ice clouds, the sensor looks deeper into the atmosphere. A not negligible part of the medium-high clouds in the observation could be a signal of high ice clouds, for which the signal is not yet saturated (see Fig. 3.3).

It should be noted that the results presented in this study were obtained for a summer period, in which the reflectance was clearly dominated by water clouds. For situations in which ice clouds play a more important role, the visible channel should still provide better information on the total (liquid and frozen) water content than the infrared channel. However, it could be more problematic to attribute systematic deviations in the reflectance histograms to water or ice clouds and the error related to assumptions on the ice habit may be larger. Using in addition the 1.6.μm channel, which allows for distinguishing water from ice clouds, may be helpful in these cases.

4.3.4 Sensitivity intercomparison for solar reflectances

The comparison of Fig. 4.7 and Fig. 4.8a already indicates a considerably larger effect of model modifications compared to that of operator uncertainties on the reflectance distribution for the full test period. To provide a clearer comparison of the impact of model modifications and operator uncertainties, we computed the individual changes on each day

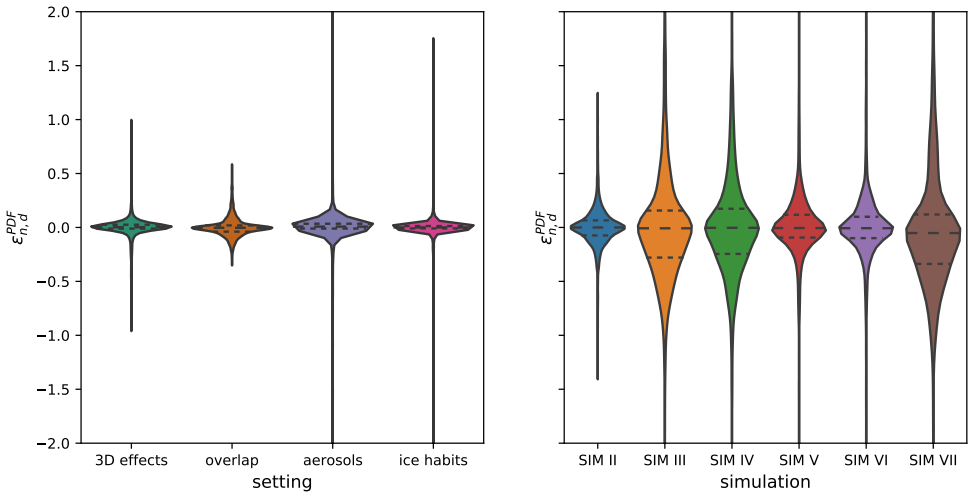

Figure 4.10: *Distributions of daily bin-by-bin differences from reference run in 0.6 μm SEVIRI solar reflectance as a measure of uncertainty in the visible forward operator (left) and the model (right). The modified forward operator settings are switching off the cloud top inclination (3D effects), using random instead of maximum-random subgrid cloud overlap (overlap), including aerosols with an optical depth of 0.1 (aerosols) and changing the cloud ice particle habit to solid columns (ice habits). The perturbed model settings are (II) increased cloud droplet number concentration (smaller effective radius) by increasing the updraft velocity at activation, (III) modified distribution of turbulent subgrid liquid clouds (less and thicker subgrid clouds), (IV) stronger shallow-convection parameterisation by doubling the thickness of the thickest unresolved cloud, (V) simulation with the two-moment scheme, (VI) like (V) without subgrid-ice clouds and (VII) like (VI) and reduced number of subgrid-scale liquid clouds. Horizontal dashed lines indicates 25^{th}, 50^{th} (median), and 75^{th} percentile.*

of the test period in all of the reflectance bins (see Sect.3.3). The violin plots in Fig. 4.10 show these daily bin-by-bin deviations of the reflectance distribution caused by changes in the operator settings and model modifications. Figure 4.10 indicates that also for individual days of the test period the changes due to model modifications are much larger than the ones related to operator uncertainty. The median deviation and the interquartile range (difference of 75th and 25th percentile) are about one order of magnitude larger for the model uncertainty. As already mentioned, aerosols will have a much stronger impact during e.g. dust events, but such events should not be included in test periods for the evaluation of model clouds.

In general, the operator uncertainties are thus a second-order effect compared to model modifications. Visible satellite images are therefore well-suited to detect and overcome model deficiencies and to provide guidance for model tuning. Still, some of the deviations of the model reflectance distribution could be related to deficiencies of the operator. An improved cloud top inclination or changes in the cloud ice optical properties could mitigate some of the deviations at high reflectances and using the correct aerosol optical depth can particularly improve the low-reflectance end of the distribution (see Fig. 4.7). However, for a broad range of reflectances between 0.2 and 0.8 it is only the inconsistency in the overlap assumption that makes the operator results uncertain. As discussed above, this is actually only a temporary issue related to the current versions of the ICON model. As soon as the overlap assumptions in the the model are consistent, the correct choice of the overlap assumption can be regarded as a model setting and model evaluation using visible reflectances can provide information on suitable choices.

4.4 Summary

In this chapter, visible and infrared satellite observations are used to better understand the model representation of clouds. Semi-free 30-day convection-permitting hindcast simulations are conducted that are only driven by analysis boundary conditions. In this setup, clouds freely develop inside the domain without any perturbations from data assimilation.

The evaluation of visible and infrared satellite observations individually reveals systematic deviations in the model representation of clouds. From the perspective of the visible satellite channel, the model exhibits shortcomings in representing medium-thick to thick clouds, independently of the used microphysics scheme. This deviation can be attributed to subgrid-scale water clouds, as sensitivity tests of solar reflectance to different hydrometeors and subgrid-scale clouds demonstrate. Overall, liquid water clouds contribute most to solar reflectance. Visible satellite observations can therefore be utilised to constrain the model's (subgrid-scale) water cloud assumptions. In the infrared, the comparison indicates that the model generates too many high ice clouds and underestimates mid-level clouds.

Combining the two complementary observation types, solar reflectance and infrared brightness temperature, reveal an overall similar structure in the 2D distribution of the simulated and observed clouds. However, additional information on the nature of systematic deviations in the model representation of clouds become apparent in these joint 2D distributions. This approach synthesises individual deviations in visible and infrared satellite observations and points to inherent model shortcomings. Inherent model shortcomings are related to the representation of boundary layer (sub-grid) water clouds, shallow and

deep convection and an excessive production of ice clouds.

Simulations with perturbed cloud-related parameterisation reveal sensitivities of synthetic satellite observations. The perturbed cloud-related parameterisations are uncertain and modified within their physical plausibility. Changes in the distribution of solar reflectance are mainly related to water clouds assumptions, while changes in the infrared brightness temperature distribution are mainly related to ice clouds assumptions. Hence, both satellite channels can provide crucial information to constrain uncertain model parameters. In order to improve the model representation of clouds, the subgrid-scale water cloud and cloud-ice scheme require modifications.

Furthermore, uncertainties of the visible forward operator are smaller than the present systematic deviations. Therefore, the visible operator can not cause severe systematic deviations. The examined uncertainties in VISOP are related to 3D RT effects, aerosols and ice habits. Cloud top inclination mainly improves the decline of the distribution for high solar reflectances. Additionally, including aerosols can improve the clear-sky peak and dampens relatively high solar reflectances. Hence, considering cloud top inclination and aerosols improves solar reflectance distribution. Assuming solid ice habits instead of a habit mixture affects mainly high solar reflectances. However, the uncertainty from ice habits plays only a secondary role for the test period.

Finally, the comparison on a daily basis of model and operator uncertainty proves that the visible forward operator is accurate enough for evaluation and assimilation. Moreover, the forward operator approach helps understand the model representation of clouds and points to inherent model shortcomings, particularly by combining two complementary satellite observations. Hence, this novel approach should be utilised to constrain uncertain model parameters.

Chapter 5

Assimilation of visible satellite observations

The previous chapter showed that the visible forward operator is accurate enough for model cloud evaluation and assimilation. This chapter demonstrates the potential of assimilating visible satellite channels for convective-scale numerical weather prediction. Two different simulations for a 1-month period are compared. The simulation CONV resembles the pre-operational setup of DWD (in 2020), using only conventional observations to compute the analysis. VISCONV additionally assimilates visible satellite observations to represent cloud distribution in the analysis. The impact in the analysis and short-term forecasts in solar reflectance and cloud distribution by assimilating reflectances is shown. Afterwards, the simulations of both setups are evaluated against conventional observations. Subsequently, the influence on 24-h forecasts and the error dependency between solar reflectance and global horizontal irradiance is presented.

5.1 Investigation period

According to DWD's Forecasting and consulting centre (after Hess and Brezowsky (1969)), the first third of the period (July 1 - 08) was dominated by westerly and northwesterly flow. Behind a cold front moving to the northeast of Europe, relatively humid and warm sea air was advected to Central Europe. This resulted in locally heavy thunderstorms with precipitation and hail. Individual fronts moved towards the Alps due to a surface low over the Balkans and a high over Ireland. Subsequently (July 09 - 17), a strong high-pressure system formed over the Norwegian Sea, which led to a northerly flow over Germany. As a result, relatively cool air was advected to Germany, leading to rain, especially in the north and east of Germany. From July 18 onwards, a more westerly flow was established again, with locally triggered convection and some frontal passages. Warm air masses were advected and a strong upper-level high-pressure system built up over central Europe, strengthening in the following days. A low-level high also builds upon. As a result, Western and Central Europe was hit by an extreme heatwave (July 20-26; (De Villiers, 2020)), with record temperatures in Germany. Overall, the period was characterised by different weather conditions, with some sunny days, locally triggered convection, partially heavy precipitation and frontal passages.

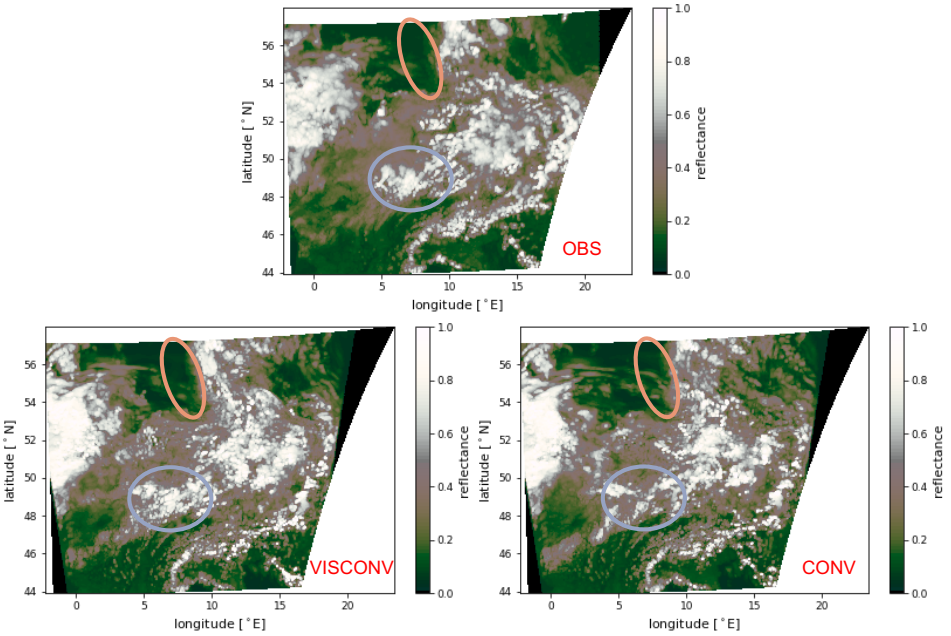

Figure 5.1: *0.6 µm MSG SEVIRI solar reflectance observation on 19 July 2019 12 UTC (top) and VISCONV (bottom left) and CONV (bottom right) first guess. (EUMETSAT)*

5.2 Analysis and short-term forecast impact

5.2.1 Solar reflectance error evolution during cycling

This section demonstrates an overall beneficial impact in the analysis and the first guess by the reflectance assimilation. Figure 5.1 shows the observed and simulated satellite images of the two setups on 19 July 2019, 12 UTC. In this example, a pronounced convective cloud over France (blue circle) is also clearly detectable in the VISCONV 1-h short-term forecast. In contrast, the CONV setup underestimates the thickness of this cloud. Furthermore, the assimilation of solar reflectance reduces false alarm errors in the first guess, improving the overall cloud cover (orange circle: North Sea).

Figure 5.2 shows the period mean error evolution in solar reflectance during cycling. The reflectance MAE in the VISCONV analysis is strongly reduced at each analysis time step compared to the 1-h forecast. This indi-

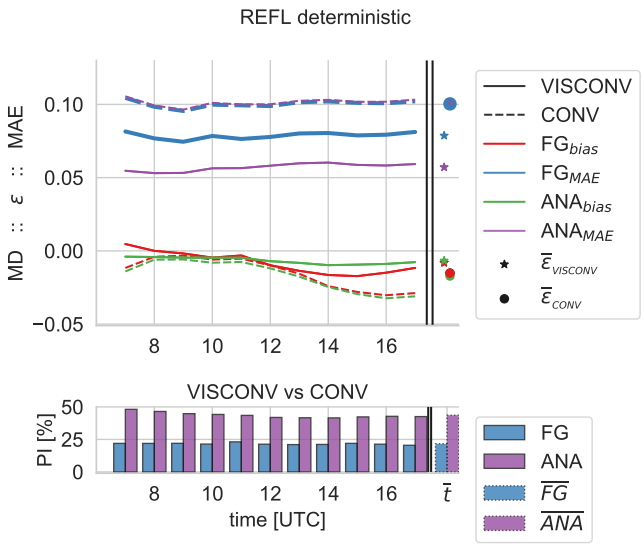

Figure 5.2: *Domain and period mean 0.6 µm MSG SEVIRI solar reflectance error evolution during data assimilation (top panel) and the percentage improvement in the VISCONV vs the CONV first guess and analyses (bottom panel) in July 2019.*

cates a better representation in cloud distribution and thickness initially. In contrast, using only conventional observations to compute the analysis is unable to reduce reflectance errors. Accordingly, the average VISCONV solar reflectance analysis error is only half, compared to CONV.

The average percentage improvement (PI) is still 25 % in short-term forecasts and comparable to Scheck et al.'s (2020) findings for a synoptically and locally-driven convective day case study. In both simulations, the mean differences (MD) in solar reflectances are negative but closer to zero in VISCONV than in CONV, particularly during noon. This implies more cloudy pixels or thicker clouds in VISCONV. Moreover, during the whole period, reflectance assimilation reduces errors in the analysis and the short-term forecasts at each data assimilation time step. Hence, a beneficial impact is always apparent, independently of the weather condition. Overall, the assimilation of reflectance substantially reduces solar reflectance errors initially and in the short-term forecasts.

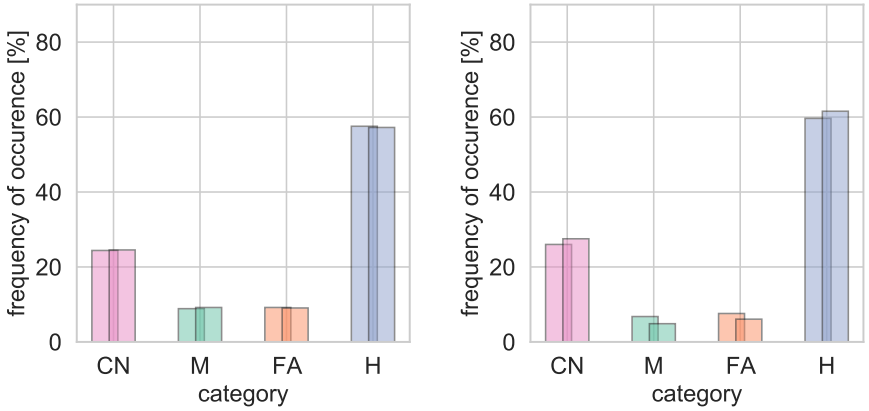

(a) CONV **(b)** VISCONV

Figure 5.3: *Frequency of occurrence in correctly negative CN, hits H, miss M and false alarm FA category in CONV (a) and VISCONV (b). The left bar corresponds to the first guess and the right bar to the analysis, respectively.*

5.2.2 Solar reflection distribution

The solar reflectance error and the reduction discussed above can be caused by incorrect cloud thickness or by clouds at the wrong location. Four categories were defined in Sect. 3.3 to investigate the error source in solar reflectance and to reveal the dominant process in error reduction. The following categories are computed for the first guess and analysis, respectively.

CN: correctly negative , where the observed and simulated pixel is clear-sky

H: hit, where the observed and simulated pixel is cloudy

M: miss, where a cloud is observed but not simulated

FA: false alarm, where a cloud is simulated but not observed

Figure 5.3 shows the time-averaged frequency in each category. The frequency of occurrence in each category is relatively comparable in the two setups. Nevertheless, the cloud distribution in VISCONV is in better agreement with the observations, as H and CN appear more frequent, while the number of M and FA is reduced. Moreover, in each analysis time step, the cloud distribution is further improved in VISCONV because the number of correctly negative and hits increases, while M and FA decrease. In CONV, nearly no modification occurs between first guess and analysis.

These findings are also apparent in reflectance PDFs (Fig. 5.4). In CONV, the shape of the reflectance distributions is almost identical in the first guess and the analyses. Additionally, if only cloudy pixels are considered (H, FA, M), the distributions show more deviations in the representation of semi-transparent to medium-thick clouds. The reflectance assimilation improves the agreement in cloud distributions, with quasi no displaced and thicker clouds in short-term forecasts (FA, M). Additionally, the shape of the simulated and observed reflectance distribution of cloudy pixels is in better agreement. Both setups reveal deviations for high solar reflectance values. This deviation is related to the simplified visible forward operator version used for data assimilation. A sensitivity experiment that compares a 1D and 3D forward operator is discussed in Sect. 5.5.

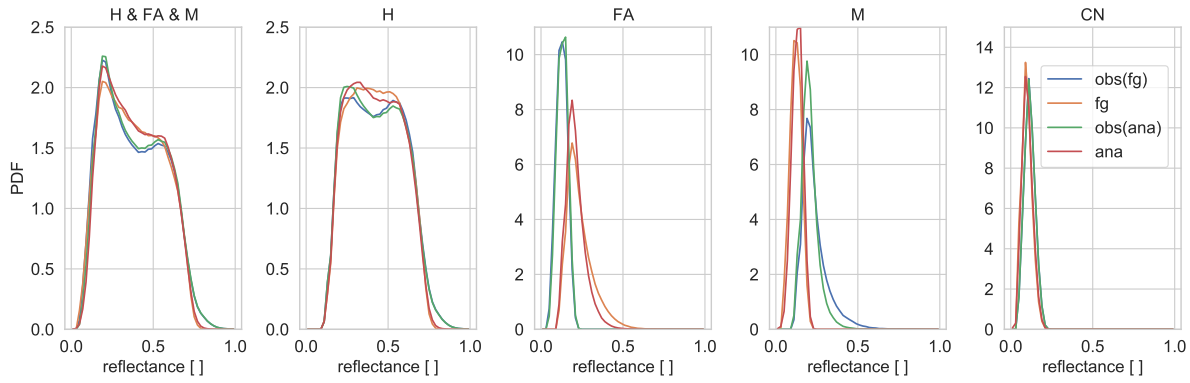

(a) VISCONV PDF

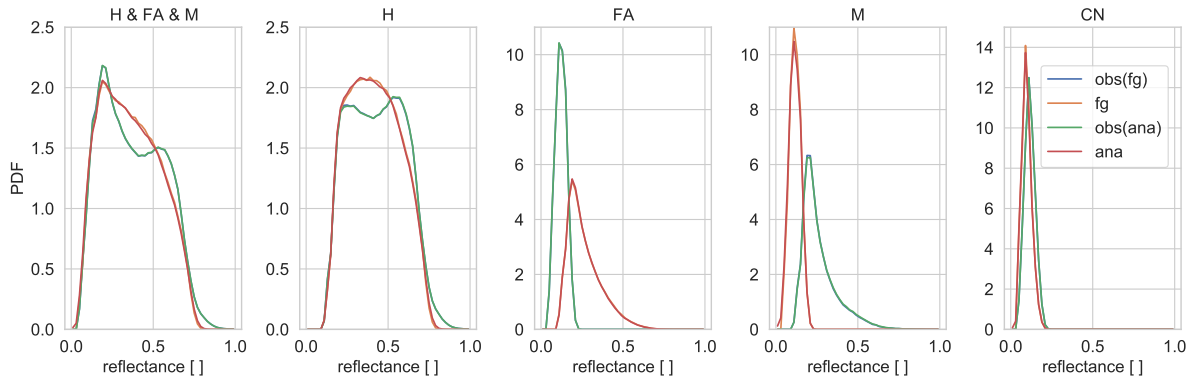

(b) CONV PDF

Figure 5.4: *Observed and simulated 0.6 µm MSG SEVIRI solar reflectance PDF in VISCONV (top) and CONV (bottom) first guess fg and analysis ana. The PDFs are individually computed for hits H, false alarm FA, miss M and correctly negative CN satellite pixels in July 2019.*

Figure 5.5 shows the average share of each category to the average solar reflectance MAE (same as average MAE in Fig. 5.2). This plot reveals that the dominant error source is deviations in cloud thickness (H) in both setups, while errors from M and FA are comparably low. The error introduced by clear-sky reflectance is almost negligible, meaning a realistic representation of the clear-sky reflectance. Therefore, the dominant error reduction when the solar reflectance is assimilated is improving cloud thickness (76 %), followed by reducing miss (15 %) and false alarm errors (9 %).

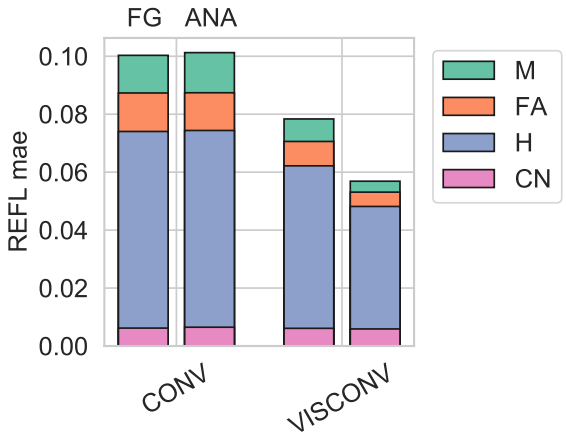

Figure 5.5: *Contribution of each category to average mean absolute error. The left (right) bar corresponds to the first guess (analysis) of CONV and VISCONV.*

Data assimilation methods usually assume Gaussian error statistics (e.g. Lorenc and Hammon (1988)) for both the observations and the first-guess errors. However, the occurrence of clouds can lead to non-Gaussian first guess departure statistics that pose a severe challenge for the effective assimilation of cloud-affected satellite observations. Additionally, solar reflectance exhibit a non-linear dependency in the presence of clouds and hence, the forward operator is non-linear (Fig. 3.3).

Fig. 5.6 shows the first guess and the analysis departures. The corresponding mean differences and standard deviations are provided in Table 5.1. The departures in each individual category are clearly non-Gaussian distributed. However, if we consider hits, false alarm and miss altogether, the PDF of the first guess departure is similar to a Gaussian distribution in VISCONV. Hence, excluding clear-sky pixels should have an additional beneficial impact in computing the analysis.

Table 5.1: *Summary of mean differences (MD) and standard deviations (STD) of first guess (FG) and analysis (ANA) departures of the two experiments VISCONV and CONV and for the different categories: hits (H), false alarm (FA), miss (M) and correctly negative (CN).*

EXP	x 10^{-2}	Category									
		H & FA & M		H		FA		M		CN	
		MD	STD	MD	STD	MD	STD	MD	STD	MD	STD
VISCONV	FG	-0.44	13	-0.65	12	11	7.8	-11	8.1	-1.6	2.4
	ANA	-0.33	9.1	-0.58	9.1	8.1	5.4	-7.7	4.9	-1.4	2.3
CONV	FG	-1.3	16	17	15	14	10	-15	11	-1.8	2.5
	ANA	-1.5	16	18	15	14	10	-15	11	-1.9	2.6

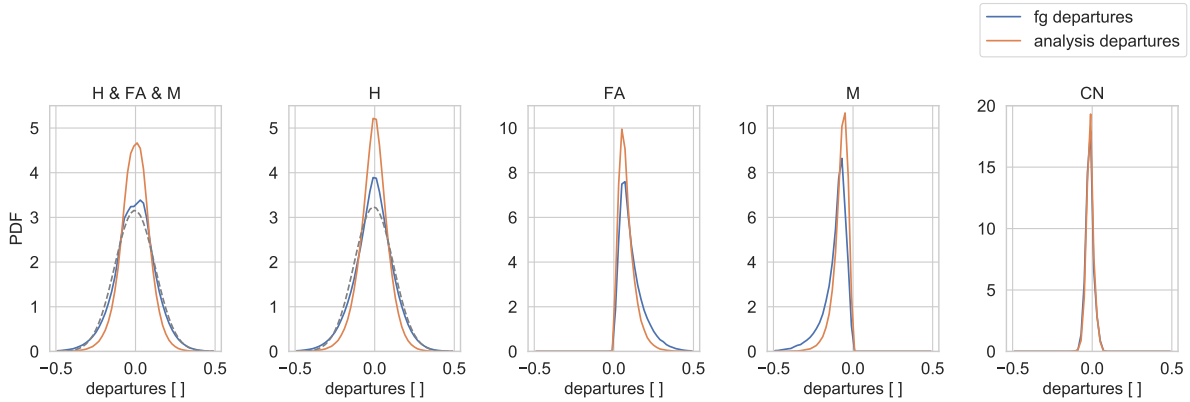

(a) VISCONV departures

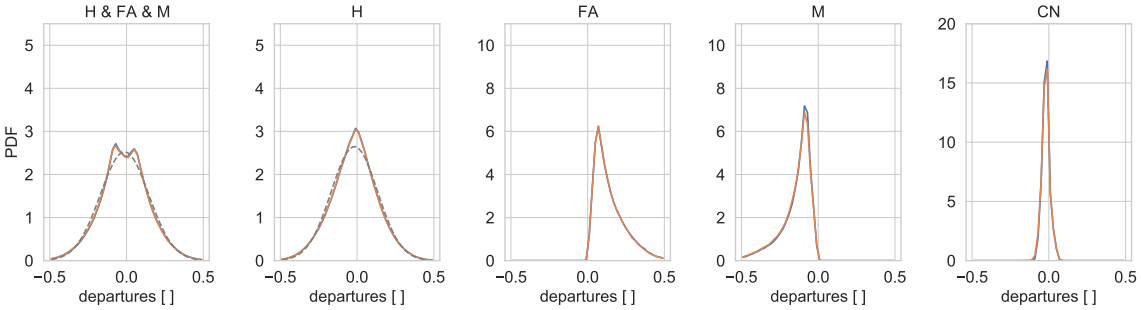

(b) CONV departures

Figure 5.6: *0.6 µm MSG SEVIRI solar reflectance first guess and analysis departures. The grey dashed line represents a normal Gaussian PDF $\mathcal{N}(MD_{fg}; STD_{fg})$. Corresponding MD and STD are in table 5.1*

5.2.3 Evaluation using conventional observations

Figure 5.7a displays the impact on temperature, wind, relative humidity and surface pressure, evaluated against conventional observations. In CONV, only conventional observations are used to compute the analysis and have more weight compared to the VISCONV setup. This makes the CONV analysis more confident towards conventional observations. Overall, the errors in the shown variables are lower than estimated observation errors for a period in June 2011, using Derozies's method (Schraff et al., 2016). Furthermore, corresponding error differences between the two setups are comparatively low in temperature (<0.03 K), surface pressure (< 1Pa), humidity (<0.5 %), and wind (<0.05 m/s). The PI in the RMSE of wind, surface pressure, and TEMP relative humidity and temperature is negative, while the SYNOP temperature and relative humidity representation benefits. In short-term forecasts, the detrimental impact on wind variables is reduced but still present. The PI in other observations is relatively neutral to slightly positive after one hour of model integration.

As shown in Fig. 5.7b, the mean differences are comparable in both setups, but reflectance assimilation clearly impacts surface variables. Next, temperature and humidity at 2m height and the surface pressure are discussed because the first two quantities are in-

dependent metrics (not assimilated). Surface pressure (tendency) indicates if the analysis is consistent with model dynamics (e.g. Lange and Craig, 2014).

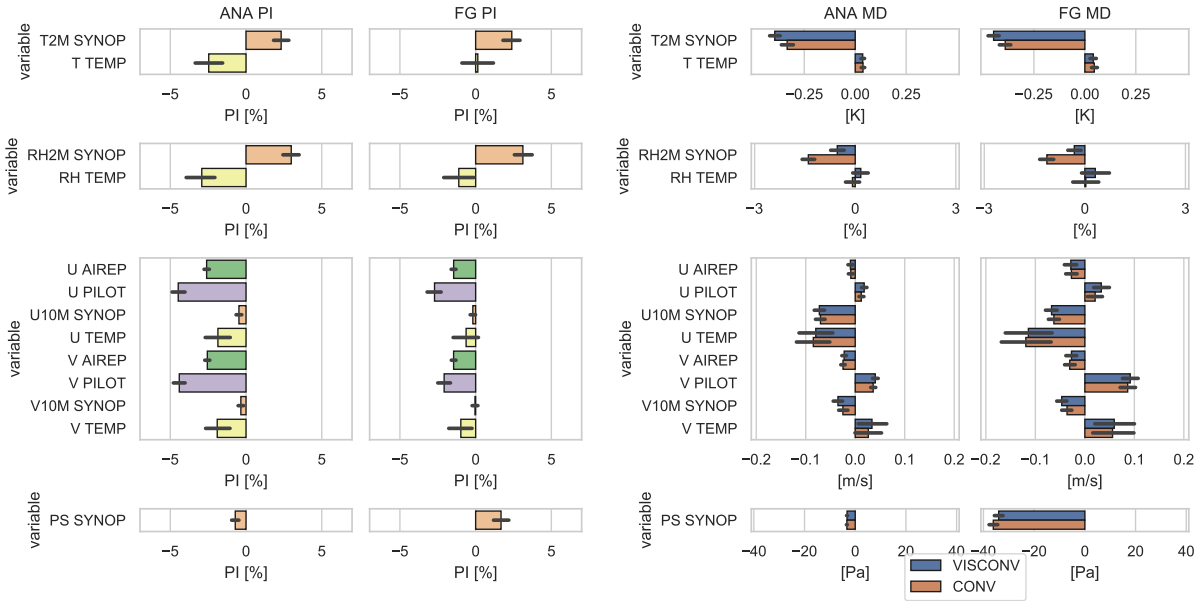

(a) Percentage improvement **(b)** Mean differences

Figure 5.7: *Domain and period averaged percentage improvement in root mean squared error (left) and mean differences (right) evaluated with conventional observations: AIREP, PILOT, SYNOP and TEMP for all assimilation times t=[0,23] UTC.*

Further discussion: surface variables

Clouds strongly interact with solar radiation. Clouds determine heating rates on the earth's surface, whereas heating rates influence cloud formation and evolution. Moreover, clouds cast shadows on the ground and might reduce convection locally through cooling (Jakub and Mayer, 2015), while the atmosphere becomes more balanced vertically, affecting the surface pressure field. Additionally, small variations in moisture or temperature in the boundary layer are critical to whether storms form or not. Such small variations are hardly observable and even more complex to assimilate as small fluctuations are short living. A positive impact from solar reflectance assimilation on these variables should be valuable in predicting subsequent convection.

Temperature and humidity are discussed together as they are linked via the Clausius–Clapeyron relation. In the conventional setup, the simulations are too cold and dry compared to the observations (Fig. 5.7b), implying a general model shortcoming. The mean differences are more negative (positive) in VISCONV than in CONV for temperature (humidity). On average, solar reflectance is higher in VISCONV analysis and first guess and hence, global horizontal irradiance at the surface should be more attenuated. Therefore, the heating rates at the surface are lower, leading to a lower temperature and higher relative humidity at 2m height on average. This link between T and RH is also apparent in their diurnal cycles that show an antisymmetric evolution. At almost all cycling times, the mean absolute errors in the first guess and the analysis of T_{2m} and RH_{2m}

are lower in VISCONV than in CONV, as the cloud distribution is in better agreement to observations. Hence, a clear benefit in T_{2m} and RH_{2m} distribution is apparent, indicating that longer-lasting forecasts, particularly quantities related to convection, might benefit from solar reflectance assimilation.

The model underestimates surface pressure on average. Furthermore, in short-term forecasts, the mean pressure decreases relatively fast (≈-0.4 hPa/h). According to DWD (2021b), this drift was mainly caused by a bias between ICON-EU (BC) and the used ICON-D2 forecasts (meanwhile, DWD applies an adaptive pressure bias correction). Since this pressure drift affects both simulations, a comparison should still be fair.

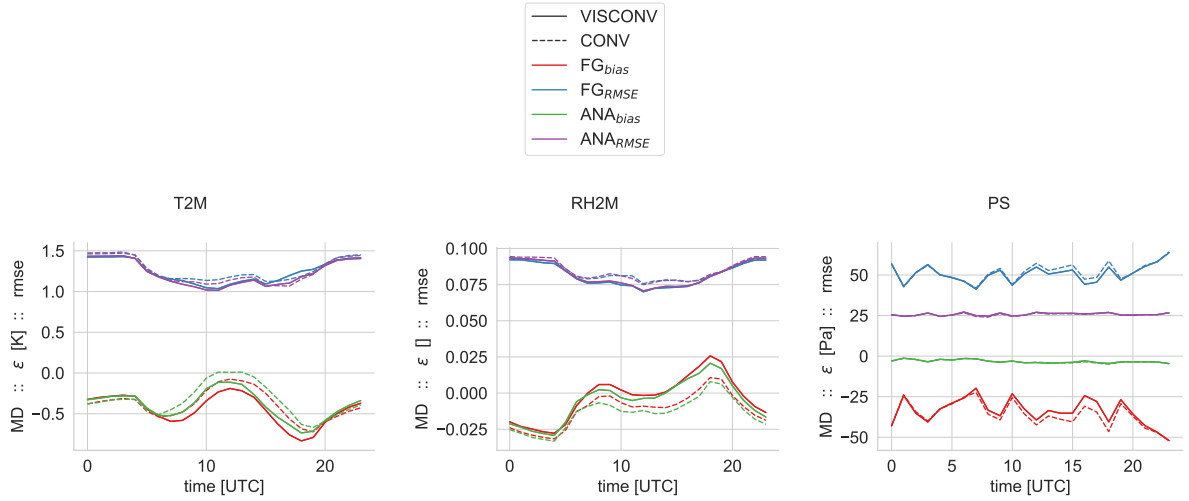

(a) T2m **(b)** RH2m **(c)** PS

Figure 5.8: *Diurnal cycle in root mean squared error and mean difference evaluated with conventional SYNOP observations: (a) temperature at 2m height, (b) relative humidity at 2m height and (c) surface pressure.*

The analysis and the first guess errors show quasi no diurnal variation, and the analysis errors are comparable in both simulations. The error growth during the first hour of model integration is comparable in both experiments, with a rate often greater than 100 % indicating a rapid small-scale error growth. However, reflectance assimilation improves the short-term forecasts. Furthermore, the beneficial impact on the first guess continuously increases from 5 UTC to 18 UTC. This finding could suggest that the analysis is more consistent with the model dynamics or that less spurious imbalances are introduced during the first hour of model integration.

5.3 Evaluation of 24-h forecasts

Sect. 5.2 demonstrated a more realistic representation of solar reflectance in the VISCONV analyses and short-term forecasts. At the same time, the influence on conventional observations is relatively neutral. Therefore, the next discussed subject is what impact we can expect in 24-h forecasts.

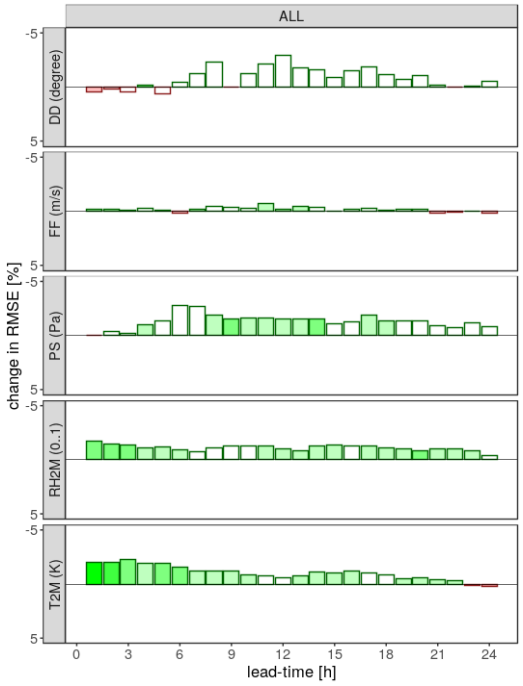

(a) INI=0,6,12 & 18 UTC

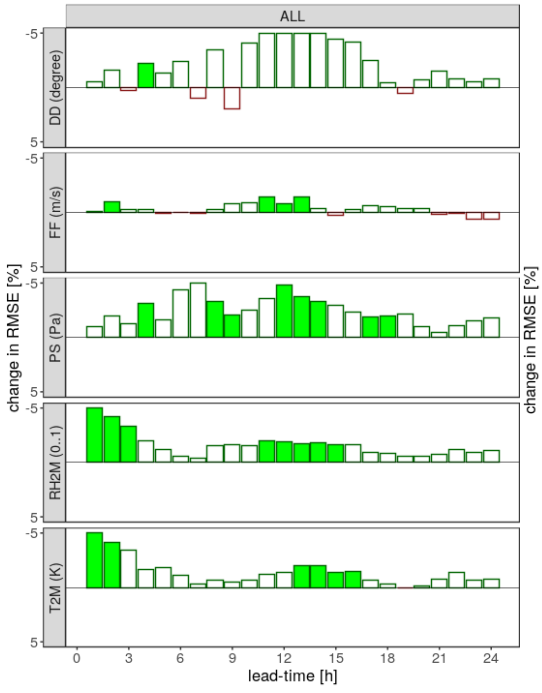

(b) INI=12 UTC

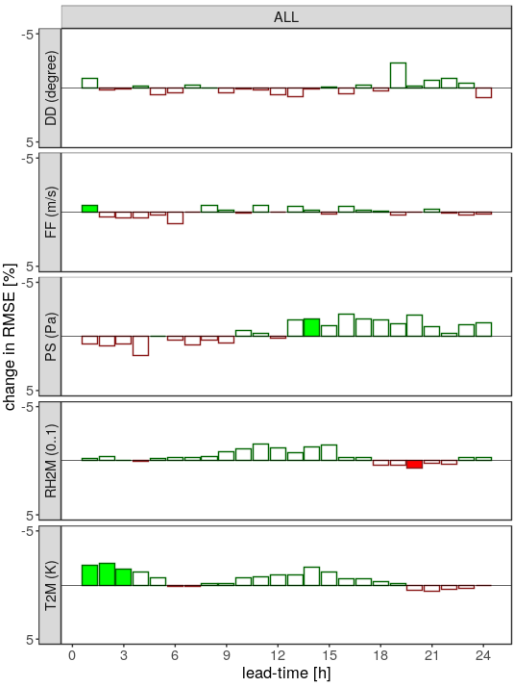

(c) INI=0 UTC

Figure 5.9: *Period mean reduction in root mean squared error (=-1×PI) of VISCONV vs. CONV from DWD's standard verification system using SYNOP observations of all forecast initialisation (a), forecasts initialised at 12 UTC (b) and 0 UTC (c). The average reduction is computed for the entire ICON-D2 domain in July 2019. The quantities are wind direction DD and strength FF, surface pressure PS, relative humidity RH2M and temperature T2m at 2 m height.*

5.3.1 Conventional observations

Figure 5.9 displays the time evolution of 24-h forecasts in RMS error reduction, evaluated against SYNOP observations, using DWD's standard verification system. Averaging all forecast initialisation (0, 6, 12, 18 UTC) exhibits a clear and long-lasting positive impact through reflectance assimilation, particularly in surface pressure, relative humidity and temperature in 2 m height.

However, differences are apparent for different forecast initialisations. For the forecasts initialised at 12 UTC, the positive impact is more pronounced, while for those forecasts initialised at 0 UTC, the influence is relatively neutral. This difference implies that through solar reflectance assimilation, the prediction of surface variables is clearly enhanced and strengthen the hypothesis raised in sect. 5.2.3 that the analysis is either more balanced or more consistent with model dynamics.

Moreover, relative humidity and temperature prediction in the boundary layer profit from reflectance assimilation, on average (Fig. 5.10), while the influence on upper tropospheric humidity and temperature, evaluated with TEMP observations, is relatively neutral. The impact is less evident in the evaluation against wind strength and direction using TEMP and AIREP observations. The evaluation against TEMP wind strength shows a negative impact, while a positive impact is present, using AIREP observations. Vice versa, evaluation of wind direction reveals a positive impact, using TEMP but negative, using AIREP. This discrepancy should be addressed in further studies.

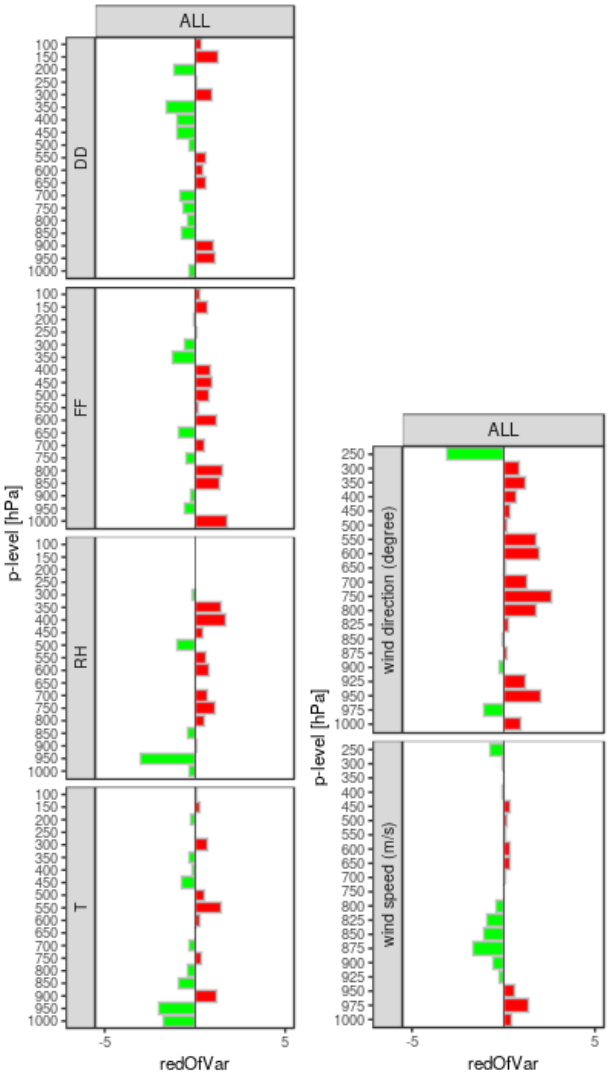

(a) TEMP **(b)** AIREP

Figure 5.10: *Average reduction in root mean squared error (=-1×PI) of VISCONV vs CONV from DWD's standard verification system in TEMP (left) and AIREP (right) observation and the average of all initialisation (0, 6, 12 and 18 UTC). The average reduction is computed for the entire ICON-D2 domain in July 2019. The quantities are wind direction DD and strength FF, relative humidity RH and temperature.*

5.3.2 Cloud distribution

Figure 5.11 comprises the time evolution of solar reflectance FSS and the related PI for the 24-h forecasts, initialised at 0, 6, 12 and 18 UTC. The FSS on a relatively small scale of 24 km and a threshold value of 0.5 reveals the spatiotemporal accuracy in predicting relatively thick clouds. Im-

proving the cloud distribution in the analysis has a long-lasting impact for up to 24 hours.

Comparison of the CONV FSS at t=1h and VISCONV FSS at later forecast lead times shows that we gain approximately four hours in forecasting relatively thick clouds (INI $\in [06, 12]$ UTC). We found similar results when using the 95th percentile threshold ($\overline{R} \approx 0.7$), i.e., very thick clouds and on smaller scales (12 km) and a threshold value of 0.5. In both setups, the FSS decreases faster for forecasts initialised at 12 UTC compared to 06 UTC. This faster error growth is related to locally triggered convection. Overall, a clear positive impact on reflectance forecast is present through reflectance assimilation.

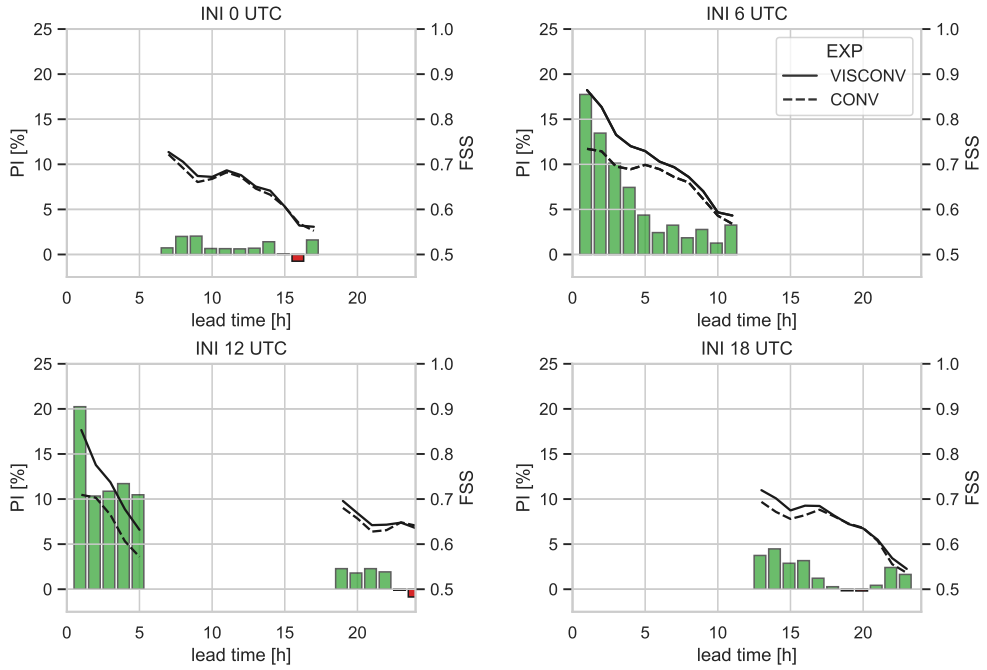

Figure 5.11: *Average (period mean) FSS in 0.6 µm MSG SEVIRI solar reflectance forecast (scale = 24 km, threshold = 0.5) and percentage improvement in FSS against forecast lead time in July 2019. The forecasts are initialised at 0, 6, 12 and 18 UTC.*

5.3.3 Surface irradiance

Global horizontal irradiance at the surface strongly correlates with solar reflectance at TOA. GHI is observed at 209 pyranometer stations. Figure 5.12 demonstrates that GHI is relatively predictable on average, similar to solar power generation forecasts in Germany (Fig. 1.2). Both setups provide realistic radiation forecasts with correlation coefficient $\rho \in [0.94, 0.95]$ (calculated with all observation: each station/prediction time entered directly). However, the contours in VISCONV are narrower. This is the first indicator that the global horizontal irradiance forecast benefits through solar reflectance assimilation. Overall, GHI is overestimated on average (MD $\in [3, 9]$ W/m^2) but reduced in VISCONV. This is in accordance to findings in several other studies (e.g. Remund et al., 2008, Lorenz et al., 2009). Only for the 6 UTC VISCONV simulation GHI is underestimated ($\mathrm{MD_{VISCONV}}$ = -3.1 W/m^2, $\mathrm{MD_{CONV}}$ = 3.6 W/m^2).

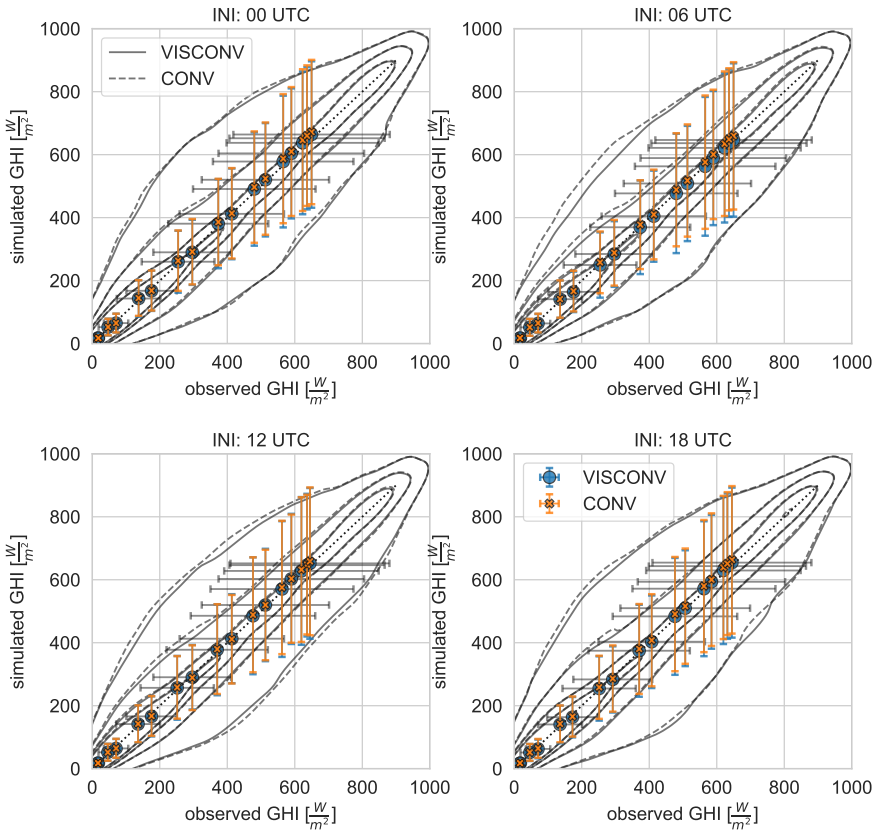

Figure 5.12: *Simulated against observed global horizontal irradiance for forecast initialised at 0, 6, 12 and 18 UTC in July 2019. Dots represent the period and domain averaged values for different lead times. The contours represent a 2D KDE with levels at 95, 75, 50, 25 and 10% for VISCONV (solid) and CONV (dashed) computed for every single day and lead time.*

Fig. 5.13 displays the error evolution in surface global horizontal irradiance forecast. Here, the normalised mean absolute error is shown in order to fairly compare errors introduced by clouds, particularly during morning and evening ramps. Otherwise, the diurnal cycle would dominate the error evolution. However, by norming the errors with the observed values, errors introduced by ICON's 1D-RT scheme (RRTM) become apparent in early morning and evening hours. The introduced error by neglecting 3D effects in both setups is equal, and the comparison should still be fair.

Similar to findings in the reflectance forecasts, a clear beneficial impact is found in predicting GHI that is still present the next day. Therefore, reflectance assimilation enhances the skill in intra-day and day-ahead forecasts, and thus a substantial gain is achieved, valuable for solar power forecasts. Comparing the PIs after one hour lead time for the 6 and 12 UTC forecasts, an error reduction of about 30 % and 22%, respectively, is apparent. This difference in PI is probably due to convection initiation, which is non-deterministic, and thus, random displacement errors in simulated clouds grow faster.

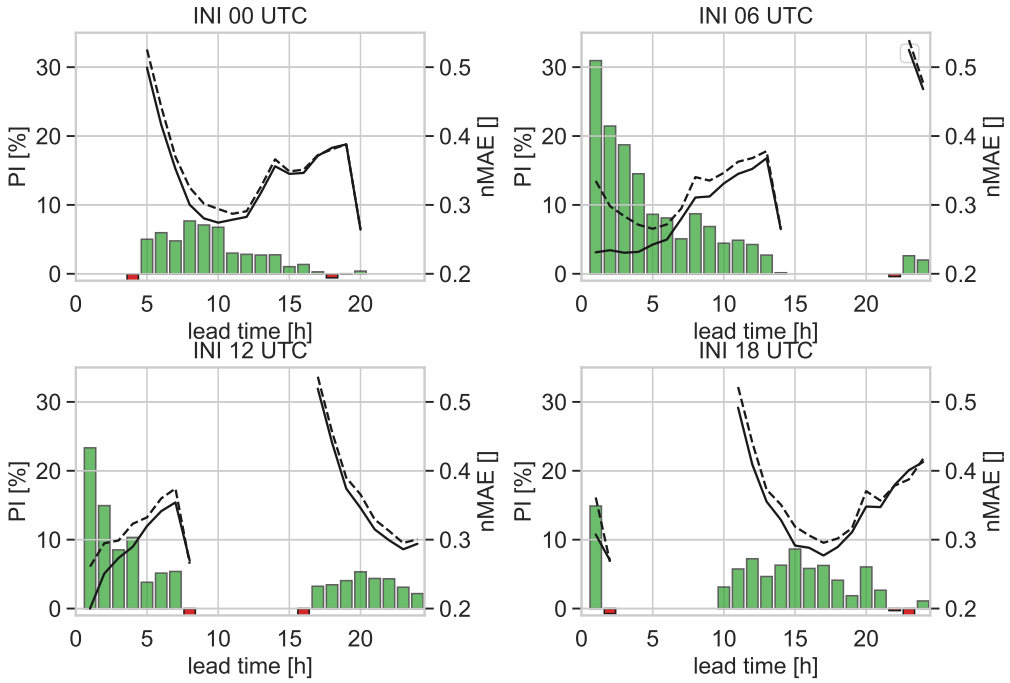

Figure 5.13: *Average (period mean) nMAE in global horizontal irradiance forecast and percentage improvement in FSS against forecast lead time in July 2019. The forecasts are initialised at 0, 6, 12 and 18 UTC.*

5.3.4 Precipitation

Precipitation and, in particular, heavy precipitation events are primary forecasting aspects in convective-scale numerical weather prediction. Precipitation forecast can indicate if the analysis is still consistent with model dynamics and microphysics after the assimilation of solar reflectance. Moreover, precipitation is the only independent metric, besides 2 m temperature and relative humidity.

Fig. 5.14 displays the FSS in the precipitation forecast, initialised at 0, 6, 12 and 18 UTC, with a spatial scale of 24 km and a fixed precipitation threshold of 1 mm/h. The FSS-values are comparatively low because non-precipitating days (means FSS=0) are considered in the computation, and the window size is relatively small. The results confirm that reflectance assimilation has a clear and long-lasting beneficial impact in forecasting moderate precipitation.

Since the impact of the four forecast initialisation is comparable, we can summarise the four forecast initialisation and compute their average impact to discuss different precipitation thresholds. Fig. 5.15 shows this average impact in FSS, using different thresholds. This result confirms an overall better forecast performance in observable ($\geq$0.1 mm/h), moderate ($\geq$1 mm/h) and heavy precipitation ($\geq$5 mm/h and 99$^{\text{th}}$ percentile). The 99$^{\text{th}}$ percentile corresponds to the 1 % precipitating pixels with the highest values in the observation and simulation, respectively. A percentile threshold ensures a fair comparison if simulation or observation is biased. The weakest impact is apparent in the first hour of model integration and likely caused by spin-up in precipitation formation in NWP-models

(e.g. Schraff et al., 2016).

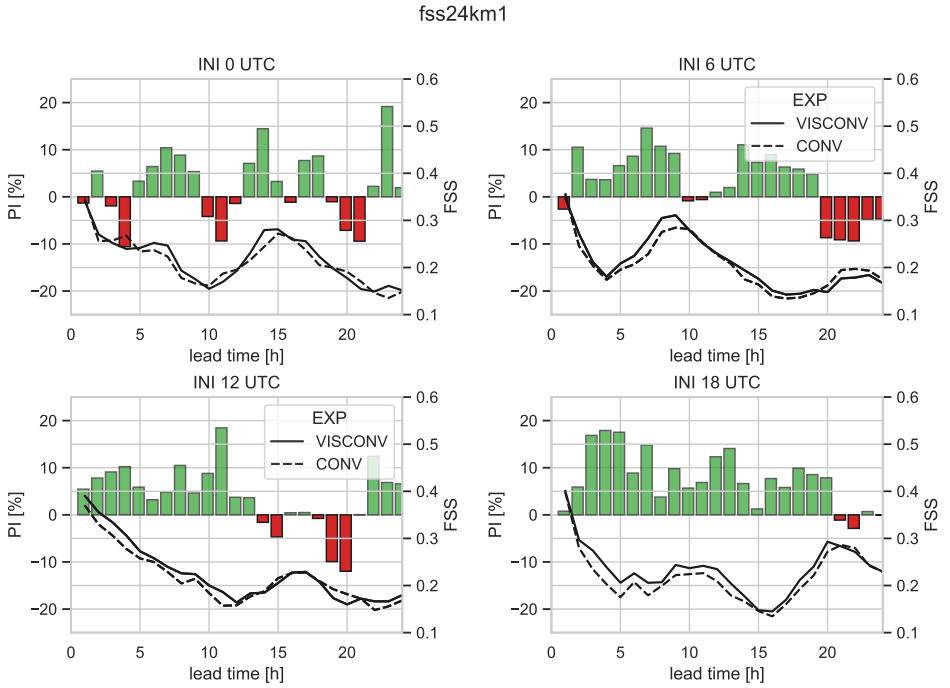

Figure 5.14: *Average (period mean) FSS in precipitation forecast (scale = 24 km, threshold = 1 mm) and percentage improvement in FSS against forecast lead time in July 2019. The forecasts are initialised at 0, 6, 12 and 18 UTC.*

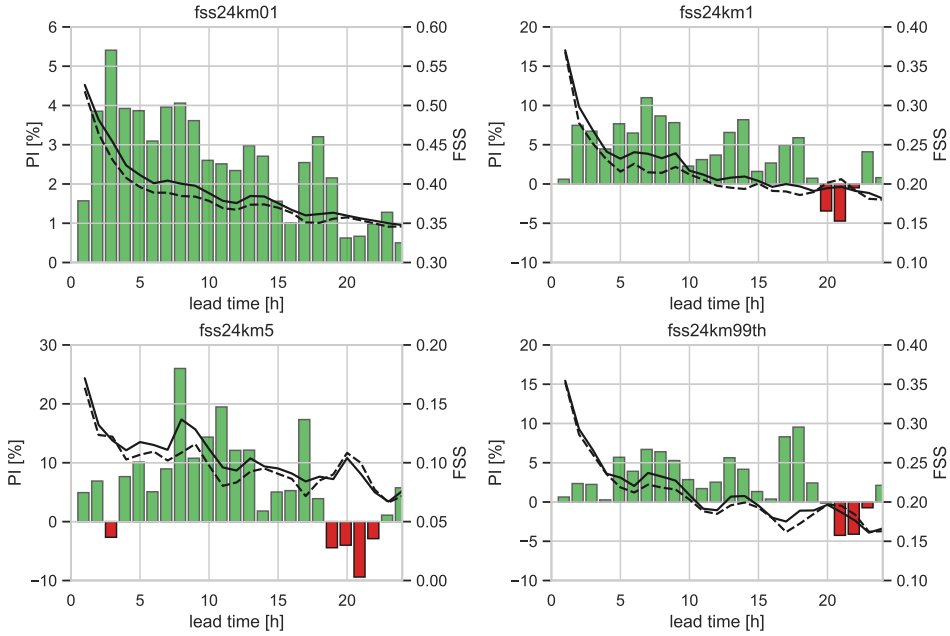

Figure 5.15: *Like Fig. 5.14 but the average of all forecast initialisation with precipitation threshold of 0.1 mm (top left), 1 mm (top right), 5 mm (bottom left) and the 99th percentile (bottom right) on a scale of 24 km.*

5.4 Reflectance and solar power error dependency and reduction

The previous section confirmed that reflectance assimilation has an overall beneficial impact in forecasting reflectance and global horizontal irradiance for up to 24 h. Solar reflectance at TOA and surface global horizontal strongly correlate (Fig. 3.5). This section demonstrates how surface irradiance error depends on TOA solar reflectance error and confirms that improvements in predicting GHI are related to a better representation of clouds initially and in the forecast. Afterwards, the gain one could expect in updating a forecast in the two setups is quantified.

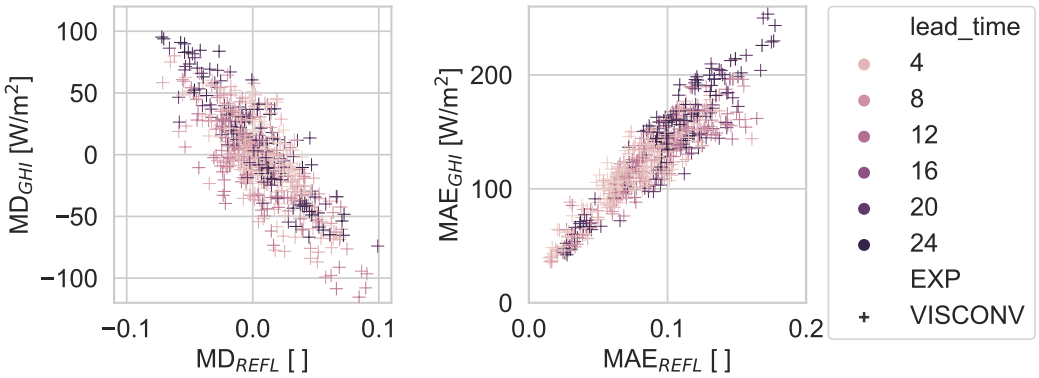

Figure 5.16: *Mean difference error (left) and mean absolute error (right) dependency in collocated surface global horizontal irradiance (divided by cos(sza)) and 0.6 µm MSG SEVIRI solar reflectance at pyranometer stations. Forecasts are initiated at 06 and 12 UTC. Each + represents an average of all pyranometer stations inside the evaluation domain.*

Reflectance and surface irradiance forecast error dependency

In order to examine the impact of reflectance assimilation, we only display the 6 and 12 UTC forecasts. Reflectance observations are superobbed around each surface pyranometer station (nearest nine neighbouring satellite pixels) to reduce sampling errors between satellite observations and surface stations.

Fig. 5.16 displays the dependency of collocated global horizontal irradiance and solar reflectance errors. It becomes evident that improving the model representation of clouds improves surface irradiance. The correlation coefficient ρ between these two errors is -0.8 (p-value $< 10^{-100}$). Therefore, a change in reflectance MD of approximately $\pm$ 0.01 results in a global horizontal irradiance MD of $\mp$ 10 W/m^2, on average. Overall, the reflectance MD is slightly positive (4.9x10^{-3}), whereas GHI MD is negative (-0.7 W/m^2). Most NWP models overestimate radiation due to the lack of cloud representation (Mathiesen et al. (2013) and references therein).

We found a similar but somewhat higher correlation between the mean absolute errors (ρ=0.9, p-value$< 10^{-200}$). Here, it becomes evident that the errors grow in a quasi-linear dependency with forecast lead time. The relatively low errors for longer lead times are

clear-sky days (bottom left corner). If no clouds are present, the errors in global horizontal irradiance are smaller by their very nature. Once again, these results confirm that improving the (spatiotemporal) representation of reflectance in the analyses and in the forecasts, using visible satellite observations, enhances radiation forecast.

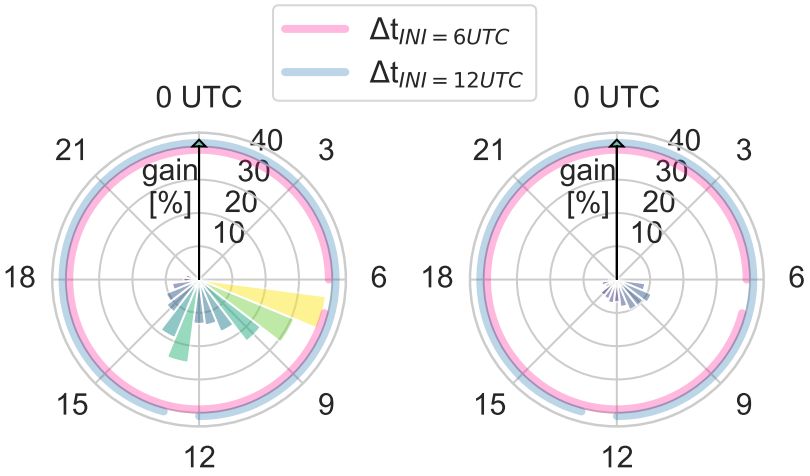

Figure 5.17: *Period mean gain in global horizontal irradiance forecast through a forecast update in VISCONV (left) and CONV (right). Comparison of 6 UTC (pinkish) and 12 UTC (bluish) forecasts (Δt=6h) and vice versa (Δt=18h).*

Gain in predicting solar power by updating a forecast

One main challenge regarding solar power prediction is forecast errors in day-ahead forecasts that persist after an intra-day forecast update (Siefert et al., 2017). In order to examine the impact of reflectance assimilation, errors in the global horizontal irradiance forecast of the CONV and VISCONV setup are evaluated individually.

This section compares the 12 UTC and the 6 UTC forecast the next day, providing a time lag of 18 hours. The 6 UTC and 12 UTC forecasts on the same day are compared, leading to a time lag of six hours. Therefore, the gain in global horizontal irradiance by updating a forecast becomes apparent. Fig. 5.17 shows the error reduction after updating a forecast with a time lag of six and 18 hours, respectively. For Δt=6 h, the error in the conventional setup is reduced by 8 % at 13 UTC. For a time lag of 18 h (7 UTC), the reduction is still comparable in CONV. This relatively low gain in the conventional setup can be linked to an almost saturated cloud and radiation error when the forecasts are started. In VISCONV, however, the cloud distribution is in better agreement with the observations initially and in subsequent forecasts. Therefore, solar power prediction could benefit three times as much ($\approx$ 26 %) for a time lag of six hours (13 UTC) and for a time lag of 18 h, the error reduction is even close to 40 % (7 UTC).

Hence, a higher update frequency combined with solar reflectance assimilation could improve solar power prediction using convective-scale numerical weather prediction.

5.5 Sensitivity experiments

Chapter 4 demonstrated that considering aerosols and the main 3D RT effects improves the agreement between observed and synthetic satellite images. Hence, including 3D RT and aerosols effects should give an additional benefit. Their influence on the short-term forecasts and the analysis will be discussed next.

Aerosols, clear-sky peak and calibration factor

Aerosols impact solar reflectance directly (see Sect. 4.3.2) and indirectly, as aerosols serve as cloud condensation nuclei. The more water droplets in a cloud (with fixed water content), the lower the effective radius and the more radiation is scattered to the satellite (see Sect. 4.3.3). Additionally, aerosols impact solar power production, especially during Saharan dust outbreaks (e.g. Köhler et al., 2017, Neher et al., 2019). While the correct calibration of solar reflectance observation is uncertain, we found a positive influence by considering aerosols on the stability of the calibration factor during the entire day. Without aerosols, the calibration factor varies, depending on the position of the sun. Additionally, the simulated clear-sky signal is more reliable compared to observations. Fig. 5.18 shows the histograms for 6, 12 and 18 UTC of the observations and the first guess model equivalents as provided by datools and the 3D forward operator. The clear-sky signal's peaks and spread are in better agreement with the observations if an AOD of 0.1 for each satellite pixel is assumed. Hence, considering aerosols improve the first guess solar reflectance distribution and reduces representation error.

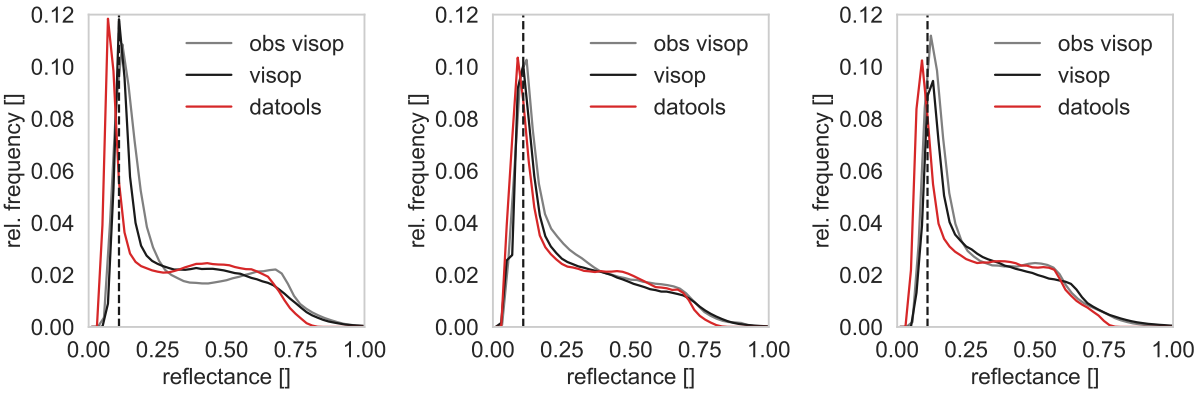

(a) 06 UTC **(b)** 12 UTC **(c)** 17 UTC

Figure 5.18: *Period mean 0.6 µm MSG SEVIRI solar reflectance histograms at 6 (a), 12 (b) and 17 UTC (c) of the first guess from datools and the applied 3D VISOP operator. In datools, no aerosols are considered. VISOP uses an MFASIS lookup table with AOD=0.1 that is assumed for each satellite pixel. The calibration factor for observations is 0.9. The vertical dashed line indicates the reflectance value of the clear-sky peak at 06 UTC.*

3D vs 1D visible forward operator

A simplified version of the forward operator was applied to the first guess to compute the analysis in the data assimilation. In this online operator (datools), 3D-RT effects and snow (online operator) are neglected. Neglecting 3D effects, particularly assuming vertical columns instead of the slant viewing angle of the satellite, can lead to initially displaced clouds. This can lead to systematic deviations in solar reflectance and global horizontal irradiance, particularly during morning and evening times with low sun levels (meaning high solar zenith angles in the MFASIS framework; see Fig. 2.5). Figure 5.19 comprises

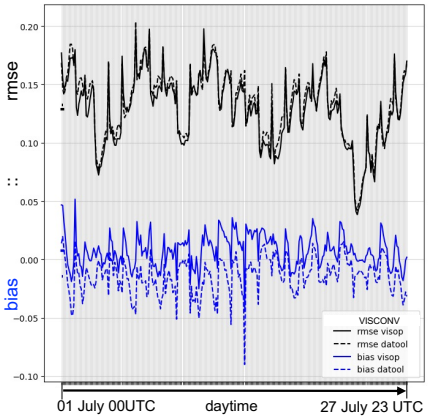

Figure 5.19: *The first guess RMSE and MD in 0.6 µm MSG SEVIRI solar reflectance during cycling evaluated using a 1D (datools) and 3D (VISOP) visible operator for the VISCONV experiment in July 2019.*

the RMSE and MD of the solar reflectance first guess as provided by the online forward operator version (datools) and the 3D operator (VISOP). Both operators are applied to the short-term forecasts. Here, it becomes evident that taking the slant viewing angle and cloud top inclination into account can further improve the solar reflectance field.

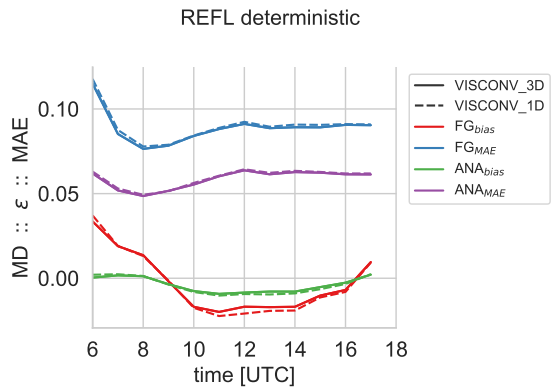

Figure 5.20: *Domain and subperiod (three days from 17. to 20 July 2019) mean 0.6 µm MSG SEVIRI solar reflectance error evolution during cycling in the first guess and the analyses. Assimilation using a 1D and 3D visible operator.*

Due to limitations in computational resources, the full 3D forward operator and the forward operator assuming vertical columns (1D) were applied to compute the analysis only for a shorter period (17. July 13 UTC to 20. July 17 UTC). Fig. 5.20 shows the subperiod mean error evolution in solar reflectance at each analysis time step. Here, a slight improvement is also apparent in the mean differences and the mean absolute errors. This subperiod was predominantly characterised by synoptically forced convection. For other scenes with locally triggered convection, the effect should be more pronounced. Furthermore, a 3D operator version will become more valuable when model and satellite observation resolutions increase in future.

5.6 Summary

In this chapter, visible satellite observations are used to demonstrate their potential in convective-scale numerical weather prediction. A summer period of four weeks was simulated using two setups of observations to compute the analysis. The first setup uses only conventional observations, and the second setup incorporates solar reflectance observations from 6 to 17 UTC. The analyses are computed every hour, and 24-h forecasts are initialised every six hours at 0, 6, 12 and 18 UTC.

The assimilation of solar reflectance reduces the mean errors substantially in the solar reflectance analysis at each data assimilation time step. The analyses errors in reflectance are almost half of the conventional setup because no error reduction is present in the conventional setup. Adjusting the cloud thickness is the dominant process in reducing solar reflectance errors. In short-term forecasts, almost no thick clouds are displaced when visible satellite observations are assimilated, unlike the conventional setup. Moreover, the first guess departures are almost Gaussian distributed if clear-sky pixels in both the observation and the first-guess are excluded. Overall, the accuracy of cloud distribution is in better agreement with the observations in the analysis and the first guess when solar reflectance is assimilated. If aerosols, the parallax correction and cloud top inclination are considered in the visible forward operator, potentially, synthetic visible satellite images can be further improved. Moreover, considering aerosols in the visible forward operator stabilises the calibration factor of the observations and the clear-sky peak (distribution) during the day.

The evaluation against conventional observations reveals an almost neutral impact in the analysis and short-term forecasts. However, model equivalents in the boundary layer and close to the Earth's surface are in better agreement with the observations. The evaluation of 24-h forecasts reveals that temperature, relative humidity at 2m height and in the boundary layer plus surface pressure profit by assimilating solar reflectances. In contrast, the averaged impact on variables in the middle and upper troposphere is slightly negative in the 24-h forecasts.

However, by assimilating visible satellite observations, day-ahead and intra-day forecasts of solar reflectance and global horizontal irradiance are improved as errors in both variables strongly correlate. The positive impact is apparent up to 24 hours lead time. Moreover, updating a forecast with a time lag of six hours reduces the average error by 26 % and, after 18 hours, by 40 % during the first hour of the comparison. In contrast, using only conventional observations, the error reductions are comparatively low and approximately 8 % for both time-lags. Last but not least, precipitation forecasts of observable, moderate and heavy precipitation is slightly improved up to 18 hours.

Overall, representing cloud information in the analysis using visible satellite observations possesses a vast potential for convective-scale numerical weather prediction, particularly for cloud and radiation forecasts.

Chapter 6

Conclusion

Satellite observations provide a crucial source of information for convective-scale numerical weather prediction with untapped potential for model cloud evaluation and to represent small-scale cloud structures in the analysis. In the past, the focus in NWP was not necessarily on accurate cloud representation. Model clouds, in particular ice clouds, are often used to tune the net TOA radiative flux. However, on the convective scale, moisture processes become comparatively more important. Moist physical processes are diabatic and often occur in regions with thermodynamic instability in the atmosphere. The dilemma is that the conventional observing system provides limited information about small-scale cloud processes and distribution. This is where satellite observations come into play. For the first time, this thesis has demonstrated the potential in using satellite observations for model cloud evaluation and assimilation using fast and operationally applicable forward operators. The used forward operators generate synthetic satellite images in quasi real-time.

This thesis examines two approaches employing the recently operational regional ICON-D2 model of Deutscher Wetterdienst. First, understanding the model representation clouds and systematic deviations from a satellite's point of view for a high impact weather period of 30 days. Systematic deviations can cause severe issues in data assimilation, introducing inconsistency between the generated analysis and model (thermo-) dynamics. Second, estimating potentials in assimilating visible satellite observations for convective-scale numerical weather prediction for a multi-week period, characterised by various weather conditions and different cloud formation processes.

Evaluation of model clouds

Previous studies often compare quantities retrieved from satellite observations to the model state. However, this thesis performs the comparison in observation space using synthetic satellite images generated by forward operators. An advantage of this approach is that errors in synthetic images are easier to characterise than for retrievals. Using visible satellite images generated by a fast forward operator in this approach is not yet well-established for evaluation. Hence, sensitivity experiments with modified operator settings reveal the recently developed forward operator's uncertainty. The comparison of several perturbed model simulations and VISOP settings reveals that the operator is accurate and further emphasises the usefulness of solar channels for model evaluation and improvement.

The combination of observations in two spectral ranges provides significantly more and complementary information than the individual channels. Infrared observations provide information on cloud top height since their signal quickly saturates in the presence of clouds. This means that infrared observations can only distinguish a comparatively small range in cloud water path. Moreover, information on water clouds may be obscured by cirrus clouds above. In contrast, visible channels are less sensitive to ice clouds but can distinguish a much more extensive cloud water path (liquid and solid) range. The developed approach is successfully used at DWD to test model changes and to optimise model parameters. This has already reduced systematic errors in the ice clouds in the ICON model. The developed approach could also constrain clouds in climate models, as clouds are one of the primary error sources in climate sensitivity estimates (Solomon et al., 2007).

The combined use of visible and infrared observations is novel. It allows identifying specific model deficiencies, e.g. too many high cirrus clouds, too weak shallow convection, deficiencies in the model representation of subgrid clouds, too strong deep convection or too much production of cloud ice. Several model sensitivity experiments targeted these deficiencies and point towards potential approaches for model improvement. However, solving these challenging issues will require additional studies, given the number of interacting processes that contribute to clouds' formation, modification, and dissipation.

It is of utmost importance to advance the representation of clouds to use cloud-affected satellite observations in data assimilation more effectively. As the analysis using an LETKF is a linear combination of an ensemble of 1-h short-term forecasts, systematic biases in cloud distribution could introduce inconsistency between the analysis and model (thermo-) dynamics and, e.g. triggering spurious convection.

Assimilation of visible satellite images

Assimilating visible satellite channels reduces cloud distribution errors substantially in the analyses and the short term forecasts. In particular, errors in cloud thickness, followed by false-alarm and miss errors, are reduced. Using findings from the previous experiment, an advantage of visible over infrared channels becomes apparent in adjusting cloud thickness through their assimilation. The infrared signal is often already saturated for pixels in which clouds are both observed and simulated. Still, information from an infrared channel could be helpful to constrain cloud top height or using the near-infrared 1.6 μm channel that distinguishes between water and ice clouds (Wolters et al., 2008). Furthermore, first guess departures in solar reflectance are quasi-Gaussian distributed if clear-sky pixels in both observation and short-term forecasts are excluded (correctly negative). A more sophisticated approach to improve solar reflectance assimilation is to develop an adaptive error model that is successfully used for infrared channels (e.g. Harnisch et al., 2016, Geer, 2019).

Rapid updates in NWP systems can introduce balance and noise during the first hour of model integration (Gustafsson et al., 2018). Therefore, it is mandatory to evaluate temperature, humidity, wind and surface pressure in the analyses and short term forecasts. Slight improvements are apparent in the analysis and the first guess of 2m temperature and humidity fields and surface pressure. Indications were found that the thermodynamic state is improved in the boundary layer while worsened in the middle and upper troposphere. This finding can partly be attributed to model cloud distribution biases (as the analysis is a

linear combination) and partly because these observations have simply more weight in the computation of the analysis in the conventional setup. Moreover, dependent verification metrics can often be misleading in estimating the impact, as Necker et al. (2018) has shown, for example. In addition, the errors themselves and hence error differences in temperature, surface pressure, humidity, and wind are relatively low compared to error differences in clouds and radiation. There, errors are more likely to occur in the order of some deca- per cent.

The visible forward operator accounting for the main 3D effects, meaning cloud top inclination and a parallax correction, is superior to the 1D implementation. Additionally, taking aerosol optical depth into account stabilise the calibration of solar reflectance observations and improves the (variability of the) clear sky peak during the whole day. In the standard RT-solver MFASIS of the visible operator, the number of input parameters is limited due to computational efficiency. Using a neural network-based forward operator (Scheck, 2021) aerosols could be directly used as input, e.g. from a numerical forecast that DWD currently develops for mineral dust (PerduS, PermaStrom). This could make the assimilation of visible satellite observations more effective, as aerosols can be detected in the solar spectral range and often, Aerosols like from Saharan dust outbreaks severely impact solar power generation (Bachmann, 2021).

Improvements in cloud-related forecasts

Weather forecast is mostly improved through the assimilation of visible satellite observations. The most considerable positive impact is in predicting the solar reflectance at TOA and the surface global horizontal irradiance. The positive influence holds up to 24 hours of model integration. Errors in surface irradiance are reduced since these errors correlate strongly with those in solar reflectance ($|\rho| \in [0.8, 0.9]$). This finding confirms the vast potential in solar power prediction using NWP by tuning and improving solar reflectance analysis and forecast. However, there are further potentials in solar power forecast, as errors introduced by the two-stream 1D-radiative transfer scheme often dominate, particularly during morning and evening hours. Additional solar power forecast skills are possible using a more sophisticated RT scheme like a TenStream solver (Jakub and Mayer, 2015) accounting for 3D effects, instead of the meanwhile outdated operational two-stream solver RRTM. In the current operational ICON version, ecRAD (Hogan and Bozzo, 2016) is implemented, containing three RT-solvers, with a possible account for subgrid 3D radiative effects, cloud inhomogeneity, aerosol optical depths and others (Schäfer et al., 2021). Global horizontal irradiance forecasts should benefit from this new RT scheme.

Still, by assimilating solar reflectances, surface global horizontal irradiance errors in day-ahead forecasts are strongly reduced in intraday updates: -40 %, for a time lag of 18 h, and - 26 % for a time lag of 6 h, during the first hour of the comparison. This finding argues for more frequent forecast updates (operationally currently every three hours). However, only if solar reflectance is assimilated (or something similar) because the error reductions are relatively low and relatively independent of the considered time lags (6 and 18 h) in the conventional setup. This relatively low gain suggests that solar reflectance and global horizontal irradiance errors are initially almost saturated.

Finally, there remains precipitation as an independent metric. Assimilation of solar reflectances enhances the spatio-temporal distribution of precipitation. There is a clear

positive influence for measurable (rr>0.1 mm/h) and moderate (rr=1 mm/h) precipitation, as well as for heavy rainfall events (rr>5 mm/h). The positive influence lasts on average up to 18 hours. Hence, assimilating solar reflectances indicates a more consistent analysis with the model's thermodynamics and/or introduces fewer imbalances.

All in all, satellite observations provide valuable information to evaluate, tune, and assimilate clouds. In future, weather services should exploit this information to improve cloud-related weather forecasts, predictions of photovoltaics power generation and, last but not least, enhance the representation of model clouds in climate simulations.

Appendix A

Contribution of journal publications to this dissertation

This dissertation includes results from a journal article. Table A.1 provides an overview of the contribution of the article to this dissertation. The table lists all sections that are based on content from the publication.

Table A.1: *Contribution of a journal publication to this dissertation.*

Geiss et al. (2021)
Section 1.2
Section 3.1
Section 3.2
Section 3.3
Section 4.1
Section 4.2
Section 4.3

List of Abbreviations

Abbreviation	Description
AIREP	Aircraft observations
BC	Boundary Conditions
BT	Brightness temperature
CONV	Simulations using only conventional observations in DA
COSMO	COnsortium for Small-scale MOdeling
DA	Data Assimilation
DWD	Deutscher Wetterdienst
EUMETSAT	European Organisation for the Exploitation of Meteorological Satellites
FSS	Fractions skill score
GHI	Global horizontal irradiance at the Earth's surface
IC	Initial conditions
ICON	Icosahedral Nonhydrostatic
ICON-D2	Icosahedral Nonhydrostatic Deutschland 2.1 km
ICON-EU	Icosahedral Nonhydrostatic Europa
IR	Infrared
IR108	MSG SEVIRI 10.8 μm channel
LETKF	Local Ensemble Transform Kalman Filter
MSG	Meteosat Second Generation
MFASIS	Method for FAst Satellite Image Simulation
MAE	Mean absolute error
MW	Microwave
NWP	Numerical Weather Prediction
PDF	Probability density function
PI	Percentage improvement
PROF	Wind profiler observations
PS	Surface pressure
R	Solar reflectance at top of atmosphere
RADOLAN	Radar-based precipitation product
RH	Relative Humidity
RMSE	Root mean squared error
rr	Precipiation rate
RTTOV	Radiative Transfer for TOVS
SEVIRI	Spinning Enhanced Visible and InfraRed Imager
SYNOP	Surface observations
sza	solar zenith angle

T	Temperature
TEMP	Radiosonde/Sounding observations
TOA	Top of atmosphere
UTC	Coordinated Universal Time
VIS	Visible
VIS006	MSG SEVIRI 0.6 μm channel
VISCONV	Simulations using VIS satellite and conventional observations in DA
VISOP	Visible forward operator

List of Figures

Bibliography

Bachmann, K., C. Keil, G. C. Craig, M. Weissmann, and C. A. Welzbacher, 2020: Predictability of deep convection in idealized and operational forecasts: Effects of radar data assimilation, orography, and synoptic weather regime. *Monthly Weather Review*, **148 (1)**, 63–81.

Bachmann, V., 2021: The project perdus and permastrom: Daily mineral dust forecasts using icon-art. DWD, `https://www.dwd.de/EN/specialusers/research_education/seminar/2021/iccarus2021/presentations/friday_04_bachmann.pdf?view=nasPublication&nn=721380`, last accessed on 23/08/21.

Baldauf, M., C. Gebhardt, S. Theis, B. Ritter, and C. Schraf, 2018: Beschreibung des operationellen kürzestfristvorhersagemodells cosmo-d2 und cosmo-d2-eps und seiner ausgabe in die datenbanken des dwd.(2018).

Bauer, P., A. J. Geer, P. Lopez, and D. Salmond, 2010: Direct 4d-var assimilation of all-sky radiances. part i: Implementation. *Quarterly Journal of the Royal Meteorological Society*, **136 (652)**, 1868–1885.

Bauer, P., G. Ohring, C. Kummerow, and T. Auligne, 2011a: Assimilating satellite observations of clouds and precipitation into nwp models. *Bulletin of the American Meteorological Society*, **92 (6)**, ES25–ES28.

Bauer, P., A. Thorpe, and G. Brunet, 2015: The quiet revolution of numerical weather prediction. *Nature*, **525 (7567)**, 47–55.

Bauer, P., T. Auligné, W. Bell, A. Geer, V. Guidard, S. Heilliette, M. Kazumori, M.-J. Kim, E. H.-C. Liu, A. P. McNally, B. Macpherson, K. Okamoto, R. Renshaw, and L.-P. Riishøjgaard, 2011b: Satellite cloud and precipitation assimilation at operational nwp centres. *Quarterly Journal of the Royal Meteorological Society*, **137 (661)**, 1934–1951.

Baum, B. A., P. Yang, A. J. Heymsfield, A. Bansemer, B. H. Cole, A. Merrelli, C. Schmitt, and C. Wang, 2014: Ice cloud single-scattering property models with the full phase matrix at wavelengths from 0.2 to 100μm. *Journal of Quantitative Spectroscopy and Radiative Transfer*, **146**, 123 – 139, doi:https://doi.org/10.1016/j.jqsrt.2014.02.029, URL `http://www.sciencedirect.com/science/article/pii/S0022407314000867`, electromagnetic and Light Scattering by Nonspherical Particles XIV.

Bechtold, P., N. Semane, P. Lopez, J.-P. Chaboureau, A. Beljaars, and N. Bormann, 2014: Representing equilibrium and nonequilibrium convection in large-scale models. *Journal of*

the Atmospheric Sciences, **71 (2)**, 734 – 753, doi:10.1175/JAS-D-13-0163.1, URL https://journals.ametsoc.org/view/journals/atsc/71/2/jas-d-13-0163.1.xml.

Behrens, K., R.-D. Grewe, O. Lindenberg, and A. Observatorium, 2005: A comparison of scapp radiation data with global, diffuse and direct solar radiation. *WMO Technical Conference on Meteorological and Environmental Instruments and Methods of Observation (TECO-2005)*, Vol. 1265.

BMWi, 2021: Neuer bund-länder-kooperationsausschuss zum ausbau erneuerbarer energien tagt erstmalig und bringt monitoring auf den weg. Bundesministerium für Wirtschaft und Energie, URL https://www.bmwi.de/Redaktion/DE/Pressemitteilungen/2021/03/20210324-neuer-bund-laender-kooperationsausschuss-zum-ausbau-erneuerbarer-energien-br html.

Böhme, T., S. Stapelberg, T. Akkermans, S. Crewell, J. Fischer, T. Reinhardt, A. Seifert, C. Selbach, and N. Van Lipzig, 2011: Long-term evaluation of cosmo forecasting using combined observational data of the gop period. *Meteorologische Zeitschrift*, **20 (2)**, 119–132.

BReg, 2021: Ein neues zeitalter hat begonnen. Presse- und Informationsamt der Bundesregierung, URL https://www.bundesregierung.de/breg-de/themen/energiewende/energie-erzeugen/erneuerbare-energien-317608.

Burger, B., 2021a: Jährlicher Anteil der Solarenergie an der Stromerzeugung in Deutschland. Fraunhofer-Institut für Solare Energiesysteme ISE, Freiburg, Germany, URL https://energy-charts.info/charts/renewable_share/chart.htm?l=de&c=DE&interval=year&share=solar_share&partsum=1.

Burger, B., 2021b: Solar Prognose vs. Hochrechnungs-Istwert in Deutschland im Juli 2019. Fraunhofer-Institut für Solare Energiesysteme ISE, Freiburg, Germany, URL https://energy-charts.info/charts/power_scatter/chart.htm?l=de&c=DE&year=2019&interval=month&dataType=solar_ante_post&download-format=application%2Fpdf&month=07.

Chandrasekhar, S., 2013: *Radiative transfer*. Courier Corporation.

Cohn, S., 2017: A new edition of the international cloud atlas. *WMO Bulletin, Geneva, World Meteorological Organization*, **66**, 2–7.

Craig, G. C. and A. Dörnbrack, 2008: Entrainment in cumulus clouds: What resolution is cloud-resolving? *Journal of the atmospheric sciences*, **65 (12)**, 3978–3988.

Crook, N. A., 1996: Sensitivity of moist convection forced by boundary layer processes to low-level thermodynamic fields. *Monthly Weather Review*, **124 (8)**, 1767 – 1785, doi:10.1175/1520-0493(1996)124⟨1767:SOMCFB⟩2.0.CO;2, URL https://journals.ametsoc.org/view/journals/mwre/124/8/1520-0493_1996_124_1767_somcfb_2_0_co_2.xml.

De Villiers, M., 2020: Europe extreme heat 22–26 july 2019: was it caused by subsidence or advection? *Weather*, **75 (8)**, 228–235.

Desroziers, G., L. Berre, B. Chapnik, and P. Poli, 2005: Diagnosis of observation, background and analysis-error statistics in observation space. *Quarterly Journal of the Royal Meteorological Society: A journal of the atmospheric sciences, applied meteorology and physical oceanography*, **131 (613)**, 3385–3396.

DWD, 2020a: Modifications in the data assimilation for cosmo-d2, cosmo-d2-eps. Forschung und Entwicklung - Abteilung Meteorologische Analyse und Modellierung, https://www.dwd.de/DE/fachnutzer/forschung_lehre/numerische_wettervorhersage/nwv_aenderungen/_functions/DownloadBox_modellaenderungen/cosmo_d2/pdf_2018_2020/pdf_cosmo_d2_17_06_2020.pdf?__blob=publicationFile&v=2, last accessed on 17/08/21.

DWD, 2020b: RADOLAN-Kurzbeschreibung. DWD-Hydrometeorologie, https://www.dwd.de/DE/leistungen/radolan/radarniederschlagsprodukte/radolankurzbeschreibung_pdf.pdf?__blob=publicationFile&v=7, last accessed on 17/08/21.

DWD, 2021a: Extension of ICON-D2 forecasts up to 48h. Forschung und Entwicklung - Abteilung Meteorologische Analyse und Modellierung, https://www.dwd.de/DE/fachnutzer/forschung_lehre/numerische_wettervorhersage/nwv_aenderungen/_functions/DownloadBox_modellaenderungen/icon_d2/pdf_2021/pdf_icon_d2_23_06_2021.pdf?__blob=publicationFile&v=3, last accessed on 17/08/21.

DWD, 2021b: Extension of ICON-D2 forecasts up to 48h. Forschung und Entwicklung - Abteilung Meteorologische Analyse und Modellierung, https://www.dwd.de/DE/fachnutzer/forschung_lehre/numerische_wettervorhersage/nwv_aenderungen/_functions/DownloadBox_modellaenderungen/icon_d2/pdf_2021/pdf_icon_d2_system_26_05_2021.pdf?__blob=publicationFile&v=6, last accessed on 17/08/21.

DWD, 2021c: Model configuration upgrade of ICON. Forschung und Entwicklung - Abteilung Meteorologische Analyse und Modellierung, https://www.dwd.de/DE/fachnutzer/forschung_lehre/numerische_wettervorhersage/nwv_aenderungen/_functions/DownloadBox_modellaenderungen/icon_d2/pdf_2021/pdf_icon_d2_14_04_2021.pdf?__blob=publicationFile&v=3, last accessed on 17/08/21.

DWD, 2021d: RADOLAN-Produktübersicht. DWD-Hydrometeorologieg, https://www.dwd.de/DE/leistungen/radolan/produktuebersicht/radolan_produktuebersicht_pdf.pdf?__blob=publicationFile&v=9, last accessed on 17/08/21.

Emde, C., 2018: Scattering phase function as function of particle size (water cloud). Meteorological Institute Munich, https://www.meteo.physik.uni-muenchen.de/~emde/doku.php?id=teaching:radiative_transfer:mie_phase, last accessed on 24/08/21.

Emde, C., R. Buras-Schnell, A. Kylling, B. Mayer, J. Gasteiger, U. Hamann, J. Kylling, B. Richter, C. Pause, T. Dowling, and L. Bugliaro, 2016: The libradtran software package for radiative transfer calculations (version 2.0.1). *Geoscientific Model Development*,

9 (5), 1647–1672, doi:10.5194/gmd-9-1647-2016, URL https://gmd.copernicus.org/articles/9/1647/2016/.

Errico, R. M., P. Bauer, and J.-F. Mahfouf, 2007: Issues regarding the assimilation of cloud and precipitation data. *Journal of the Atmospheric Sciences*, **64 (11)**, 3785 – 3798, doi:10.1175/2006JAS2044.1.

Franklin, C. N., Z. Sun, D. Bi, M. Dix, H. Yan, and A. Bodas-Salcedo, 2013: Evaluation of clouds in access using the satellite simulator package cosp: Global, seasonal, and regional cloud properties. *Journal of Geophysical Research: Atmospheres*, **118 (2)**, 732–748.

Frèrebeau, P., 2014: A fast radiative transfer model for the simulation of visible satellite imagery. http://nbn-resolving.de/urn:nbn:de:bvb:19-170752, last accessed on 17/08/21.

Fu, Q., 1996: An accurate parameterization of the solar radiative properties of cirrus clouds for climate models. *Journal of Climate*, **9 (9)**, 2058–2082.

Geer, A., F. Baordo, N. Bormann, P. Chambon, S. English, M. Kazumori, H. Lawrence, P. Lean, K. Lonitz, and C. Lupu, 2017: The growing impact of satellite observations sensitive to humidity, cloud and precipitation. *Quarterly Journal of the Royal Meteorological Society*, **143 (709)**, 3189–3206.

Geer, A. J., 2019: Correlated observation error models for assimilating all-sky infrared radiances. *Atmospheric Measurement Techniques*, **12 (7)**, 3629–3657.

Geer, A. J., P. Bauer, and P. Lopez, 2010: Direct 4d-var assimilation of all-sky radiances. part ii: Assessment. *Quarterly Journal of the Royal Meteorological Society*, **136 (652)**, 1886–1905.

Geer, A. J., K. Lonitz, P. Weston, M. Kazumori, K. Okamoto, Y. Zhu, E. H. Liu, A. Collard, W. Bell, S. Migliorini, et al., 2018: All-sky satellite data assimilation at operational weather forecasting centres. *Quarterly Journal of the Royal Meteorological Society*, **144 (713)**, 1191–1217.

Geiss, S., L. Scheck, A. de Lozar, and M. Weissmann, 2021: Understanding the model representation of clouds based on visible and infrared satellite observations. *Atmospheric Chemistry and Physics*, **21 (16)**, 12 273–12 290.

Giles, D. M., A. Sinyuk, M. G. Sorokin, J. S. Schafer, A. Smirnov, I. Slutsker, T. F. Eck, B. N. Holben, J. R. Lewis, J. R. Campbell, E. J. Welton, S. V. Korkin, and A. I. Lyapustin, 2019: Advancements in the aerosol robotic network (aeronet) version 3 database – automated near-real-time quality control algorithm with improved cloud screening for sun photometer aerosol optical depth (aod) measurements. *Atmospheric Measurement Techniques*, **12 (1)**, 169–209, doi:10.5194/amt-12-169-2019, URL https://www.atmos-meas-tech.net/12/169/2019/.

Gustafsson, N., T. Janjić, C. Schraff, D. Leuenberger, M. Weissmann, H. Reich, P. Brousseau, T. Montmerle, E. Wattrelot, A. Bučánek, et al., 2018: Survey of data

assimilation methods for convective-scale numerical weather prediction at operational centres. *Quarterly Journal of the Royal Meteorological Society*, **144 (713)**, 1218–1256.

Häckel, H., 2016: *Meteorologie*. UTB.

Harnisch, F., M. Weissmann, and Á. Periáñez, 2016: Error model for the assimilation of cloud-affected infrared satellite observations in an ensemble data assimilation system. *Quarterly Journal of the Royal Meteorological Society*, **142 (697)**, 1797–1808.

Heinze, R., et al., 2017: Large-eddy simulations over germany using icon: A comprehensive evaluation. *Quarterly Journal of the Royal Meteorological Society*, **143 (702)**, 69–100.

Hess, P. and H. Brezowsky, 1969: Katalog der grosswetterlagen europas.

Hogan, R. J. and A. Bozzo, 2016: *ECRAD: A new radiation scheme for the IFS*. European Centre for Medium-Range Weather Forecasts.

Hogan, R. J. and A. J. Illingworth, 2000: Deriving cloud overlap statistics from radar. *Quarterly Journal of the Royal Meteorological Society*, **126 (569)**, 2903–2909, doi:https://doi.org/10.1002/qj.49712656914.

Hogan, R. J., C. Jakob, and A. J. Illingworth, 2001: Comparison of ecmwf winter-season cloud fraction with radar-derived values. *Journal of Applied Meteorology*, **40 (3)**, 513–525.

Honda, T., T. Miyoshi, G.-Y. Lien, S. Nishizawa, R. Yoshida, S. A. Adachi, K. Terasaki, K. Okamoto, H. Tomita, and K. Bessho, 2018: Assimilating all-sky himawari-8 satellite infrared radiances: A case of typhoon soudelor (2015). *Monthly Weather Review*, **146 (1)**, 213–229.

Houtekamer, P. L., H. L. Mitchell, G. Pellerin, M. Buehner, M. Charron, L. Spacek, and B. Hansen, 2005: Atmospheric data assimilation with an ensemble kalman filter: Results with real observations. *Monthly weather review*, **133 (3)**, 604–620.

Hu, Y. and K. Stamnes, 1993: An accurate parameterization of the radiative properties of water clouds suitable for use in climate models. *Journal of climate*, **6 (4)**, 728–742.

Hunt, B. R., E. J. Kostelich, and I. Szunyogh, 2007: Efficient data assimilation for spatiotemporal chaos: A local ensemble transform kalman filter. *Physica D: Nonlinear Phenomena*, **230 (1-2)**, 112–126.

IEA, 2020: Solar pv, iea, paris. URL `https://www.iea.org/reports/solar-pv`.

Illingworth, A., R. Hogan, E. O'connor, D. Bouniol, M. Brooks, J. Delanoë, D. Donovan, J. Eastment, N. Gaussiat, J. Goddard, et al., 2007: Cloudnet: Continuous evaluation of cloud profiles in seven operational models using ground-based observations. *Bulletin of the American Meteorological Society*, **88 (6)**, 883–898.

Ingel, L. K., 2014: On some generalization of the rayleigh problem on a convective instability. *Univers. J. Appl. Math*, **2 (1)**, 24–28.

Jakub, F. and B. Mayer, 2015: A three-dimensional parallel radiative transfer model for atmospheric heating rates for use in cloud resolving models—the tenstream solver. *Journal of Quantitative Spectroscopy and Radiative Transfer*, **163**, 63–71, doi:https://doi.org/10.1016/j.jqsrt.2015.05.003, URL `https://www.sciencedirect.com/science/article/pii/S0022407315001727`.

Janjić, T., N. Bormann, M. Bocquet, J. Carton, S. Cohn, S. Dance, S. Losa, N. Nichols, R. Potthast, J. Waller, et al., 2018: On the representation error in data assimilation. *Quarterly Journal of the Royal Meteorological Society*, **144 (713)**, 1257–1278.

Keil, C., F. Baur, K. Bachmann, S. Rasp, L. Schneider, and C. Barthlott, 2019: Relative contribution of soil moisture, boundary-layer and microphysical perturbations on convective predictability in different weather regimes. *Quarterly Journal of the Royal Meteorological Society*, **145 (724)**, 3102–3115.

Keller, M., O. Fuhrer, J. Schmidli, M. Stengel, R. Stöckli, and C. Schär, 2016: Evaluation of convection-resolving models using satellite data: The diurnal cycle of summer convection over the alps. *Meteorologische Zeitschrift*, **25 (2)**, 165–179.

King, M. D., S. Platnick, W. P. Menzel, S. A. Ackerman, and P. A. Hubanks, 2013: Spatial and temporal distribution of clouds observed by modis onboard the terra and aqua satellites. *IEEE transactions on geoscience and remote sensing*, **51 (7)**, 3826–3852.

Kniffka, A., M. Stengel, M. Lockhoff, R. Bennartz, and R. Hollmann, 2014: Characteristics of cloud liquid water path from seviri onboard the meteosat second generation 2 satellite for several cloud types. *Atmospheric Measurement Techniques*, **7 (4)**, 887–905.

Köhler, C., A. Steiner, Y.-M. Saint-Drenan, D. Ernst, A. Bergmann-Dick, M. Zirkelbach, Z. B. Bouallègue, I. Metzinger, and B. Ritter, 2017: Critical weather situations for renewable energies–part b: Low stratus risk for solar power. *Renewable energy*, **101**, 794–803.

Köpke, P. and M. Sachweh, 2012: Satellitenmeteorologie. *Uni-Taschenbücher, UTB GmbH*.

Koppe, P. and A. Stozek, 1999: *Kommunales Abwasser: seine Inhaltsstoffe nach Herkunft, Zusammensetzung und Reaktionen im Reinigungsprozeß einschließlich Klärschlämme*. Vulkan-Verlag GmbH.

Kostka, P. M., M. Weissmann, R. Buras, B. Mayer, and O. Stiller, 2014: Observation operator for visible and near-infrared satellite reflectances. *Journal of Atmospheric and Oceanic Technology*, **31 (6)**, 1216–1233.

Kurzrock, F., S. Cros, F. Chane-Ming, J. Otkin, A. Hutt, L. Linguet, G. Lajoie, and R. Potthast, 2018: A review of the use of geostationary satellite observations in regional-scale models for short-term cloud forecasting. *Meteorologische Zeitschrift*, **27 (4)**, 277–298.

Lange, H. and G. C. Craig, 2014: The impact of data assimilation length scales on analysis and prediction of convective storms. *Monthly Weather Review*, **142 (10)**, 3781–3808.

Lenzi, V., A. Ulbig, and G. Andersson, 2013: Impacts of forecast accuracy on grid integration of renewable energy sources. *2013 IEEE Grenoble Conference*, 1–6, doi: 10.1109/PTC.2013.6652486.

Lin, Y.-L., R. D. Farley, and H. D. Orville, 1983: Bulk parameterization of the snow field in a cloud model. *Journal of climate and applied meteorology*, **22 (6)**, 1065–1092.

Lorenc, A. and O. Hammon, 1988: Objective quality control of observations using bayesian methods. theory, and a practical implementation. *Quarterly Journal of the Royal Meteorological Society*, **114 (480)**, 515–543.

Lorenz, E., J. Hurka, D. Heinemann, and H. G. Beyer, 2009: Irradiance forecasting for the power prediction of grid-connected photovoltaic systems. *IEEE Journal of selected topics in applied earth observations and remote sensing*, **2 (1)**, 2–10.

Marseille, G.-J. and A. Stoffelen, 2017: Toward scatterometer winds assimilation in the mesoscale harmonie model. *IEEE Journal of Selected Topics in Applied Earth Observations and Remote Sensing*, **10 (5)**, 2383–2393.

Martin, G., D. Johnson, and A. Spice, 1994: The measurement and parameterization of effective radius of droplets in warm stratocumulus clouds. *Journal of Atmospheric Sciences*, **51 (13)**, 1823–1842.

Martin, W. J. and M. Xue, 2006: Sensitivity analysis of convection of the 24 may 2002 ihop case using very large ensembles. *Monthly Weather Review*, **134 (1)**, 192 – 207, doi:10.1175/MWR3061.1, URL `https://journals.ametsoc.org/view/journals/mwre/134/1/mwr3061.1.xml`.

Mathiesen, P., C. Collier, and J. Kleissl, 2013: A high-resolution, cloud-assimilating numerical weather prediction model for solar irradiance forecasting. *Solar Energy*, **92**, 47–61.

Mayer, B., 2009: Radiative transfer in the cloudy atmosphere. *EPJ Web of Conferences*, EDP Sciences, Vol. 1, 75–99.

Mayer, B., 2018: Erwärmungs- und Abkühlungsraten - Wie wichtig ist 3D-Strahlungstransport. *promet*, **100**, 98–110.

Mayer, B. and A. Kylling, 2005: The libradtran software package for radiative transfer calculations-description and examples of use. *Atmospheric Chemistry and Physics*, **5 (7)**, 1855–1877.

McNally, A., 2002: A note on the occurrence of cloud in meteorologically sensitive areas and the implications for advanced infrared sounders. *Quarterly Journal of the Royal Meteorological Society: A journal of the atmospheric sciences, applied meteorology and physical oceanography*, **128 (585)**, 2551–2556.

Meilinger, S., 2017: Metpvnet. Präsident der Hochschule Bonn-Rhein-Sieg, Prof. Dr. Hartmut Ihne, `http://metpvnet.de`, last accessed on 16/08/21.

Meirink, J., R. Roebeling, and P. Stammes, 2013: Inter-calibration of polar imager solar channels using seviri. *Atmospheric Measurement Techniques Discussions*, **6 (2)**.

Mlawer, E. and S. Clough, 1997: On the extension of rapid radiative transfer model to the shortwave region. *Proceedings of the 6th Atmospheric Radiation Measurement (ARM) Science Team Meeting, US Department of Energy, CONF-9603149*, Citeseer.

Mlawer, E. J., S. J. Taubman, P. D. Brown, M. J. Iacono, and S. A. Clough, 1997: Radiative transfer for inhomogeneous atmospheres: Rrtm, a validated correlated-k model for the longwave. *Journal of Geophysical Research: Atmospheres*, **102 (D14)**, 16 663–16 682.

Necker, T., S. Geiss, M. Weissmann, J. Ruiz, T. Miyoshi, and G.-Y. Lien, 2020: A convective-scale 1,000-member ensemble simulation and potential applications. *Quarterly Journal of the Royal Meteorological Society*, **146 (728)**, 1423–1442.

Necker, T., M. Weissmann, and M. Sommer, 2018: The importance of appropriate verification metrics for the assessment of observation impact in a convection-permitting modelling system. *Quarterly Journal of the Royal Meteorological Society*, **144 (714)**, 1667–1680.

Neher, I., T. Buchmann, S. Crewell, B. Pospichal, and S. Meilinger, 2019: Impact of atmospheric aerosols on solar power. *Meteorologische Zeitschrift*, **28 (4)**, 305–321, doi: 10.1127/metz/2019/0969, URL `http://dx.doi.org/10.1127/metz/2019/0969`.

Otkin, J. A. and T. J. Greenwald, 2008: Comparison of wrf model-simulated and modis-derived cloud data. *Monthly Weather Review*, **136 (6)**, 1957–1970.

Otkin, J. A., W. E. Lewis, A. J. Lenzen, B. D. McNoldy, and S. J. Majumdar, 2017: Assessing the accuracy of the cloud and water vapor fields in the hurricane wrf (hwrf) model using satellite infrared brightness temperatures. *Monthly Weather Review*, **145 (5)**, 2027–2046.

Pagé, C., L. Fillion, and P. Zwack, 2007: Diagnosing summertime mesoscale vertical motion: Implications for atmospheric data assimilation. *Monthly weather review*, **135 (6)**, 2076–2094.

Palmén, E. H. and C. W. Newton, 1969: *Atmospheric circulation systems: their structure and physical interpretation*, Vol. 13. Academic press.

Pfeifer, M., W. Yen, M. Baldauf, G. Craig, S. Crewell, J. Fischer, M. Hagen, A. Hühnerbein, M. Mech, T. Reinhardt, M. Schröder, and A. Seifert, 2010: Validating precipitation forecasts using remote sensor synergy: A case study approach. *Meteorologische Zeitschrift*, **19 (6)**, 601–617, doi:10.1127/0941-2948/2010/0487.

Piper, D., M. Kunz, F. Ehmele, S. Mohr, B. Mühr, A. Kron, and J. Daniell, 2016: Exceptional sequence of severe thunderstorms and related flash floods in may and june 2016 in germany–part 1: Meteorological background. *Natural Hazards and Earth System Sciences*, **16 (12)**, 2835–2850.

Politovich, M. K. and W. A. Cooper, 1988: Variability of the supersaturation in cumulus clouds. *Journal of the atmospheric sciences*, **45 (11)**, 1651–1664.

Reinhardt, T. and A. Seifert, 2006: A three-category ice scheme for lmk, cosmo newsletter, no. 6, deutscher wetterdienst, offenbach, germany, 115–120.

Remund, J., R. Perez, and E. Lorenz, 2008: Comparison of solar radiation forecasts for the usa. *Proc. of the 23rd European PV Conference*, Vol. 14.

Roberts, N. M. and H. W. Lean, 2008: Scale-selective verification of rainfall accumulations from high-resolution forecasts of convective events. *Monthly Weather Review*, **136 (1)**, 78–97.

Rossow, W. B. and R. A. Schiffer, 1991: Isccp cloud data products. *Bulletin of the American Meteorological Society*.

Saunders, R., J. Hocking, D. Rundle, P. Rayer, S. Havemann, M. Matricardi, A. Geer, C. Lupu, P. Brunel, and J. Vidot, 2017: Rttov v12 science and validation report, 78 pp.

Saunders, R., J. Hocking, E. Turner, P. Rayer, D. Rundle, P. Brunel, J. Vidot, P. Roquet, M. Matricardi, A. Geer, et al., 2018: An update on the rttov fast radiative transfer model (currently at version 12). *Geoscientific Model Development*, **11 (7)**, 2717–2737.

Schäfer, S., M. Köhler, R. Hogan, C. Klinger, D. Rieger, G. Zängl, M. Ahlgrimm, and A. de Lozar, 2021: Addressing radiation and cloud uncertainties with the new radiation scheme ecrad in icon. *EGU General Assembly Conference Abstracts*, EGU21–10 076, `http://www.meteo.fr/cic/meetings/2021/high-tune/presentations/14_02.pdf`, last accessed on 23/08/21.

Scheck, L., 2021: A neural network based forward operator for visible satellite images and its adjoint. *Journal of Quantitative Spectroscopy and Radiative Transfer*, 107841, doi: https://doi.org/10.1016/j.jqsrt.2021.107841, URL `https://www.sciencedirect.com/science/article/pii/S0022407321003344`.

Scheck, L., P. Frèrebeau, R. Buras-Schnell, and B. Mayer, 2016: A fast radiative transfer method for the simulation of visible satellite imagery. *Journal of Quantitative Spectroscopy and Radiative Transfer*, **175**, 54–67.

Scheck, L., M. Weissmann, and L. Bach, 2020: Assimilating visible satellite images for convective-scale numerical weather prediction: A case study. *Quarterly Journal of the Royal Meteorological Society*.

Scheck, L., M. Weissmann, and B. Mayer, 2018: Efficient methods to account for cloud-top inclination and cloud overlap in synthetic visible satellite images. *Journal of Atmospheric and Oceanic Technology*, **35 (3)**, 665–685.

Schmetz, J., P. Pili, S. Tjemkes, D. Just, J. Kerkmann, S. Rota, and A. Ratier, 2002: An introduction to meteosat second generation (msg). *Bulletin of the American Meteorological Society*, **83 (7)**, 977–992.

Schraff, C., H. Reich, A. Rhodin, A. Schomburg, K. Stephan, A. Periáñez, and R. Potthast, 2016: Kilometre-scale ensemble data assimilation for the cosmo model (kenda). *Quarterly Journal of the Royal Meteorological Society*, **142 (696)**, 1453–1472.

Schröttle, J., M. Weissmann, L. Scheck, and A. Hutt, 2020: Assimilating visible and infrared radiances in idealized simulations of deep convection. *Monthly Weather Review*, **148 (11)**, 4357–4375.

Schrödter-Homscheidt, M., H. Deifel, and D. Heinemann, 2015: Grundlagen des Energiesystems für Energiemeteorologen. *promet*, **39**, 142.

Segal, Y. and A. Khain, 2006: Dependence of droplet concentration on aerosol conditions in different cloud types: Application to droplet concentration parameterization of aerosol conditions. *Journal of Geophysical Research: Atmospheres*, **111 (D15)**.

Seifert, 2011: Uncertainty and complexity in cloud microphysics. Workshop on representing model uncertainty and error in numerical weather and climate prediction models, ECMWF, June 2011, `https://www.ecmwf.int/sites/default/files/elibrary/2011/14857-uncertainty-and-complexity-cloud-microphysics.pdf`, last accessed on 23/08/21.

Seifert, A. and K. D. Beheng, 2006: A two-moment cloud microphysics parameterization for mixed-phase clouds. part 1: Model description. *Meteorology and atmospheric physics*, **92 (1-2)**, 45–66.

Senf, F. and H. Deneke, 2017: Uncertainties in synthetic meteosat seviri infrared brightness temperatures in the presence of cirrus clouds and implications for evaluation of cloud microphysics. *Atmospheric Research*, **183**, 113 – 129, doi:https://doi.org/10.1016/j.atmosres.2016.08.012.

Senf, F., A. Voigt, N. Clerbaux, A. Hünerbein, and H. Deneke, 2020: Increasing resolution and resolving convection improve the simulation of cloud-radiative effects over the north atlantic. *Journal of Geophysical Research: Atmospheres*, **125 (19)**, e2020JD032 667.

Siefert, M., R. Hagedorn, A. Braun, J. Dobschinski, R. Fritz, and G. Good, 2017: *Abschlussbericht EWELINE: Erstellung innovativer Wetter-und Leistungsprognosemodelle für die Netzintegration wetterabhängiger Energieträger*. Fraunhofer-Institut für Windenergie und Energiesystemtechnik, IWES.

Sieling, S. and M. Müllers, 2021: Redispatch 2.0 – Verteilnetzbetreiber in Zugzwang. EEB ENERKO Energiewirtschaftliche Beratung GmbH, Aldenhoven, Germany, URL `https://enerko.de/wp-content/uploads/2020/09/200917_Whitepaper_Redispatch_2.0.pdf`.

Simmer, C., G. Adrian, S. Jones, V. Wirth, M. Göber, C. Hohenegger, T. Janjic, J. Keller, C. Ohlwein, A. Seifert, et al., 2016: Herz: The german hans-ertel centre for weather research. *Bulletin of the American Meteorological Society*, **97 (6)**, 1057–1068.

Sissenwine, N., M. Dubin, and H. Wexler, 1962: The us standard atmosphere, 1962. *Journal of Geophysical Research*, **67 (9)**, 3627–3630.

Solomon, S., D. Qin, M. Manning, Z. Chen, M. Marquis, K. Averyt, M. Tignor, and H. Miller, 2007: Ipcc fourth assessment report (ar4). *Climate change*.

Sommeria, G. and J. Deardorff, 1977: Subgrid-scale condensation in models of nonprecipitating clouds. *Journal of Atmospheric Sciences*, **34 (2)**, 344–355.

Stamnes, K., S.-C. Tsay, W. Wiscombe, and K. Jayaweera, 1988: Numerically stable algorithm for discrete-ordinate-method radiative transfer in multiple scattering and emitting layered media. *Applied optics*, **27 (12)**, 2502–2509.

Statista, 2021: Anzahl der Stromnetzbetreiber in Deutschland in den Jahren 2010 bis 2020. Statista GmbH, Hamburg, Germany, URL `https://de.statista.com/statistik/daten/studie/152937/umfrage/anzahl-der-stromnetzbetreiber-in-deutschland-seit-2006/`.

Stevens, B., 2005: Atmospheric moist convection. *Annu. Rev. Earth Planet. Sci.*, **33**, 605–643.

Talagrand, O., 1997: Assimilation of observations, an introduction (gtspecial issueltdata assimilation in meteology and oceanography: Theory and practice). *Journal of the Meteorological Society of Japan. Ser. II*, **75 (1B)**, 191–209.

Tegen, I., P. Hollrig, M. Chin, I. Fung, D. Jacob, and J. Penner, 1997: Contribution of different aerosol species to the global aerosol extinction optical thickness: Estimates from model results. *Journal of Geophysical Research: Atmospheres*, **102 (D20)**, 23 895–23 915.

Tiedtke, M., 1993: Representation of clouds in large-scale models. *Monthly Weather Review*, **121 (11)**, 3040–3061.

Tselioudis, G. and C. Jakob, 2002: Evaluation of midlatitude cloud properties in a weather and a climate model: Dependence on dynamic regime and spatial resolution. *Journal of Geophysical Research: Atmospheres*, **107 (D24)**, AAC 14–1–AAC 14–10, doi:https://doi.org/10.1029/2002JD002259.

Tuohy, A., J. Zack, S. E. Haupt, J. Sharp, M. Ahlstrom, S. Dise, E. Grimit, C. Mohrlen, M. Lange, M. G. Casado, et al., 2015: Solar forecasting: Methods, challenges, and performance. *IEEE Power and Energy Magazine*, **13 (6)**, 50–59.

Vidot, J., P. Brunel, M. Dumont, C. Carmagnola, and J. Hocking, 2018: The vis/nir land and snow brdf atlas for rttov: Comparison between modis mcd43c1 c5 and c6. *Remote Sensing*, **10 (1)**, 21.

Wallace, J. M. and P. V. Hobbs, 2006: *Atmospheric science: an introductory survey*, Vol. 92. Elsevier.

Wapler, K. and B. Mayer, 2008: A fast three-dimensional approximation for the calculation of surface irradiance in large-eddy simulation models. *Journal of Applied Meteorology and Climatology*, **47 (12)**, 3061–3071.

Webb, M., C. Senior, S. Bony, and J.-J. Morcrette, 2001: Combining erbe and isccp data to assess clouds in the hadley centre, ecmwf and lmd atmospheric climate models. *Climate Dynamics*, **17 (12)**, 905–922.

Weisman, M. L., W. C. Skamarock, and J. B. Klemp, 1997: The resolution dependence of explicitly modeled convective systems. *Monthly Weather Review*, **125 (4)**, 527–548.

Weissmann, M., M. Gober, C. Hohenegger, T. Janjic, J. Keller, C. Ohlwein, A. Seifert, S. Tromel, T. Ulbrich, K. Wapler, et al., 2014: Initial phase of the hans-ertel centre for weather research-a virtual centre at the interface of basic and applied weather and climate research. *Meteorologische Zeitschrift*, **23**, 193–208.

Wirth, H. and K. Schneider, 2015: Aktuelle fakten zur photovoltaik in deutschland. *Fraunhofer ISE*, **201 (2)**.

Wolters, E. L., R. A. Roebeling, and A. J. Feijt, 2008: Evaluation of cloud-phase retrieval methods for seviri on meteosat-8 using ground-based lidar and cloud radar data. *Journal of applied meteorology and climatology*, **47 (6)**, 1723–1738.

Wood, R. and P. R. Field, 2011: The distribution of cloud horizontal sizes. *Journal of Climate*, **24 (18)**, 4800–4816.

Wyser, K., 1998: The effective radius in ice clouds. *Journal of Climate*, **11 (7)**, 1793–1802.

Yang, P., H. Wei, H.-L. Huang, B. A. Baum, Y. X. Hu, G. W. Kattawar, M. I. Mishchenko, and Q. Fu, 2005: Scattering and absorption property database for nonspherical ice particles in the near- through far-infrared spectral region. *Appl. Opt.*, **44 (26)**, 5512–5523, doi:10.1364/AO.44.005512.

Yuter, S. E. and R. A. Houze Jr, 1995: Three-dimensional kinematic and microphysical evolution of florida cumulonimbus. part ii: Frequency distributions of vertical velocity, reflectivity, and differential reflectivity. *Monthly weather review*, **123 (7)**, 1941–1963.

Zack, J., 2011: Current status and challenges of solar power production forecasting. ETWG Solar Workshop, Austin, Texas, `http://www.ercot.com/gridinfo/ettsArchive/solar/04_-_AWS_John_Zack_ERCOT_workshop_25apr11.pdf`, last accessed on 12/07/19.

Zängl, G., D. Reinert, P. Rípodas, and M. Baldauf, 2015: The icon (icosahedral non-hydrostatic) modelling framework of dwd and mpi-m: Description of the non-hydrostatic dynamical core. *Quarterly Journal of the Royal Meteorological Society*, **141 (687)**, 563–579.

Zeng, Y., T. Janjić, A. de Lozar, U. Blahak, H. Reich, C. Keil, and A. Seifert, 2018: Representation of model error in convective-scale data assimilation: Additive noise, relaxation methods, and combinations. *Journal of Advances in Modeling Earth Systems*, **10 (11)**, 2889–2911.

Zhang, F., M. Minamide, and E. E. Clothiaux, 2016: Potential impacts of assimilating all-sky infrared satellite radiances from goes-r on convection-permitting analysis and prediction of tropical cyclones. *Geophysical research letters*, **43 (6)**, 2954–2963.

Zhang, F., C. Snyder, and J. Sun, 2004: Impacts of initial estimate and observation availability on convective-scale data assimilation with an ensemble kalman filter. *Monthly Weather Review*, **132 (5)**, 1238–1253.

Zhang, M., W. Lin, S. Klein, J. Bacmeister, S. Bony, R. Cederwall, A. Del Genio, J. Hack, N. Loeb, U. Lohmann, et al., 2005: Comparing clouds and their seasonal variations in 10 atmospheric general circulation models with satellite measurements. *Journal of Geophysical Research: Atmospheres*, **110 (D15)**.

Zhang, Y., D. J. Stensrud, and F. Zhang, 2019: Simultaneous assimilation of radar and all-sky satellite infrared radiance observations for convection-allowing ensemble analysis and prediction of severe thunderstorms. *Monthly Weather Review*, **147 (12)**, 4389–4409.

Zhang, Y., F. Zhang, and D. J. Stensrud, 2018: Assimilating all-sky infrared radiances from goes-16 abi using an ensemble kalman filter for convection-allowing severe thunderstorms prediction. *Monthly Weather Review*, **146 (10)**, 3363–3381.

Danksagung

Allen voran möchte ich natürlich meinem Doktorvater Martin Weissmann danken. Lieber Martin, vielen Dank für die aufregende und spannende Zeit, die du mir ermöglicht hast und in der ich vieles von Dir lernen konnte! Auch wenn wir uns räumlich, durch Deine Berufung nach Wien, distanziert haben, warst Du doch immer da um mit Rat und Tat zur Seite zu stehen. Wer weiß, was die Paralleluniversen noch so bereit halten.

In München war ich dennoch weiterhin gut betreut und aufgehoben und das habe ich vor allem Leonhard Scheck zu verdanken. Lieber Leonhard, ohne Dich wäre diese Arbeit in dieser Form unmöglich gewesen. Auch wenn ich Dir vielleicht manchmal Deine Programme ein bisserl durcheinander gebracht habe, hat es immer Spaß gemacht mit Dir zu arbeiten und konnte sehr viel von Dir lernen. Danke für Deine großartige Unterstützung, Deine Ideen und Deinen endlosen Optimismus!

An dieser Stelle möchte ich auch meinem Zweitgutachter Bernhard Mayer danken, der mich in meiner ersten Meteorologie-Vorlesung für die Atmosphärenphysik begeistern konnte und mich die letzten 10 Jahre an der LMU begleitet hat. Lieber Herr Mayer, vielen Dank für die wertvollen Grundlagen und Denkweisen, die ich von Ihnen lernen durfte!

Mein besonderer Dank gilt meinen Kolleg*innen vom Deutschen Wetterdienst, im besonderen Alberto de Lozar und Lilo Bach. Lieber Alberto und liebe Lilo, danke für die endlosen Simulationen, Ratschläge, Diskussionen und einfach die tolle Zeit mit euch. An dieser Stelle möchte ich auch dem Satelliten Datenassimilations-Team vom DWD danken: Roland P., Christina C.-W., Annika S., Thomas D., Christina S. & Christoph S. Und, kaum zu glauben, nach den Jahren ist mir Offenbach durch euch doch an's Herz gewachsen. Schade, dass wir uns die letzten anderthalb Jahre nicht mehr treffen konnten. Dafür sind wir jetzt DFN-Profis.

Ein weiterer großer Dank gilt meinen Kolleg*innen vom Projekt MetPVNet, die mir unzählige Ideen beschert und die Herausforderungen der solaren Energieerzeugung näher gebracht haben. Einen möchte ich dabei ganz besonders danken, dem Felix Gödde. Lieber Felix, nicht nur für die letzten drei, sondern für die letzten 10 Jahre will ich Dir danken, auch für die schöne und lehrreiche Zeit als „echte“ vor-Corona Studenten. An dieser Stelle möchte ich allen meinen Weggefährt*innen im Bachelor und Master für die unvergessliche Zeit danken.

Ein großer Dank gilt auch meinen (Ex-) Kolleg*innen und Korrekturleser*innen, welche einen wichtigen Beitrag zu dieser Arbeit geleistet haben: Anne M., Matthias S., Theresa D. und Stefano S. Ganz besonders möchte ich noch Tobias Necker danken. Lieber Tobi, mit Dir macht es immer Spaß über die Arbeit (auch wenn wir thematisch immer etwas asynchron unterwegs waren) und das Leben zu grübeln. Ohne euch, hätte ich es wahrscheinlich nicht so weit geschafft.

Nicht zu vergessen ist die gute Seele unseres Instituts, Barbara Baumann. Liebe Barbara, mit Dir ist es immer eine Freude Zeit zu verbringen! Egal ob auf dem Balkon, bei einem Zigarettchen oder zuletzt der gemeinsame Genuss in der Mensa. Du hast immer eine Lösung parat und ohne Dich wäre das alles nicht so unbeschwert verlaufen.

Zu guter Letzt, aber wohl doch am wichtigsten: meine Freunde und meinem kleinen Bruder Josef ein ganz herzliches Dankeschön. Nur mit euch wird das Leben bunt und zu einem Erlebnis! Und ∞-Dank meiner größten Stütze und dem besten Menschen: René Hanschke! Für's hoch helfen, wenn's mal wieder gar nicht ging, die unentwegte Motivation und Deine endlose Neugierde.

MetPVNet This doctoral thesis was carried out in the integrated project MetPVNet (Meilinger, 2017), project number 0350009A, funded by the Federal Ministry for Economic Affairs and Energy.

HErZ I would like to thank the Hans Ertel Centre for Weather Research (Weissmann et al., 2014, Simmer et al., 2016) for supporting this work. This German research network of universities, research institutes and the German Weather Service is funded by the BMVI (Federal Ministry of Transport and Digital Infrastructure).